Wireless Performance Analysis of Buildings for Indoor Communications

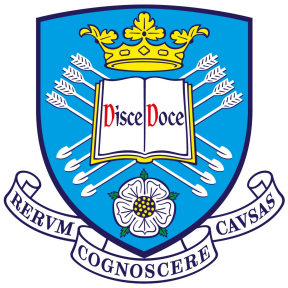

Wenfei Yang

Supervisors: Prof. Jie Zhang, Dr Wei Liu

Department of Electronic and Electrical Engineering
The University of Sheffield

This thesis is submitted for the degree of
Doctor of Philosophy

January 2022

I would like to dedicate this thesis to my beloved mom and dad.

Acknowledgements

First and foremost, I would like to express the deepest appreciation to my supervisor, Professor Jie Zhang, for always being supportive in all aspects during my PhD. His invaluable insight into this exciting research direction, the building wireless performance, laid the foundations of the works in my thesis. His unique perspective, innovative spirit, and optimism have left a deep impression on me.

Completing my thesis would not have been possible without the support and nurturing of Dr Jiliang Zhang. As an enthusiastic, self-motivated, and talented researcher, he is my role model.

I would like to thank Dr Andrés Alayón Glazunov for his invaluable advice, patience, and meticulous attention to detail.

I very much appreciate Professor Sana Salous for kindly offering me the opportunities to participate in practical channel measurements and many insightful suggestions.

I would also like to extend my gratitude to Dr Jie Huang, Dr Yuan Gao, and Dr Hui Song for collaborations in papers.

Special thanks to my friends and colleagues, Yixin Z., Yixin H., Mengxue, Mengxin, Songjiang, Zhengyu, Junwei, and Bo, for their company, encouragement, and help.

Last but not least, I would like to express my heartfelt appreciation to my dear family. For years I could not do anything for them, but they always stand by my side.

Abstract

The ever-boosting indoor traffic demands make indoor wireless communications a necessity in buildings. The performance of an indoor wireless network is constrained by the building where it is deployed, as the building structures affect network deployments and signal propagation. This thesis investigates the effects of building structures on indoor wireless communications for both buildings in use and buildings under design.

Firstly, a three-dimensional (3-D) indoor line-of-sight (LOS) probability model is proposed in this thesis. The LOS probability is a critical indicator of the blockage effects in a given building. The proposed model with a closed-form expression can be used to compute the LOS probability accurately based on actual building layouts in 3-D space. It can be employed for indoor network performance evaluation and optimisation.

Secondly, this thesis focuses on the building wireless performance (BWP), quantifying the impact of building structures on indoor wireless networks at the design stage of a building. Two figures of merit (FoMs), i.e., the power gain (PG) and the interference gain (IG), have been proposed to assess the BWP. Employing open space as the benchmark, the PG and the IG respectively quantify the effective change of the intended signal power and the undesired power, i.e., interference signal and thermal noise power, received in a probing location due to the presence of a building. In previous works, the analytical models of the PG and the IG were derived for single rooms on a two-dimensional (2-D) plane, which means only the impact of the geometry of a single room was considered. However, there are other factors of building structures affecting indoor network performance, e.g., building materials and layouts. This thesis extends the BWP concept by considering more practical factors in FoM calculation. For single storeys on 2-D planes, a partition-based BWP evaluation scheme is proposed to introduce the effects of both building materials and layouts. For multi-storey buildings in 3-D space, a multi-storey BWP evaluation scheme is proposed to address the impact of the number of storeys and their height. Both BWP evaluation schemes proposed in this thesis consist of preprocessing of building plans and closed-form analytical models of the BWP FoMs. The works in this thesis are critical complements to the initial BWP framework and can be employed in future wireless-friendly building design.

List of Publications

Published Papers

[1] **W. Yang**, J. Zhang, A. A. Glazunov, and J. Zhang, "Line-of-sight probability for channel modeling in 3-D indoor environments," *IEEE Antennas Wireless Propag. Lett.*, vol. 19, no. 7, pp. 1182–1186, July 2020. (Chapter 3)

[2] **W. Yang**, J. Zhang, H. Song, and J. Zhang, "Partition-based analytic evaluation of building wireless performance," *IEEE Trans. Veh. Technol.*, vol. 70, no. 9, pp. 9036–9049, Sep. 2021. (Chapter 4)

[3] **W. Yang**, J. Huang, J. Zhang, Y. Gao, S. Salous, and J. Zhang, "Measurements of reflection and penetration loss in indoor environments in the 39-GHz band," in *15th Eur. Conf. Antennas and Propag. (EuCAP)*, Düsseldorf, Germany, 2021, pp. 1–5. (Section 2.1.1)

[4] J. Zhang, A. A. Glazunov, **W. Yang**, and J. Zhang, "Fundamental wireless performance of a building," *IEEE Wireless Commun.*, doi: 10.1109/MWC.121.2100244.

[5] **W. Yang**, J. Huang, J. Zhang, Y. Gao, S. Salous, and J. Zhang, "On verification of intelligent ray launching algorithm in indoor environments at Ka-band," in *Radio Sci.*, vol. 56, no. 9, pp. 1–11, Sep. 2021.

[6] **W. Yang**, J. Zhang, and J. Zhang, "On performance of ultra-dense neighborhood small cell networks in urban scenarios," *IEEE Commun. Lett.*, vol. 25, no. 4, pp. 1378–1382, Apr. 2021.

[7] **W. Yang**, J. Huang, J. Zhang, S. Salous, and J. Zhang, "Indoor measurement based verification of ray launching algorithm at the Ka-band," in *XXXIII URSI General Assem. and Scientific Symp. (URSI GASS)*, Roma, Italy, 2020, pp. 1–4.

[8] **W. Yang**, J. Zhang, and J. Zhang, "On evaluation of indoor to outdoor communications using neighbourhood small cells," *IEEE Trans. Veh. Technol.*, vol. 69, no. 7, pp. 8045–8050, July 2020.

[9] **W. Yang**, J. Zhang, and J. Zhang, "Machine learning based indoor line-of-sight probability prediction," in *Int. Symp. Antennas and Propag. (ISAP)*, Xi'an, China, 2019, pp. 1–3.

Table of contents

List of figures

Nomenclature

Acronyms / Abbreviations

1-D	One-Dimensional
2-D	Two-Dimensional
2G	Second Generation
3-D	Three-Dimensional
3G	Third Generation
3GPP	Third Generation Partnership Project
4G	Fourth Generation
5G	Fifth Generation
6G	Sixth Generation
ABG	Alpha-Beta-Gamma
ASE	Area Spectral Efficiency
BS	Base Station
BWP	Building Wireless Performance
CAGR	Compound Annual Growth Rate
CDF	Cumulative Distribution Function
CI	Close-in
CoMP	Coordinated Multipoint

DPP Determinantal Point Process

EM Electromagnetic

ER Effective Roughness

FI Floating Intercept

FoM Figure of Merit

FSPL Free Space Path Loss

GO Geometrical Optic

HetNet Heterogeneous Network

IG Interference Gain

IoT Internet of Things

ITU International Telecommunication Union

KED Knife Edge Diffraction

LOS Line-of-Sight

MHCP Matérn Hard-Core Point Process

MIMO Multiple-Input and Multiple-Output

mmWave Millimetre Wave

MPLP Manhattan Poisson Line Process

MRT Maximum Ratio Transmissions

NLOS Non-Line-of-Sight

PCP Poisson Cluster Process

PDF Probability Density Function

PG Power Gain

PHCP Poisson Hard-Core Process

PHP Poisson Hole Process

PLE Path Loss Exponent

PPP Poisson Point Process

RL Ray Launching

RMSE Root-Mean-Square Error

RT Ray Tracing

SBS Small Base Station

SINR Signal-to-Interference-plus-Noise Ratio

SIR Signal-to-Interference Ratio

SNR Signal-to-Noise Ratio

TM Toy Model

Tx-Rx Transmitter-Receiver

UDS Ultra Dense Small Cell

UE User Equipment

UTD Uniform Theory of Diffraction

WINNER Wireless World Initiative New Radio

XR Extended Reality

Chapter 1

Introduction

Overview

Comparing with 5G, 6G is expected to achieve 10 times higher data rate and 10-100 times higher energy efficiency. As over 80% of data traffic takes place indoors, high-capacity and energy-efficient wireless networks are required in buildings. It has been aware that the impact of complex building structures on indoor wireless network performance should be considered not only in indoor network design but as early as at the design stage of a building. This chapter first introduces the background and motivations of this thesis. Then, the research contributions and the organisation of this thesis are presented.

1.1 Background

With the remarkable upsurge of emerging technologies, researchers have started to picture our future life with a wide variety of smart services. The current plane multimedia is expected to be developed to high fidelity extended reality (XR) and then to wireless holographic communication by 2030 [1]. Based on this trend, various revolutionary techniques, such as remote surgery, immersive gaming, and autonomous vehicles, are expected to be applied in our daily life. To match the requirements of future applications, visions of wireless networks for the year 2030 and beyond, i.e., the 6G era, have been widely discussed. Fig. 1.1 gives a comparison of key capabilities among 4G, 5G, and 6G according to the state-of-the-art discussions, where the innermost polygon represents the reference values for 4G extracted from Report ITU-R M.2134 [2], the polygon in the middle represents the reference values for 5G extracted from Report ITU-R M.2083 [3], and the outermost polygon represents the reference values for 6G mentioned in [4–6]. Comparing with 5G, 6G is projected to have

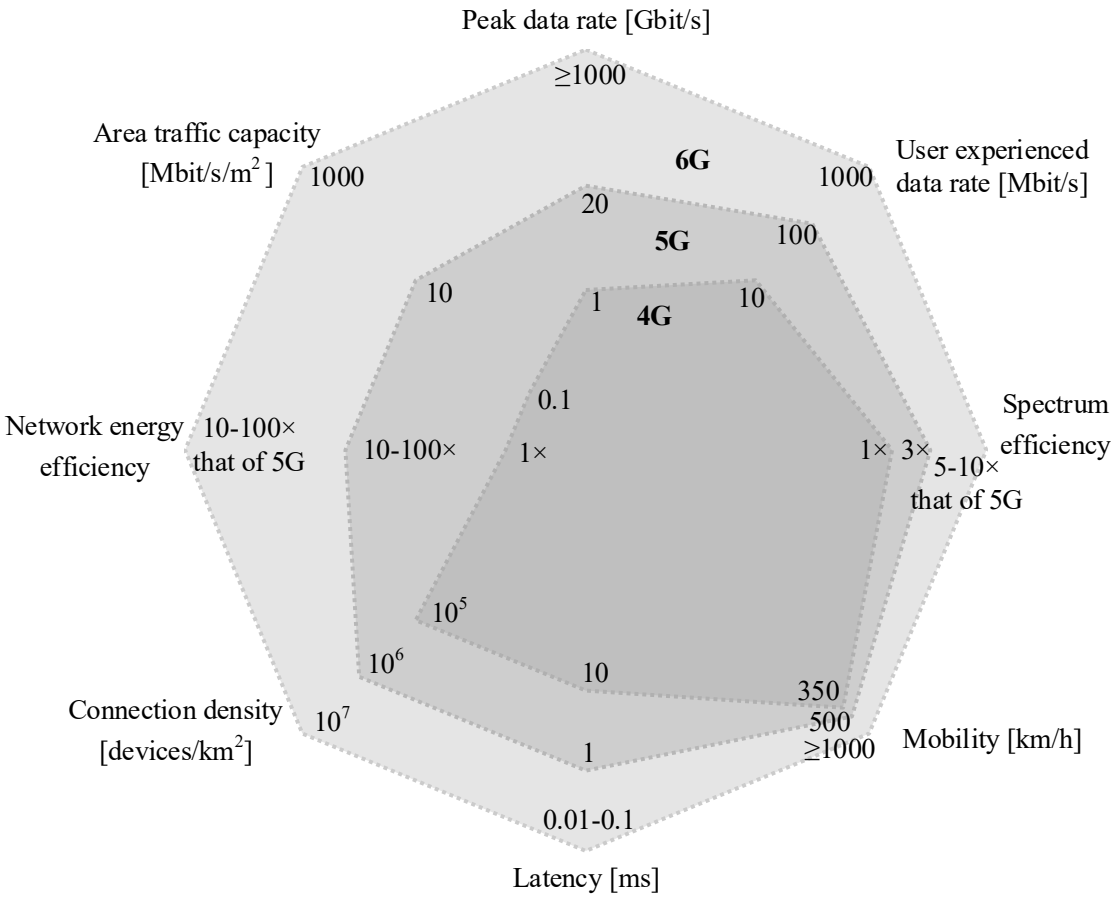

Fig. 1.1 Key capabilities of 4G, 5G, and 6G networks.

10 times higher data rate and connection density and 10-100 times higher energy efficiency. Moreover, the coverage will be improved from the current 70% in 5G to 99% in 6G [1]. The total number of Internet users is estimated to increase from 3.9 billion in 2018 to 5.3 billion by 2023 at a compound annual growth rate (CAGR) of 6%, representing 51% and 66% of the global population, respectively [7, Figure 1]. Machine-to-machine (M2M) connections will increase from 6.1 billion in 2018 to 14.7 billion by 2023 [7, Figure 4], which means 1.8 M2M connections per person by 2023.

Meanwhile, buildings have become the main scenes for data consumption. Among the fast-growing M2M connections, connected home applications will have the largest share, 48%, by 2023 [7, Figure 5]. As estimated in [8, Figure 1], for 5G networks, about 96% of the mobile data would be consumed at hotspots, work, and home, while only 4% of the mobile data would be consumed when "on the go". As most of the data traffic takes place indoors, the wireless network system has become one of the primary infrastructures for a modern

building. Consequently, improving the performance of indoor wireless networks is of vital importance.

Besides the network performance, the energy efficiency of indoor wireless networks has also drawn attention in both the wireless communication and building design industries. Globally, buildings account for about 30% of final energy use, and 28% of energy-related CO_2 emissions [9]. Meanwhile, wireless communications are already among the top energy consumers. At the EU level, the average annual specific consumption for buildings was about 180 kWh/m^2/year in 2013 [10]. Whereas, an indoor 5G network is estimated to consume 87.6 kWh/m^2/year as indicated in [11, Table 1], which can take a significant share in the total energy consumption. Moreover, a growing trend in the energy consumption of indoor wireless networks can be seen from technological advancements of future wireless communications [12]. Therefore, it is urgent to reduce the carbon footprint by reducing the power consumption of indoor wireless networks.

1.2 Motivations

Indoor propagation environments partitioned by walls, floors, and ceilings result in blockage effects on signals, and hence impact indoor network performance significantly. To enable mathematical tractability in indoor network performance evaluation, stochastic geometry has been widely employed in the literature, where the building structures were assumed to follow a random process to address the blockage effects [13]. However, the hypothetical indoor propagation scenarios do not correspond to actual building structures, leading to limited value of the stochastic geometry based methods in industrial practice. The conflict between the complexity of actual indoor environments and the tractability in blockage modelling in indoor wireless communications raises the question—how to better characterise the effects of a building in use? A tractable approach is desired to address blockage effects in actual indoor environments in three-dimensional (3-D) space.

Currently, building network performance and energy efficiency are optimised for existing buildings. To improve indoor network performance, radio engineers may adjust the network by increasing the number of transmit elements, optimizing the network deployment, or adopting performance enhancement schemes, such as coordinated multipoint (CoMP) transmissions [14, 15]. To improve the energy efficiency of wireless networks, the strategies of managing the system operation and adopting energy-efficient architectures, such as using relays and low power nodes, have been widely discussed [11]. However, building structures inevitably affect indoor wireless networks, leading to upper bounds on network performance and energy efficiency in a building [16, 17]. The potential constraints caused by building

structures can only be overcome by modifying or reconstructing the building itself. Consequently, it is necessary to consider the impact of building structures on indoor networks at the design stage of a building [18]. The concept of building wireless performance (BWP) has been introduced to quantify the effects of building structures on indoor network performance, which bridges the gap between building design and wireless communications [19–21]. In previous works, the analytical models of the PG and the IG were derived for single rooms on two-dimensional (2-D) planes, which means only the impact of the geometry of a single room was considered. However, there are other factors of building structures affecting indoor network performance, e.g., building materials and layouts, which raises the question—how to better characterise the effects of a building under design? The framework of the BWP is expected to be improved in terms of network models, environment models, and evaluation schemes to facilitate its practical applications for wireless-friendly building design.

1.3 Contributions of this Thesis

Chapter 3 proposes a 3-D line-of-sight (LOS) probability model to express the blockage effects in indoor network performance evaluation. The proposed analytical model in the closed-form expression can be used to compute the LOS probability in a 3-D environment based on the layout of a specific building. It addresses the cross-floor association/interference which was ignored in previous proposed 2-D approaches. The numerical results show that the proposed 3-D LOS probability model improves the accuracy of coverage probability of 3-D ultra dense small cell (UDS) networks in specific buildings.

Chapter 4 and Chapter 5 focus on the BWP evaluation. In the initial works [19–22], the BWP has been defined and evaluated for individual rooms on a 2-D plane. Chapter 4 introduces a partition-based BWP evaluation scheme. It accounts for the penetration loss using a partition-based path gain model. The analytical models for the BWP FoMs are given in closed-form expressions. Numerical results are generated to analyse the effects of penetration loss of walls on the distribution of the BWP in a typical office building. The proposed scheme can be employed to address the impact of building materials and layouts in the BWP evaluation.

Chapter 5 proposes a multi-storey BWP evaluation scheme. The BWP FoMs are defined for multi-storey buildings, and then the analytical models computing the FoMs are derived in closed-form expressions. Numerical results are generated for a typical multi-storey office building to observe the distribution of the BWP on different storeys. The proposed scheme can be employed to address the impact of 3-D building properties, including the number of

storeys and their height. The works in Chapter 4 and Chapter 5 are critical extensions of the BWP framework.

1.4 Structure of this Thesis

The structure of the rest of this thesis is introduced as follows.

Chapter 2: Literature Review

This chapter first reviews previous works in indoor wireless channel modelling and the tractable approaches for wireless network performance evaluation. Then it introduces the concept of the BWP and state-of-the-art works, including the definition of the FoMs, the system model, and the analytical approaches of the BWP evaluation.

Chapter 3: LOS Probability for Channel Modelling in 3-D Indoor Environments

This chapter proposes a 3-D indoor LOS probability model. The proposed analytical model in the closed-form expression can be used to compute the LOS probability in a 3-D environment based on the layout of a specific building. The proposed model is validated in both single rooms and a typical office building by Monte Carlo simulations. The coverage probability in a typical office building with a 3-D ultra dense small cell (UDS) network is evaluated based on the proposed LOS probability model. The numerical results are compared with those generated by 2-D empirical and plan-based LOS probability models in the literature.

Chapter 4: Partition-Based Analytic Evaluation of Building Wireless Performance

This chapter proposes a tractable approach to obtain the FoMs of the BWP with a partition-based path gain model. The proposed analytical models in closed-form expressions enable the BWP FoMs to capture the impact of both building materials and layouts on indoor wireless network performance. The BWP assessment is demonstrated in a typical office building.

Chapter 5: On Evaluation of Wireless Performance for Multi-Storey Buildings

This chapter proposes a multi-storey BWP evaluation scheme to address the effects of building structures on indoor wireless network performance in 3-D space. The BWP FoMs are defined for a multi-storey building and the analytical models to compute the FoMs are derived in closed-form expressions. The BWP analysis under a multi-storey system model is demonstrated in a typical office building. Numerical results are generated to observe the

variation of the BWP with the 3-D building properties, including the number of storeys and their height.

Chapter 6: Conclusion and Future Works

This chapter generates the conclusion of this thesis and introduces future works to study the effects of building structures on indoor wireless networks. Moreover, the open issues in BWP evaluation and optimisation regarding the system model, specific techniques, and experimental validation are summarised.

Chapter 2

Literature Review

Overview

This chapter first reviews previous works in indoor wireless channel modelling in the literature. Then the tractable approaches in wireless network performance evaluation are reviewed from outdoor scenarios to indoor scenarios. Moreover, it introduces the novel concept of the BWP and state-of-the-art works, including the definition of the FoMs, the system model, and the analytical approaches of the BWP evaluation.

2.1 Review in Indoor Network Performance Evaluation

2.1.1 Indoor wireless channel modelling

Indoor environments comprising walls, floors, ceilings, furniture, and moving persons result in various propagation behaviours, including transmission, reflection, diffuse scattering, and diffraction, of electromagnetic (EM) waves. Consequently, compared to outdoors, it is more difficult to characterise the received signals accurately in indoor scenarios. Two types of indoor channel models, the statistical and the deterministic channel models, to compute the received signal strength at indoor receivers are introduced in this section.

Statistical indoor wireless channel modelling

The statistical channel models are obtained by curve fitting to the measured data from practical environments and then applied to similar scenarios assuming that they are generally valid, where the decibel-scaled shadow fading is normally represented by a zero-mean Gaussian random variable. They have been reported in the literature for various indoor

environments based on the measurements in multiple frequency bands, such as the office environment at 28, 60 and 73 GHz in [23–25], the laboratory environment at 2-40 GHz in [26], the library environment at 28 GHz in [27], the hospital environment at 60 GHz in [28], the corridor and office environments at 8-11 GHz in [29], the factory, corridor, classroom, PC lab environments at 54 and 70 GHz in [30], etc. There are two basic types of statistical channel models, including the close-in (CI) free space reference distance path loss model and the floating intercept (FI) path loss model. The CI free space reference distance path loss model captures the frequency- and distance-dependency of path loss by the free space path loss (FSPL) of a reference CI distance and the path loss exponent (PLE), respectively [31]. The FI path loss model is obtained without a physically-based anchor, which addresses the distance-dependency of path loss in a given frequency band [32]. When applied to a wide frequency range, it can be extended to the alpha-beta-gamma (ABG) path loss model including a frequency-dependent factor [33, 34]. The statistical channel models show limited accuracy in radio propagation prediction without considering specific building structures. To improve the accuracy, the partition-based statistical channel models have been proposed, where the penetration loss is denoted by an additive factor site-specifically [35]. For example, a multi-wall-and-floor model was proposed in [36], where the penetration loss on a transmitter-receiver (Tx-Rx) link was represented as a function of the exact number of walls and floors intersected. Moreover, the penetration loss of obstacles in an indoor environment has been further specified according to the type of obstacles [37], the thickness of obstacles [38], and the incident angle of a Tx-Rx link [39]. The partition-based models show increased complexity in radio propagation prediction as they require extra input parameters.

Deterministic indoor wireless channel modelling

Deterministic methods, such as ray tracing (RT) and ray launching (RL), are considered promising for accurate radio propagation prediction in complex indoor environments. They approximate radio propagation in a 3-D environment model following the geometrical optic (GO) rules site-specifically. EM waves are represented by rays radiated through infinitely small tubes in a homogeneous medium and their trajectories are represented by straight lines [40]. The rays carry energy and follow the laws of the propagation mechanisms, including LOS, transmission, reflection, diffuse scattering, and diffraction. For RT, the rays are traced specifically for given locations of transmitters and receivers [41]. For RL, the 3-D propagation environment model is discretised into unit sections representing the possible reception locations [42]. Analytical models have been proposed in the literature to compute the path gain resulted from different propagation mechanisms.

Reflection occurs when EM waves hit an obstacle with much larger dimensions compared to the wavelength. In the literature, the reflection and transmission loss of common building materials have been measured in multiple frequency bands, such as the 26.5- to 40-GHz bands in [43], the 28-GHz band in [44, 45], the 38-GHz band in [45], the 60-GHz band in [46], and the 73-GHz band in [47], etc. A comprehensive review of the measured transmission loss of common indoor building materials have been given in [48, TABLE 5] at 900 MHz-10 THz. The relative permittivity of a building material can be estimated based on the relationships of the reflection and transmission loss and the thickness of the material, the incident angle, and the EM wave carrier frequency. The relative permittivity for common building materials, such as concrete, wood, glass, plasterboard, and brick, has been obtained in previous works, including [49] at 41.5 GHz, [50] at 39 GHz, [51] at 57.5 GHz, [52] at 59.5 GHz, [53, 54] at 60 GHz, [55] at 62.4 GHz, etc. In [56] and [57], the EM properties of common building materials obtained from measurements at 2-62.4 GHz and 200 MHz-67 GHz were reviewed, respectively. Moreover, based on measured data in the literature, the relative permittivity of multiple building materials was summarised in the ITU standards [58, Table 3] for the frequency range from 1 MHz-100 GHz. In ray-based radio prediction tools, the transmission loss and reflection loss can be computed based on the Fresnel equation when the EM properties of building materials have been inserted in 3-D environment models [41].

Diffraction is triggered when EM waves meet the edge of an obstacle [59]. Various objects in indoor scenarios may introduce diffraction rays, such as screens, cabinets, tables, left-open doors, and persons. To enable the computation of diffraction loss in ray-based radio prediction tools, the practical objects should be idealised to simple geometries, such as a knife edge with negligible thickness, a smooth circular cylinder, or a finitely conducting wedge. Then the diffraction models, such as knife edge diffraction (KED) [60] and uniform theory of diffraction (UTD) [61], can be adapted according to the geometries of the objects, where the KED model applies to edges and the UTD model additionally applies to wedges and cylinders. Propagation measurements in multiple frequency bands have been conducted to validate the effectiveness of the KED and UTD models in indoor scenarios. In [62], the diffraction loss was measured for indoor building materials, which included the drywall corner, wooden corner, and plastic board, with different diffraction angles at 10, 20, and 26 GHz and compared with simulations based on the KED model. In [63], the diffraction loss at an edge, a wedge, and a cylinder were measured and compared with simulations based on both the KED and UTD model at 60 and 300 GHz. A double KED model was extended from the KED model to describe the diffraction due to persons and compared to the measured data at 4–10 GHz and 73 GHz in [64] and [62], respectively. A thorough overview of the diffraction scenarios and corresponding models was introduced in the ITU standards [65].

The diffraction models have been integrated into the ray-based radio prediction tools for indoor scenarios [66, 67]. Moreover, simplified expressions of the models and mathematical approximations of the UTD coefficients have been proposed in the literature to further facilitate engineering applications of ray-based radio predication tools [68–70].

Diffuse scattering happens when EM waves interact with rough surfaces. The effects of diffuse scattering are more pronounced as the carrier frequency goes mmWave bands and above since the roughness of the surfaces become comparable to the wavelength [48]. To characterise diffuse scattering in ray-based radio prediction tools, an effective roughness (ER) diffuse scattering model was developed in [71, 72]. The ER model was further developed into sub-models based on different scattering patterns, including the Lambertian model, the directive model, and the back scattering-lobe model [73]. The directive model and Lambertian model have been implemented in ray-based radio prediction tools to explore their effectiveness in indoor scenarios on various frequency bands, such as the warehouse scenario at 1.9 GHz in [74], office scenario at 3.6 GHz in [74], conference room at 23.5 GHz in [75], office scenario at 26 GHz in [76], and office and hospital scenarios at 60 GHz in [77], where the parameters of the models were fitted from measured data without considering the heterogeneous nature of elements in an indoor propagation environment. In [78], different elements in the environment were associated with specific parameter values according to their roughness, which increased the prediction accuracy at 60 GHz in a laboratory scenario. Based on [78], the best fitting parameters for the ER-based diffuse scattering models were estimated for typical indoor building materials at 40-50 GHz and 60 GHz in [79] and [80, 81], respectively. Validation results showed that the ER-based diffuse scattering models parameterised according to specific building materials could further improve the accuracy of radio prediction.

The deterministic methods have been widely employed in indoor radio prediction and have shown high accuracy in various indoor scenarios compared to measurement results. It can be seen from the above-mentioned previous works that the accuracy of deterministic channel modelling lies in the accuracy of the 3-D environment model composed of the layout of the environment and the EM properties of building materials. Intuitively, the more detailed the propagation environment is described, the higher accuracy a ray-based radio prediction may achieve. Correspondingly, the prediction under a detailed environment model raises computation complexity and requires a large computer memory occupation.

Summary

The received signal strength at the user equipment (UE) is fundamental to compute the signal-to-interference-plus-noise ratio (SINR) and hence fundamental to obtain the network

performance metrics, such as the coverage/outage probability and the capacity. It can be computed by both the statistical channel models and the deterministic radio propagation prediction approaches. The statistical channel models with simple expressions can be employed to enable tractability in analytical network performance evaluation schemes. The deterministic approaches show high prediction accuracy by introducing the site-specific information. However, they require much information on propagation environments, while the prediction results are only valid in a specific propagation environment with predefined network architectures and the corresponding practical deployment and configurations. When applied in network deployment optimisation or systematic analysis of the impact of building structures on indoor network performance, the deterministic approaches may result in enormous computation complexity and time consumption.

2.1.2 Tractable approaches for network performance evaluation

To enable the tractability of network performance evaluation, various analytical approaches have been brought up in the literature based on different assumptions of propagation environments and network deployments. They were first applied to outdoor cellulars and then extended to indoor networks. This section reviews the tractable approaches for network performance evaluation from outdoors to indoors.

Exact cell geometry layout

In the 2G/3G era, the indoor and outdoor scenarios were not distinguished in the network performance evaluation since indoor users were mainly served by outdoor base stations (BSs). Exact cell geometry layouts, e.g., the one-dimensional (1-D) linear and 2-D hexagonal cellular patterns, were commonly used to approximate the layouts of multi-cell networks. Under 2-D hexagonal cellular patterns, where a BS was assumed to be fixed on the centre of a hexagon representing the coverage area, the network performance was evaluated in terms of the maximum number of users supportable per cell in [82] and the signal-to-interference ratio (SIR) on the edge of a hexagonal coverage area, i.e., the worst-case performance, in [60]. To enable the Shannon-theoretic approach of network capacity analysis, the Wyner model was developed in [83] to evaluate the network performance in terms of the achievable rate. Instead of computing the distance-dependent decay for each Tx-Rx link, it represented the path gain of the signals transmitted from the adjacent cells by a single parameter α, where $0 \leq \alpha \leq 1$. The Wyner model was further generalised by accounting for small-scale fading, e.g., Rayleigh fading, in [84–86]. Although the Wyner model is tractable, it is overly simplified and idealistic.

Stochastic geometry in network performance evaluation

In practical environments, cellular networks can not be deployed following exact geometry layouts due to terrain, political, and economic constraints. Moreover, cellular networks have become less regular as indoor small base stations (SBSs) have been deployed to complement the coverage of outdoor BSs since the 4G era. The distribution of BSs in a dense network shows similar features as spatial point processes. Numerical results in [87] show that the performance of a cellular network with a hexagonal cellular pattern and homogeneous Poisson point process (PPP) distributed BSs on 2-D planes provide upper and lower bounds to practical network performance, respectively. As argued in [88], the stochastic geometry tools and random graph theory facilitate mathematical tractability in deriving key network performance metrics, e.g., connectivity, coverage/outage probability, and capacity, under the assumption of randomly placed BSs following a spatial point process.

In [89], homogeneous PPP distributed BSs were assumed for an urban cellular network, based on which the analytical models of the SINR coverage probability and the average achievable rate were obtained. In addition to the homogenous PPP, different point processes characterising the spatial correlation among BSs have been applied to better represent the network deployment in practice. For example, the determinantal point process (DPP) was employed to express the repulsiveness among outdoor macro BSs [90, 91] and the Poisson cluster process (PCP) was employed to model SBSs clustered around hotspots in urban scenarios [92].

The stochastic geometry based approaches have been extended to evaluate heterogeneous networks (HetNets) comprising irregular infrastructure elements, including macro-, micro-, pico-, femtocells, etc. In [93, 94], a K-tier HetNet was analytically modeled and evaluated in terms of the SINR statistics, outage probability, and average achievable rate, where the BSs on each tier were PPP distributed and assigned with individual transmit power, supported data rate, and spatial density. The spatial correlation among BSs has also been considered in performance analysis of HetNets. In [95], a PCP was employed to model the BS distribution for each tier in a K-tier HetNet. In [96], the BSs in the first tier of a 2-tier HetNet model were assumed PPP distributed. Two cases, a Poisson hole process (PHP) and a PCP, were assumed for BSs in the second tier considering the inter- and intra-tier dependence of BSs, respectively. In [97], the distributions of BSs in a 2-tier HetNet were modeled by a Poisson hard-core process (PHCP) and a PPP for the first and second tier, respectively, where the PHCP was used to exhibit the repulsiveness among outdoor macro BSs.

When discussing networks in dense urban environments composed of high-rise buildings, it is worth analyzing the network performance in 3-D space since BSs are deployed on different heights. The work in [98] showed that the characteristics of an actual network in

a high-rise centre environment were identical to a 3-D homogeneous PPP. The coverage probabilities obtained assuming 2-D and 3-D PPP distributed BSs were compared to the network performance in practice, which showed that 3-D PPP could provide a closer bound to the practical network performance in dense urban environments. In [99], 3-D PCP distributed BSs were considered to reflect the property of clustering for small cells in 3-D space. In [100, 101], a Matérn hard-core point process (MHCP) was employed to model the BS distribution for each tier in a K-tier HetNet in 3-D space.

In the studies mentioned above, blockage effects caused by buildings in urban environments were either ignored or included in an additive shadow fading factor on a 2-D planer. In 3-D space, the floor attenuation for high-rise buildings was denoted by a constant or a factor linearly increasing with the propagation distance. As the carrier frequency goes higher for future wireless networks, the blockage effects of obstacles in propagation environments may significantly impact network performance. There have been various models proposed in the literature to better reflect the blockage effects in outdoor and indoor network performance evaluation schemes, which will be introduced in the following sections.

LOS probability

A Tx-Rx link in a propagation environment is a LOS link if it reaches the UE without any presence of obstacles; otherwise, it is a non-line-of-sight (NLOS) link. One of the practical approaches to express blockage effects is to distinguish LOS and NLOS Tx-Rx links and compute their path loss by different PLEs separately. Then it is important to know the LOS probability in a given propagation environment.

The empirical LOS probability models obtained from measured data have been given in the 3GPP and WINNER standards for various outdoor and indoor scenarios and then applied to different environments assuming that they are generally valid. As given in [102, Table 7.4.2-1] and [32, Table 4-7], they are piece-wise and each piece is a function about the propagation distance. In network performance evaluation, they have been approximated by more straightforward expressions for simplicity, such as a linear or exponential function about the propagation distance or a step function with a threshold length of LOS Tx-Rx links [16, 103, 104].

The network performance evaluation could generate different results from previous works when distinguishing the LOS and NLOS links in the system model. For example, when all the Tx-Rx links in a network with homogeneous PPP distributed BSs were computed with the same PLE as in [89], the coverage probability and the area spectral efficiency (ASE) grew monotonically as the density of the BSs increased. When different PLEs were assigned to LOS and NLOS links as in [16], a threshold of the BS density existed, exceeding which

the coverage probability decreased and the ASE decreased or suffered from slow growth. It is due to the fact that the interference signals could change from NLOS to LOS as the BS density increased. The difference resulted from distinguishing LOS and NLOS links in the system model has stressed the necessity of considering the blockage effects in network performance evaluation.

The blockage effects become more pronounced indoors due to complex building layouts. Besides the measurement-based empirical models [32, 102], the plan-based indoor LOS probability models have been derived in the literature. In [105], the LOS probability model was derived according to the exact building layout consisting of rectangular rooms on a 2-D plane. In [106], a machine learning based LOS probability model was developed based on the model proposed in [105], which could predict the LOS probability by the statistical features of a given building. The plan-based models present improved accuracy by inducing the information of a specific propagation environment.

Random blockages in urban environments

Besides considering the LOS probability in a specific environment or environments of the same category, the blockage effects could also be modeled by assuming a propagation environment consisting of randomly distributed blockages. In the benchmark work [13], a Boolean scheme of rectangles was defined to represent buildings in urban scenarios, which follows

- PPP distributed centre points,
- independent length, width, and shapes for each object, and
- random and independent orientations, locations, and sizes for all objects.

Combining the Boolean scheme assumption for the blockages and the PPP distributed BSs, the LOS probability of a Tx-Rx link can be denoted by a formula about the link length and the density and dimensions of buildings. The analytical models of key network performance metrics, e.g., connectivity, coverage/outage probability, and capacity, have been obtained under the Boolean scheme assumption. The numerical results showed that the blockages might help to improve the network performance by blocking more interference than intended signals. Moreover, the coverage probability and the ASE might be degraded as the density of BSs increases, for that the number of LOS interferers increases.

The Boolean scheme of rectangles has also been modified to the Boolean scheme of line segments and circles to enable tractability or represent blockages of different shapes. In [107], the LOS probability gain for a millimetre wave (mmWave) cellular network with

macro-diversity (the UE attempts to connect to two or more BSs simultaneously) was derived assuming that the blockages follow the Boolean scheme of line segments. In [108], the coverage probability of a 2-tier HetNet consisting of indoor and outdoor BSs was derived, where the Boolean scheme of circles was employed to represent the buildings. In [109], the Boolean scheme of circles was employed to represent the blockages in a finite circular area for a mmWave network. For indoor scenarios, the Boolean scheme of line segments and circles have been widely applied to denote interior walls and persons, respectively, which will be introduced in the following section.

The network performance evaluation under the Boolean scheme assumption was compared to it considering actual buildings in [13, 107, 110, 111]. Numerical results indicated that the network performance under the Boolean scheme assumption approximated it in practical scenarios well. Compared with the lattice model [112], the Boolean scheme assumption approximated the practical scenarios better for inducing random sizes and locations of the blockages [13].

Random blockages in indoor environments on a 2-D plane

The idea of randomly distributed blockages has also been widely used in indoor environments. In [113], the Boolean scheme of line segments has been applied to model the walls in a building, where line segments were with PPP distributed centres, uniformly distributed length, and random orientations. To better approximate practical building layouts, the Boolean scheme assumption has been modified in [17, 114–116], where the walls have been assumed binary oriented. In [114, 117], the Manhattan Poisson line process (MPLP) has also been employed to model the walls by a grid. Besides, when studying the impact of human bodies, the persons were assumed as cylinders where the centres of the bottom circles are homogeneous PPP distributed [118]. These assumptions have introduced stochastic geometry tools in indoor wireless network evaluation considering indoor obstacles.

The coverage probability has been analysed under different assumptions of user locations, BS locations, and blockage distributions. In [17, 113, 118], the network performance for a typical user at the origin of the 2-D Euclidean space was evaluated, where BSs were assumed homogeneous PPP distributed. Numerical results derived for a typical user showed that the coverage probability varied with general building structure parameters, e.g., the blockage density and the average wall attenuation factor, and general network parameters, e.g., the BS density. In [114, 115], two determined arrangements of transmitters were assumed, where the transmitters were located on the vertices of squares and rhomboids with predetermined dimensions. The receiver was located at a fixed distance from the intended transmitter while

the other transmitters were considered interferers, representing the cell-edge scenario to investigate the effects of the relative angles of Tx-Rx links to the walls.

Random blockages in indoor environments in 3-D space

To better approximate realistic environments in indoor network performance evaluation, the multi-storey structures have been considered in the system model, where the BSs were deployed on parallel planes and the floor penetration loss was considered. Under the multi-storey assumption, there have been multiple association schemes, including the single-floor strongest association, single-floor closest association, cross-floor strongest association, and cross-floor closest association. In [119–121], BSs on each floor were assumed homogeneous PPP distributed. Then the effects of the storey height, BS density, and floor penetration loss on the network performance for a typical user with different association schemes were systematically analysed. In [119], single-floor closest association and the cross-floor strongest association were compared in terms of the SIR coverage probability. The SIR coverage probability grew monotonically as the BS density increased for the single-floor closest association, while it did not change with the BS density for the cross-floor strongest association. In [120, 121], the SINR coverage probability for a multi-storey PPP distributed network was obtained. Numerical results showed that, for the cross-floor strongest association, the SINR coverage probability might first decrease and then increase as the storey height and the BS density increased. As the floor penetration loss increased, the coverage probability might first increase and then decrease for the cross-floor strongest association, while it increased monotonically for single-floor associations. In addition to the homogeneous PPP, a MHCP was employed to model the BS distribution on each floor in [122]. Similar to PPP distributed network models, a floor penetration loss corresponding to the highest SINR coverage probability could exist for the cross-floor strongest association, while a larger floor penetration loss benefited the SINR coverage probability for the single-floor association.

In addition to the multi-storey structures, a 3-D Poisson grid following the MPLP was employed to model the building layout in [123]. All BSs were assumed on the edges of the rooms following a homogeneous PPP which well approximated the practical scenarios. Another approach to address the effects of walls was made in [124], where the coverage probability for a typical user was derived assuming that BSs were distributed following a 3-D homogeneous PPP and equally spaced walls were assumed on each Tx-Rx link. Numerical results in both [123] and [124] also showed that a larger penetration loss could result in an increased coverage probability.

Summary

In this section, the tractable approaches of network performance evaluation proposed in the literature have been reviewed. The exact cell geometry layout, especially the 2-D hexagonal cellular pattern, has been universally adopted to represent the coverage area of each BS in a multi-cell network. Based on the exact cell geometry layout, the Wyner model was developed to enable the network performance evaluation in terms of the achievable rate. It lays the fundamentals of analytical network performance evaluations but is overly simple and idealistic. The stochastic geometry tools have been introduced in network performance evaluation by assuming that BS locations follow spatial point processes, such as homogeneous PPP, PCP, HCP, etc. The randomness of BSs, on the one hand, enables mathematical tractability and, on the other hand, approximates the practical network deployments. Benefitted from assumptions of the network model, the network deployment can be represented by general parameters, such as the BS density. When targeting dense urban areas or indoor scenarios, the blockage effects impact the network performance significantly. To maintain the tractability of network evaluation schemes while addressing the blockage effects, the randomness has also been assigned to the blockages, such as assuming the distribution of blockages as the Boolean scheme. With the assumptions of the blockages, the propagation environment can be described by general parameters, such as the blockage density, the storey height, and the average wall attenuation factor. Then the dependence between network deployments and propagation environments has been discussed. It motivated the development of the novel concept of the BWP, which will be introduced in the next section.

The strength of the randomly distributed blockage assumption is also its weakness. The assumed random blockage models facilitate the tractability of network performance but do not correspond to practical building structures. In previous works, the plan-based LOS probability models were derived according to the actual building layout on a 2-D plane, where the height difference between the transmitter and the receiver and cross-floor associations/interference were not considered. Thus, an exact 3-D LOS probability model is desired to address the blockage effects in a specific building and improve the accuracy of the network performance evaluation, which motivates the work in Chapter 3.

2.2 Related Works in BWP

2.2.1 Effects of building structures on indoor network performance

Indoor wireless network performance is significantly impacted by building structures, including building materials and layouts. In practice, the transmit elements, such as the SBSs

of UDS networks and antennas of distributive massive multiple-input and multiple-output (MIMO) systems, are mounted on ceilings or walls for maximum coverage and visual impact. The scale of transmit elements needs to be adjusted according to the traffic demands in a room, which is decided by its dimensions and utility. Consequently, indoor network deployments, including the number and the installation locations of the transmit elements, are constrained by building layouts. As discussed in the previous sections of this chapter, obstacles in indoor environments result in various propagation behaviours of EM waves, which affect the received signal strength. The enhancement or attenuation on the strength of intended signals or interference signals affects the SINR, hence the network performance, such as the coverage probability and data rate. General analysis shows that non-linear dependence exists between network deployments and propagation environments.

Since building structures inevitably affect indoor wireless network performance, the impact should be considered at the design stage of a building, but it is not able to be quantified by neither of the existing network performance evaluation schemes. The statistical channel models and the stochastic geometry based approaches do not correspond to specific building structures. The deterministic channel modelling approaches only apply to a specific network solution with predefined network architectures and the corresponding practical deployment and configurations. If assessing the indoor wireless network performance by the deterministic approaches at the building design stage to circumvent the constraints imposed by the building structures, all the possible combinations of wireless network solutions and building designs have to be simulated. Consequently, it is not feasible due to enormous computational cost and time consumption.

2.2.2 Definitions of BWP FoMs

To quantify the effects of building structures on the indoor network performance, two figures of merit (FoMs) were introduced in [20], which were referred to as the interference gain (IG) and the power gain (PG). They were defined by comparing the indoor network performance to the network performance in a benchmark scenario where both the targeted UE and transmit elements are located in open space.

The SINR in the open-space scenario is denoted by $\gamma_{\mathrm{O}} = P_{\mathrm{O}}/\left(I_{\mathrm{O}} + \sigma^2\right)$, and the SINR in the in-building scenario is denoted by $\gamma_{\mathrm{B}} = P_{\mathrm{B}}/\left(I_{\mathrm{B}} + \sigma^2\right)$, where P_{O} and P_{B} denote the total received intended signal power in the open-space scenario and the in-building scenario, respectively, I_{O} and I_{B} denote the total received interference power in the open-space scenario and the in-building scenario, respectively, and σ^2 represents the thermal noise power. The BWP FoMs capture the wireless network performance gain resulted from placing a building with specific structures in open space. The PG and the IG are defined as

- $g_{\mathrm{P}} \triangleq P_{\mathrm{B}}/P_{\mathrm{O}}$, and
- $g_{\mathrm{I}} \triangleq \left(I_{\mathrm{O}}+\sigma^2\right)/\left(I_{\mathrm{B}}+\sigma^2\right)$,

which indicate the effective change of the desired and undesired power received by a probing UE due to the presence of a building, respectively. Higher PG means that less intended signal power is degraded by the building structures and higher IG means that more interference power is blocked by the building structures. According to the definitions of the PG and the IG, there is the relationship $\gamma_{\mathrm{B}} = g_{\mathrm{P}} g_{\mathrm{I}} \gamma_{\mathrm{O}}$ between the product of the PG and the IG and the SINRs in a probing UE location in a given building and open space. With the definitions of the FoMs, designing a building accommodating to a well-performed and energy-efficient wireless network can be conducted by adjusting the building structures to achieve good BWP with high PG and IG values. The FoMs can be employed in the building design as the indicators to assess a building in terms of its BWP.

2.2.3 BWP evaluation approaches proposed in previous works

In previous works [19–22], the framework has captured the intrinsic BWP by quantifying the effective change of the maximum achievable performance gain from open space to indoors. A general and idealistic network model has been employed to present the maximum network performance and eliminate the effects of different network deployments, which follows the assumptions:

a) an infinite number of transmit elements are uniformly distributed on a 2-D plane;

b) the targeted UE makes use of all the detectable signals whose power exceeds a threshold decided by the sensitivity of the receive device; and

c) the PLEs are respectively defined for LOS and NLOS Tx-Rx links.

For downlink transmissions, the transmit elements could be considered as SBSs forming an UDS network or array antennas in a distributed massive MIMO system. With assumption a), a significantly densified network is approximated by a network with infinitely densely distributed transmit elements. Assumption b) comes from the network performance enhancement schemes, such as maximum ratio transmissions (MRT) for distributed massive MIMO networks or CoMP transmissions for UDS networks.

The assumptions addressed the network performance gain from network densification and network performance enhancement schemes. The network model consisted of primary network parameters, including the transmit power, maximum detectable signal strength

decided by the sensitivity of the receive device, and the carrier frequency. The LOS and NLOS Tx-Rx links were distinguished by the presence of walls and assigned with different PLEs to compute the received signal strength, respectively.

By constructing an idealistic network model presenting the maximum achievable network performance gain, analytical models were derived in closed-form expressions to derive the PG and the IG computational efficiently [20]. Observations in single rectangular rooms show that room sizes and aspect ratios impact the BWP significantly. Based on [19, 20], [22] focused on the IG and proposed a tractable method optimizing the network configurations to maximise the average IG of a given building under design. The numerical results in previous works have shown the potential of the BWP framework.

2.2.4 Research challenges in BWP

The concept of BWP is designed to describe the wireless friendliness of buildings in the real world. One of the key factors to make BWP evaluation and optimisation employed in the industry is that they should generally apply to different buildings and consider practical building structures. The BWP evaluation approaches proposed in previous works have restricted the building structures impacting indoor wireless network performance to the geometry of each room on a 2-D plane. Consequently, many other parameters of building structures were omitted in the BWP evaluation. It motivates the works in Chapter 4 and Chapter 5, which are the extensions of the BWP framework with more practical system models to address the effects of building materials, relative locations of rooms, the number of storeys and their height. Beyond the scope of this thesis, there are more open issues in this research which will be discussed in Chapter 6.

Chapter 3

Line-of-Sight Probability for Channel Modelling in 3-D Indoor Environments

Overview

The probability of having a LOS channel from the transmitter to the receiver, i.e., the LOS probability, is a critical indicator of the blockage effects for wireless networks. Indoor LOS probability models proposed in the literature were either empirical or plan-based, where the empirical models were obtained from the measured data and the plan-based models were derived according to the indoor layout of a single storey of a building. The empirical models were applied to different scenarios assuming that they were generally valid, and thereby showed limited accuracy due to the lack of the information of specific propagation environments. The plan-based models proposed in previous works presented an improved accuracy compared to the empirical models. However, they only apply to 2-D single-storey scenarios because the cross-floor associations/interference were not considering. This chapter proposes a 3-D indoor LOS probability model, which can be used to compute the LOS probability in a 3-D environment according to the layout of a specific building. The model is validated by the Monte Carlo simulations in both single rooms and a typical office building. Moreover, the coverage probability in the office building with a 3-D UDS network is evaluated based on the proposed LOS probability model. The proposed model can be employed in indoor network performance evaluation and optimisation.

3.1 Introduction

3.1.1 Background and motivations

For wireless communications, the blockage effects caused by the obstacles intersecting the propagation path between the transmitter and the receiver may attenuate the signal significantly. Especially on the mmWave bands, signals are more vulnerable to the blockage effects resulted from the propagation characteristics [23]. In indoor environments, the blockage effects become more pronounced due to complex layouts of buildings. A practical approach to express the blockage effects in the network performance evaluation is to distinguish LOS and NLOS Tx-Rx links and compute their path loss by different PLEs separately [103, 125]. Therefore, the probability that the signal reaches the UE with a LOS path in a given propagation environment, i.e., the LOS probability, is critical and has been incorporated in various network performance evaluation schemes [16, 104].

In the literature, indoor LOS probability models are either empirical or plan-based. The empirical models were obtained from the measured data and then applied to different scenarios assuming that they were generally valid [32, 102]. The plan-based models were derived according to the indoor layout of each building and presented an improved accuracy by inducing the information of the specific propagation environment [105, 106]. The above-mentioned models were derived assuming that both the UEs and the BSs have fixed heights, i.e., only apply to 2-D single-storey scenarios and corresponding propagation models.

As the indoor data traffic increases rapidly [126, 127], the BSs are densely and flexibly deployed indoors to satisfy the diversified user demands. Consequently, the overall network performance evaluation for a multi-storey building should be conducted in the 3-D space since the cross-floor association/interference exists. The work in [98] shows that the characteristics of the actual network deployment in urban buildings are identical to a 3-D homogeneous PPP. Thus, the network performance metrics, such as the coverage probability, can be analytically derived by employing the 3-D homogeneous PPP distributed BSs to represent the practical network deployment. This approach has been used in the 3-D network performance evaluation [98, 124]. However, the indoor blockage effects are either ignored [98] or represented by certain idealistic assumptions, such as the equally-spaced walls [124]. Since the 2-D models are invalid in a 3-D space, an exact 3-D LOS probability model is desired to address the blockage effects in a specific building and improve the accuracy of the network performance evaluation.

3.1.2 Contributions in this chapter

This chapter proposes an approach to compute the LOS probability for buildings in 3-D space. The LOS probability of a typical Tx-Rx link knowing its length can then be derived analytically given the dimensions of a building. The derived analytical model is validated in both single rooms and a typical office building by Monte Carlo simulations. Assuming a one-tier dense homogeneous network, the coverage probability in the building is also computed based on the proposed model. Taking both the 2-D empirical models in [32, 102] and the 2-D plan-based model in [105] as the benchmarks, the numerical results of the LOS probability and the coverage probability in a typical office building are compared and analysed.

3.2 Analytical Model of LOS Probability

3.2.1 System model

In an indoor environment, the walls, floors and ceilings, which are mainly constructed with heavy concrete, attenuate signals significantly. Therefore, a typical room is represented by a rectangular cuboid and the ceiling, floor and walls of this room are denoted by the faces of the cuboid. A building consisting of rooms with different dimensions can be considered as a structure composed of cuboids. For simplicity, rooms in the building are considered empty without any furniture or person. The UE is assumed to be randomly and uniformly distributed in the building. The link length R [m] is the Euclidean distance between a BS and the UE with the range $(0, +\infty)$. The LOS probability in a building is defined as the probability that a signal propagates from the BS to the UE without any presence of walls, floors or ceilings. The dimensions of a room are given by the length L [m], the width W [m] and the height H [m], which are perpendicular to the XZ-plane, YZ-plane and XY-plane, respectively. Without losing generality, assume that $H \leq W \leq L$ for each room. In this section, the LOS probability model is first derived for a single room and then derived for a building.

3.2.2 3-D LOS probability in a single room

Based on the system model described above, this subsection presents the 3-D LOS probability model for a single room. As shown in Fig. 3.1, a Tx-Rx link is considered as a NLOS link if it is intersected by an arbitrary face of the room. Otherwise, it is a LOS link. The locations of the UE end and the BS end are given by the coordinates $(x_\mathrm{r}, y_\mathrm{r}, z_\mathrm{r})$ and $(x_\mathrm{t}, y_\mathrm{t}, z_\mathrm{t})$,

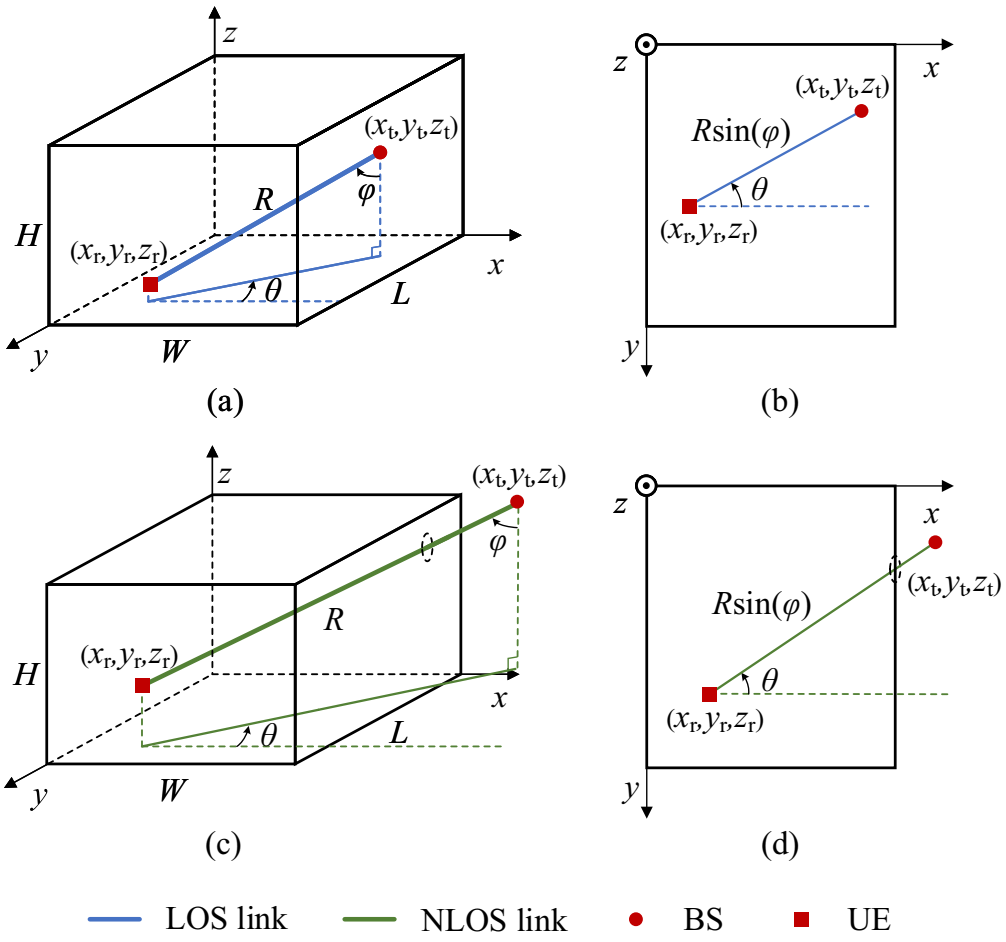

Fig. 3.1 (a) A LOS link in a typical room of a building. (b) The projection of the LOS link on the XY-plane. (c) A NLOS link in a typical room of a building. (d) The projection of the NLOS link on the XY-plane.

respectively, in the 3-D Cartesian coordinate system. The length of the projections of the Tx-Rx link on the x-axis, y-axis and z-axis are denoted by x, y and z, which can be obtained by $x = |x_t - x_r|$, $y = |y_t - y_r|$, and $z = |z_t - z_r|$, respectively. Define two angles, φ and θ, to describe the direction of each link in 3-D space. As shown in Fig. 3.1, θ denotes the angle of the projection on the XY-plane, while φ is the angle on the plane defined by the Tx-Rx link and its projection on the XY-plane.

Theorem 3.1. *The joint probability density function (PDF) of the length of the projections and the angles for a Tx-Rx link in a room is given by*

$$f(x,y,z,\varphi,\theta) = \begin{cases} \frac{4}{\pi^2 HWL}, & (x,y,z,\varphi,\theta) \in \Omega, \\ 0, & \text{else}, \end{cases} \tag{3.1}$$

where $\Omega = \{(x,y,z,\varphi,\theta) | (0<x<W) \wedge (0<y<L) \wedge (0<z<H) \wedge (0<\theta<\frac{\pi}{2}) \wedge (0<\varphi<\frac{\pi}{2})\}$ *and "$\wedge$" denotes the logical conjunction.*

Proof: According to the definitions in the system model, there are the distributions $\theta \sim U\left(0,\frac{\pi}{2}\right)$, $\varphi \sim U\left(0,\frac{\pi}{2}\right)$, $x \sim U(0,W)$, $y \sim U(0,L)$, and $z \sim U(0,H)$, where $U(\cdot)$ denotes the uniform distribution. The distributions of the angles (φ, θ) and the length of the projections (x, y, z) of the Tx-Rx link are all independent from each other. Thus the joint PDF is the product of their distributions. ■

Theorem 3.2. *For a Tx-Rx link with link length R, its LOS probability in a 3-D room with the dimension $H \times W \times L$ can be derived by*

$$\Pr_{\text{LOS}}(R) = q_0 + \int_{\varphi_3}^{\varphi_4} \mathscr{W}_1(\varphi)\mathrm{d}\varphi, - \int_{\varphi_2}^{\varphi_4} \mathscr{W}_2(\varphi)\mathrm{d}\varphi, \tag{3.2}$$

where

$$q_0 = \frac{1}{3\pi^2 HWL} \begin{bmatrix} 3H\left(2\pi LW + R^2\right)(\varphi_3 - \varphi_1) \\ +12HR(L+W)\left(\cos(\varphi_3) - \cos(\varphi_1)\right) \\ +R\sin(\varphi_1)\left(3HR\cos(\varphi_1) + 6\pi LW + R^2\right) \\ -R\sin(\varphi_3)\left(3HR\cos(\varphi_3) + 6\pi LW + R^2\right) \\ +R^2\cos(2\varphi_3)\left(R\sin(\varphi_3) - 3(L+W)\right) \\ -R^2\cos(2\varphi_1)\left(R\sin(\varphi_1) - 3(L+W)\right) \end{bmatrix}, \tag{3.3}$$

$$\mathscr{W}_1(\varphi) = \frac{2(H - R\cos(\varphi))}{\pi^2 HWL} \begin{bmatrix} 2W\sin(\varphi)\sqrt{R^2 - L^2\csc^2(\varphi)} - 2WR\sin(\varphi) \\ +2LW\arcsin\left(\frac{L\csc(\varphi)}{R}\right) - L^2 \end{bmatrix}, \tag{3.4}$$

and

$$\mathscr{W}_2(\varphi) = \frac{2(H - R\cos(\varphi))}{\pi^2 HWL} \begin{bmatrix} -2L\sin(\varphi)\sqrt{R^2 - W^2\csc^2(\varphi)} - 2WR\sin(\varphi) \\ +2LW\arccos\left(\frac{W\csc(\varphi)}{R}\right) + R^2\sin^2(\varphi) + W^2 \end{bmatrix}. \tag{3.5}$$

The angles are defined by

$$\varphi_1 = \arccos\left(\min\left\{\tfrac{H}{R}, 1\right\}\right), \tag{3.6}$$

$$\varphi_2 = \begin{cases} \arcsin\left(\min\left\{\tfrac{W}{R}, 1\right\}\right), & R < D_1, \\ \varphi_1, & \text{else}, \end{cases} \tag{3.7}$$

$$\varphi_3 = \begin{cases} \arcsin\left(\min\left\{\tfrac{L}{R}, 1\right\}\right), & R < D_2, \\ \varphi_1, & \text{else}, \end{cases} \tag{3.8}$$

and

$$\varphi_4 = \begin{cases} \arcsin\left(\min\left\{\tfrac{D_3}{R}, 1\right\}\right), & R < D_4, \\ \varphi_1, & \text{else}, \end{cases} \tag{3.9}$$

where

$$D_1 = \sqrt{H^2 + W^2}, \tag{3.10}$$

$$D_2 = \sqrt{H^2 + L^2}, \tag{3.11}$$

$$D_3 = \sqrt{W^2 + L^2}, \tag{3.12}$$

and

$$D_4 = \sqrt{H^2 + W^2 + L^2}. \tag{3.13}$$

When $R < W$, the last two terms in (3.2) *equal zero. Otherwise, the LOS probability can be approximated by a closed-form expression as*

$$\Pr_{\mathrm{LOS}}(R) \triangleq q_0 + \frac{1}{6}\left[\begin{array}{l} (\varphi_4 - \varphi_3)\left(\mathscr{W}_1(\varphi_3) + \mathscr{W}_1(\varphi_4) + 4\mathscr{W}_1\left(\dfrac{\varphi_3 + \varphi_4}{2}\right)\right) \\ -(\varphi_4 - \varphi_2)\left(\mathscr{W}_2(\varphi_2) + \mathscr{W}_2(\varphi_4) + 4\mathscr{W}_2\left(\dfrac{\varphi_2 + \varphi_4}{2}\right)\right) \end{array}\right]. \tag{3.14}$$

Proof: According to the system model, a Tx-Rx link is a LOS link if both ends, i.e., the BS and the UE, are in the same cuboid room. Therefore, deriving the LOS probability for a single room can be seen as deriving the probability that a line segment of length R drops in a cuboid with the dimension $H \times W \times L$ without crossing any face of the cuboid [128]. Let Θ, Φ and $\mathscr{V}$ represent the ranges of the angle φ, the angle θ and the length of projections (x,y,z) within which the link satisfies the necessary and sufficient condition as a LOS link. Therefore, the LOS probability in a typical room can be derived by the integration of the joint PDF, as

$$\mathrm{Pr}_{\mathrm{LOS}}(R) = \int_{\Phi}\int_{\Theta}\iiint_{\mathscr{V}} f(x,y,z,\varphi,\theta)\mathrm{d}x\mathrm{d}y\mathrm{d}z\mathrm{d}\theta\mathrm{d}\varphi, \tag{3.15}$$

where the intervals $\mathscr{V}$, Θ and Φ are given in

$$\begin{aligned}\mathscr{V} = \{(x,y,z)|\ &(R\cos(\theta)\sin(\varphi) < x < W) \wedge \\ &(R\sin(\theta)\sin(\varphi) < y < L) \wedge (R\cos(\varphi) < z < H)\},\end{aligned} \tag{3.16}$$

$$\Theta = \left\{\theta \middle| \arccos\left(\min\left\{\frac{W}{R\sin(\varphi)}, 1\right\}\right) < \theta < \arcsin\left(\min\left\{\frac{L}{R\sin(\varphi)}, 1\right\}\right)\right\}, \tag{3.17}$$

and

$$\Phi = \left\{\varphi \middle| \arccos\left(\min\left\{\frac{H}{R}, 1\right\}\right) < \varphi < \arcsin\left(\min\left\{\frac{\sqrt{W^2+L^2}}{R}, 1\right\}\right)\right\}, \tag{3.18}$$

respectively. The joint PDF $f(x,y,z,\varphi,\theta)$ given in (3.1) is first integrated with respect to (x,y,z), i.e.,

$$F(\varphi,\theta) = \iiint_{\mathscr{V}} f(x,y,z,\varphi,\theta)\mathrm{d}x\mathrm{d}y\mathrm{d}z, \tag{3.19}$$

while leaving θ and φ as variables. Based on the geometry relationship between the room and the Tx-Rx link, (3.15) can be reformulated as

$$\mathrm{Pr}_{\mathrm{LOS}}(R) = q_0 + q_1 - q_2, \tag{3.20}$$

where

$$q_0 = \int_{\varphi_1}^{\varphi_3} \int_0^{\frac{\pi}{2}} F(\varphi, \theta) \mathrm{d}\theta \mathrm{d}\varphi, \tag{3.21}$$

$$q_1 = \int_{\varphi_3}^{\varphi_4} \int_0^{\arcsin\left(\frac{L}{R\sin(\varphi)}\right)} F(\varphi, \theta) \mathrm{d}\theta \mathrm{d}\varphi, \tag{3.22}$$

and

$$q_2 = \int_{\varphi_2}^{\varphi_4} \int_0^{\arccos\left(\frac{W}{R\sin(\varphi)}\right)} F(\varphi, \theta) \mathrm{d}\theta \mathrm{d}\varphi, \tag{3.23}$$

and the angles are defined in (3.6)-(3.9). q_0 can be obtained straightforwardly as (3.3). Solving the integrals with respect to θ, q_1 and q_2 can be rewritten as

$$q_1 = \int_{\varphi_3}^{\varphi_4} \mathscr{W}_1(\varphi) \mathrm{d}\varphi, \tag{3.24}$$

and

$$q_2 = \int_{\varphi_2}^{\varphi_4} \mathscr{W}_2(\varphi) \mathrm{d}\varphi, \tag{3.25}$$

where $\mathscr{W}_1(\varphi)$ and $\mathscr{W}_2(\varphi)$ are given by (3.4) and (3.5), respectively. In order to facilitate the mathematical tractability of the 3-D LOS probability model, an approximation of (3.25) is made based on the Simpson's $1/3$ rule [129]. Instead of the integrand $\mathscr{W}_1(\varphi)$ or $\mathscr{W}_2(\varphi)$, a third-order Lagrange interpolating polynomial with the same values at three equally spaced points as the integrand is integrated with respect to φ over Φ. Then (3.14) can be obtained by inserting the approximation expressions of q_1 and q_2 into (3.2). ■

The numerical validation of Theorem 3.2 is performed by the Monte Carlo simulations. As shown in Fig. 3.2, the analytic results in (3.14) are in good agreements with the simulations performed for different dimensions of rooms. The dimensions of the rooms decide the trends of LOS probabilities varying with link length. Not only the volume but the ratio among the height, width, and length affect the LOS probability in a room.

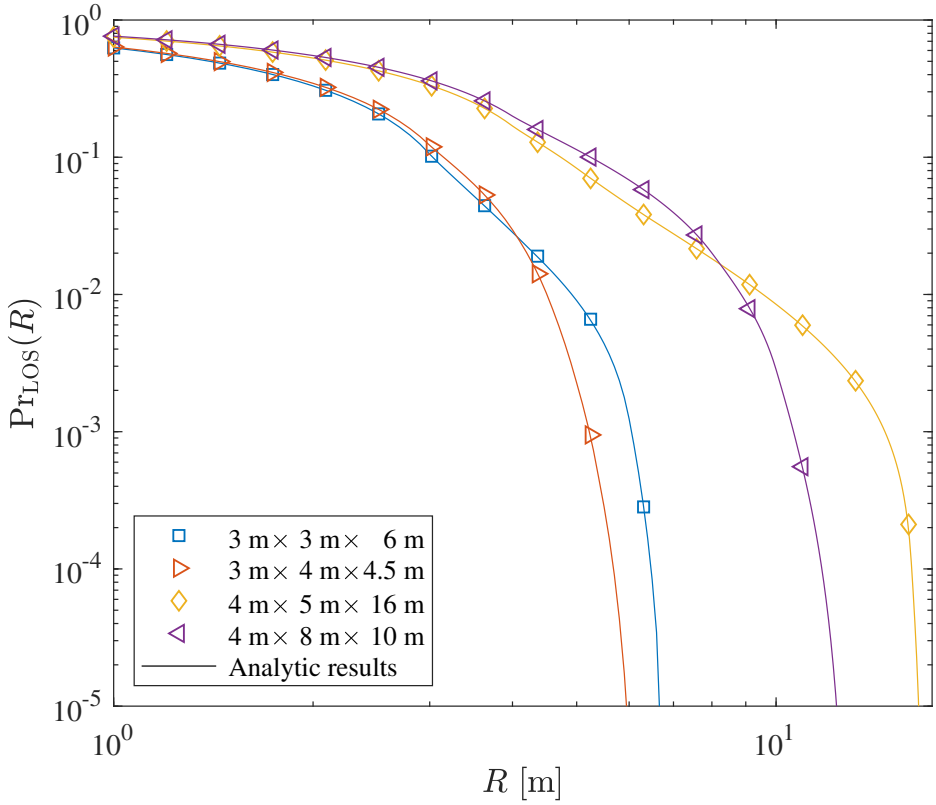

Fig. 3.2 LOS probability in single rooms varies with link length. Analytic results and Monte Carlo simulations in different types of single rooms. The results generated by simulations are denoted by the markers.

3.2.3 3-D LOS probability in a multi-storey building

In this subsection, the 3-D LOS probability in a multi-storey building is given. The volume for the t-th room in a building is represented by V_t, then the total volume for a building consisting of N_{B} rooms is given by

$$V_{\mathrm{B}} = \sum_{t=1}^{N_{\mathrm{B}}} V_t. \tag{3.26}$$

Since the UE is uniformly deployed in a building, the probability for the UE located in the t-th room is

$$p_t = \frac{V_t}{V_{\mathrm{B}}}. \tag{3.27}$$

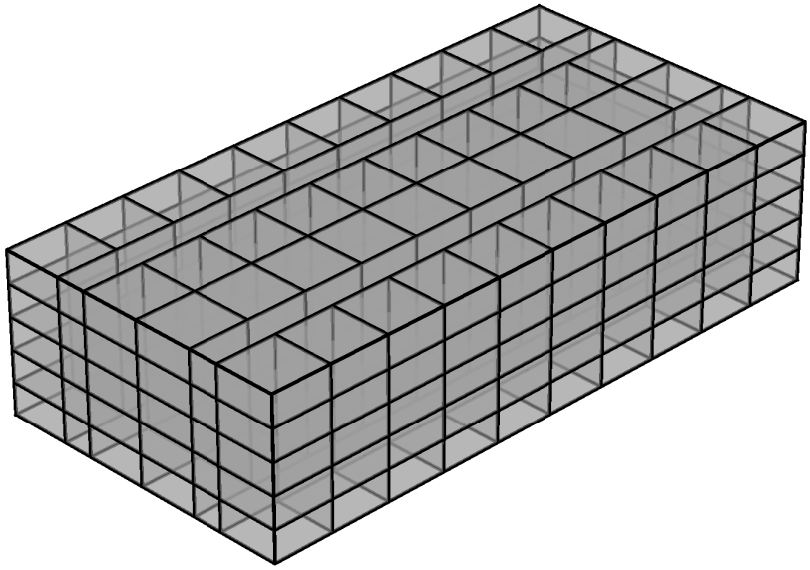

Fig. 3.3 A 5-storey building with a WINNER II A1 layout.

Lemma 3.1. *The LOS probability for a Tx-Rx link with the length R in a building with* N_{B} *rooms can be denoted by*

$$\Pr_{\mathrm{B}}(R) = \sum_{t=1}^{N_{\mathrm{B}}} p_t \Pr_{t,\mathrm{LOS}}(R), \tag{3.28}$$

where $N_{\mathrm{B}} \in \mathbb{N}_1$, p_t *is the probability that the UE end of this link is located in the* t*-th room of the building and* $\Pr_{t,\mathrm{LOS}}(R)$ *denotes the LOS probability in the* t*-th room.*

Proof: Define C_t as the scenario that the UE end of a Tx-Rx link is located in the t-th room and S as the scenario where the link is a LOS link. Then the overall LOS probability in a building can be computed by summing up the conditional LOS probabilities given that C_t happens and weighted by p_t, as

$$\Pr_{\mathrm{B}}(R) = \sum_{t=1}^{N_{\mathrm{B}}} p_t \Pr\left[S|C_t\right]. \tag{3.29}$$

The conditional probability can be derived by Theorem 3.2, and then (3.28) can be solved. ■

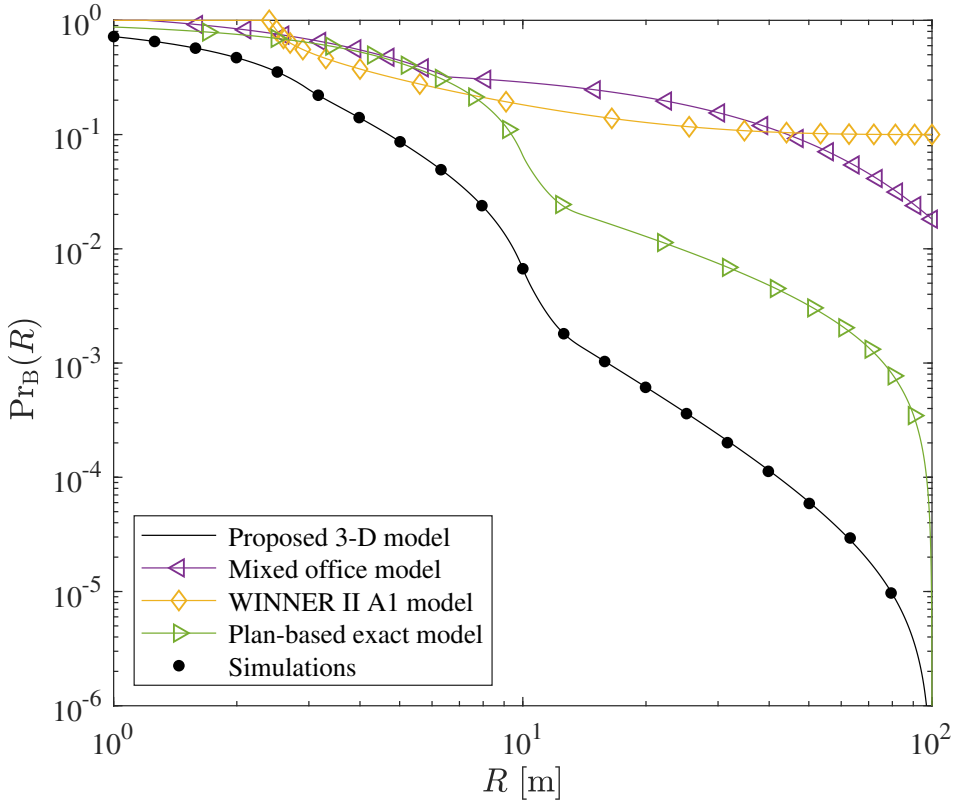

Fig. 3.4 LOS probability in a building varies with link length. Analytic results and simulations in a typical office building shown in Fig. 3.3.

The LOS probability given by (3.28) is validated next in a typical office building. Fig. 3.3 shows a building geometry where each storey of this 5-storey building consists of 40 rooms with dimensions 10 m$\times$10 m$\times$3 m and two corridors with dimensions 100 m$\times$5 m$\times$3 m, as described by the WINNER II A1 scenario [32]. The Monte Carlo simulations are conducted for Tx-Rx links with lengths ranging from 1 to 100 m. For each link length, 2×10^4 UE ends are randomly generated in the building, and then the BS ends are generated in random directions. The LOS probability is the mean value of the results of 10^3 simulation realisations. Two commonly used 2-D empirical LOS probability models, the mixed office model in [102, Table 7.4.2-1] and the WINNER II A1 model in [32, Table 4-7], which are referred to as the mixed office model and the WINNER II A1 model, respectively, in the following, and the 2-D plan-based exact LOS probability model in [105], which is referred to as the plan-based exact model in the following, are also employed to predict the LOS probability in this scenario as the benchmarks. As can be seen in Fig. 3.4, the proposed 3-D model fits the simulations well. The trend of the curve computed by the proposed 3-D model changes significantly around

the point $R = 10$ m. It is due to the fact that the 40 rooms in the building are with 10 m width and length.

The 2-D empirical models show poor agreements with the simulations since the specific layout of the building is not included. The 2-D plan-based exact model is implemented by inserting the dimensions of the 2-D floor plan of the WINNER II A1 scenario. Despite the similar trend to the simulations, this model overestimates the LOS probability due to the missing direction information in 3-D space. The 2-D models only address the probability of intersections on the horizontal direction but ignore the probability that the Tx-Rx link is obstructed by the two faces parallel to the XY-plane. Therefore, the proposed 3-D model can obtain the LOS probability accurately for a practical building, while the 2-D models lose accuracy when directly applied in a 3-D scenario.

3.3 Network Performance Evaluation Based on 3-D LOS Probability Model

3.3.1 Network model

A one-tier downlink dense homogeneous network is studied in a typical office building, as shown in Fig. 3.3. The locations of BSs are assumed following a 3-D homogeneous PPP with density λ_{B} [BSs·km^{-3}] in an infinite 3-D Euclidean space $\mathbb{R}^3$. The path gain over a link length R is expressed as $R^{-n_{\mathrm{L}}}$ and $R^{-n_{\mathrm{N}}}$ for the LOS link and the NLOS link, where n_{L} and n_{N} are the PLEs for LOS and NLOS scenarios, respectively. The PLEs n_{L} and n_{N} include the impacts of the structural materials and should be adjusted according to the propagation environment. The BSs are assumed to operate in the same frequency band with the same transmit power. UE is randomly located in the building. UE is associated with the BS providing the strongest signal, while signals received from the other BSs are considered as interference. The effects of the small-scale fading and the thermal noise are ignored in this interference-limited network.

3.3.2 Coverage probability in a building

Based on the network model above, the 3-D LOS probability model is further applied in the network performance evaluation in terms of the coverage probability. In the computations, the PLEs $n_{\mathrm{L}} = 1.73$ and $n_{\mathrm{N}} = 3.19$ [102], and the density of BSs $\lambda_{\mathrm{B}} = 10^6$ BSs·km^{-3} in an

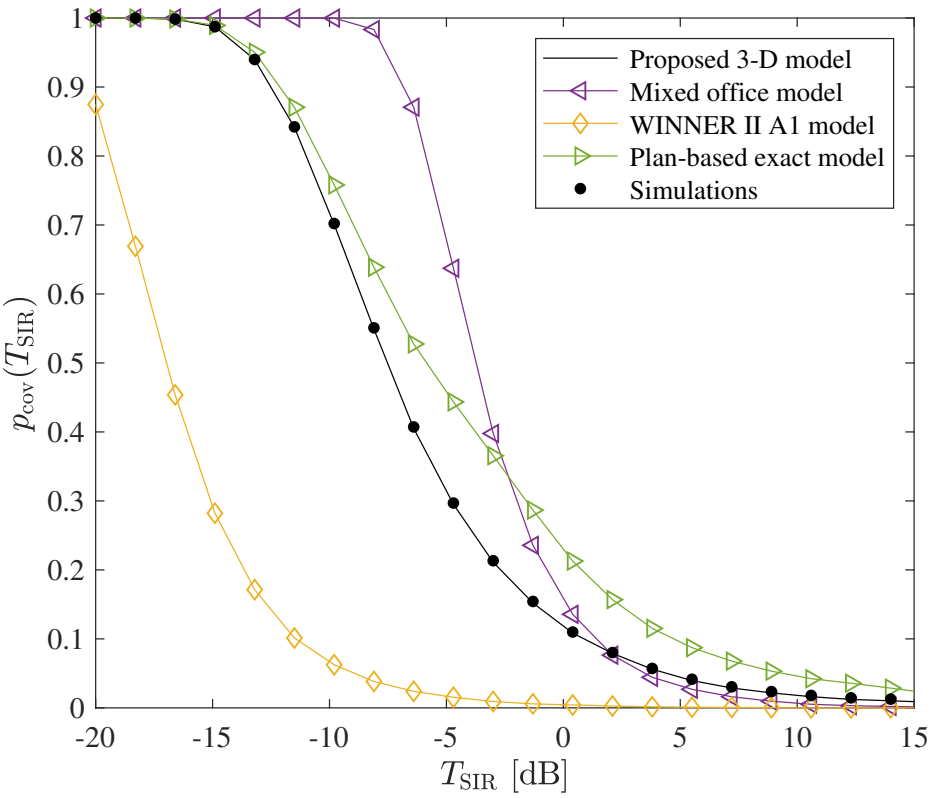

Fig. 3.5 Coverage probability in a typical office building shown in Fig. 3.3.

UDS network [98, 124, 130]. Defining T_{SIR} as the SIR threshold, the coverage probability

$$p_{\mathrm{cov}}(T_{\mathrm{SIR}}) = \Pr\{\mathrm{SIR} > T_{\mathrm{SIR}}\}. \tag{3.30}$$

For both the model-based and Monte Carlo simulations, the simulations are conducted 2×10^4 realisations to observe the coverage probability. In the model-based simulations, LOS and NLOS scenarios are distinguished based on the probability computed using LOS probability models. In the Monte Carlo simulations, LOS and NLOS scenarios are distinguished according to if any wall intersects the Tx-Rx link.

As shown in Fig. 3.5, the proposed model matches the Monte Carlo simulations well. For the benchmarks, the coverage probability obtained based on the 2-D empirical models shows poor agreements with the simulations. Although the 2-D plan-based exact model may describe the trend of the coverage probability p_{cov} as T_{SIR} increases, it overestimates the coverage probability significantly in this 3-D environment under the parameters assumed. The 2-D models ignore the cross-floor associations/interference, thereby leading to the under-

or overestimated network performance. Therefore, the proposed 3-D LOS probability model is critical for the network performance evaluation in practical buildings.

3.4 Summary

In this chapter, a LOS probability model is proposed for 3-D indoor environments. According to the exact dimensions of a practical building, both the LOS probability and the coverage probability can be obtained based on the proposed closed-form model accurately. Considering the trend of indoor network densification, the proposed 3-D LOS probability model can be employed to address the indoor blockage effects for practical buildings in network performance evaluation and optimisation.

Chapter 4

Partition-Based Analytic Evaluation of Building Wireless Performance

Overview

The significant dependence between indoor wireless network performance and the building structures can be considered as an intrinsic property of a building, which means that the building has to be designed to achieve desirable indoor wireless network performance. To quantify the impact of building structures on indoor wireless networks, the concept of BWP has been brought up and two FoMs, i.e., the PG and the IG, have been designed to assess the BWP. In previous works, the analytical models of the PG and the IG were derived for single rooms, which means only the impact of the geometry of a single room was considered. In this chapter, a tractable approach is proposed to obtain the BWP with a partition-based path gain model. It enables the BWP FoMs to capture the impact of both building materials and layouts on a 2-D plane.

4.1 Introduction

4.1.1 Background

As over 80% of indoor traffic takes place indoors, high-capacity and energy-efficient wireless networks are required in buildings. However, indoor network evaluation and optimisation remain a nodus due to complex building structures. The blockage effects caused by indoor obstacles, on the one hand, isolate users from undesired interference, but on the other hand, attenuate the intended signals significantly [17]. Consequently, in a building in use, the efforts, such as increasing the transmit power or the number of small cells, may enhance the

interference and lead to low energy efficiency rather than improving the network performance. The significant dependence between indoor wireless network performance and the building structures can be considered an intrinsic property of a building, which means the building has to be designed to achieve desirable indoor network performance. Inspired by this property, the concept of BWP has been brought up in the prior works [19–22].

The objective of this chapter is to complement the initial works in [19–22] by generating a partition-based BWP evaluation scheme under a more comprehensive system model. The initial works only investigated the impact of the geometry of a single room on indoor wireless network performance. In this chapter, the effects of both building materials and layouts are further addressed in the framework of the BWP evaluation.

4.1.2 Prior works and motivations

In previous studies investigating indoor network performance, the building structures have been modelled with different assumptions to enable mathematical tractability. In [113–115], the Boolean scheme assumption proposed in [13] has been applied to model the walls in a building, where the walls have been assumed as line segments with PPP distributed centres, uniformly distributed length, and random orientations. To better approximate practical building layouts, the Boolean scheme assumption has been modified in [17, 114, 115], where the walls have been assumed binary oriented. In [114, 123], the MPLP has also been employed to model the walls by a grid. These assumptions have introduced stochastic geometry tools in indoor wireless network evaluation. Numerical results in the literature have shown that the values of system-wide indoor network performance metrics, e.g., the coverage rate and the ASE, vary with the building structure parameters, e.g., the blockage density and the average wall attenuation factor. Nevertheless, as these assumptions cannot correspond to practical buildings, only general relationships between the building structures and the network performance have been discussed.

Conventionally, when focusing on a given building, the ray-based deterministic approaches, such as the RT and RL techniques, are employed to predict indoor network performance following the GO rules [131]. However, these deterministic approaches only apply to an existing building employing a specific network solution with predefined network architectures and the corresponding practical deployment and configurations. If assessing the indoor wireless network performance by the deterministic approaches at the building design stage to circumvent the constraints imposed by the building structures, all the possible combinations of wireless network solutions and building designs have to be simulated. Consequently, it is not feasible due to enormous computational cost and time consumption.

To quantify the wireless friendliness of a given building under design, a framework of the BWP evaluation has been built up in previous works [19–22]. The framework has captured the intrinsic BWP by quantifying the effective change of the maximum achievable performance gain from open space to indoors without a specified wireless network solution. To this end, a general and idealistic network model has been employed in [19–22], which follows the assumptions summarised in Section 2.2.3. Nevertheless, following these assumptions, the Tx-Rx links are only distinguished into LOS and NLOS scenarios. For a probing UE, the NLOS signals over the same link length are with the same strength no matter how many obstacles intersect the links, which means that the rooms in a building are considered independent from each other in terms of the BWP. Consequently, the building structures impacting indoor wireless performance have been restricted to the geometry of the room where the probing UE is located.

In practice, the layout of a building decides the number of obstacles intersecting a NLOS Tx-Rx link. Measurements conducted for indoor scenarios have indicated that the penetration loss varies with the thickness and EM properties of building materials [23, 132]. Therefore, a more practical BWP evaluation scheme is desired to address the impact of building materials and layouts on indoor wireless network performance.

4.1.3 Contributions in this chapter

Compared with the prior works reported in [19–22], this chapter improves the BWP evaluation scheme by introducing the site-specific information into the system model. Instead of only distinguishing the LOS and NLOS links, a partition-based path gain model is employed to account for the exact penetration loss for each Tx-Rx link.

To facilitate mathematical tractability, a given building under design consisting of polygonal-shaped rooms is first divided into multiple computation units. Then the analytical models to compute the PG and the IG are given in closed-form expressions and validated by the Monte Carlo simulations. It also demonstrates the partition-based BWP evaluation of a typical office building using the proposed method. The numerical results are generated with different carrier frequencies and wall attenuation factors to observe the variation of the BWP with network configurations and building materials. The effects of the layout on the BWP are compared among uniformly distributed UE locations in the building.

The proposed partition-based BWP evaluation scheme enables the BWP FoMs to capture the impact of building materials and layouts on indoor wireless network performance. It assesses the BWP in various probing UE locations across a building computational-efficiently, which can be employed in future wireless-friendly building design.

4.2 System Model

4.2.1 Definition of the BWP FoMs

This section recalls the definitions of the BWP FoMs given in [19–22]. The BWP FoMs, i.e., the PG and the IG, are defined by comparing the SINR in a probing UE location in the in-building scenario and the benchmark, i.e., the open-space scenario. The open-space scenario refers to that both the probing UE and transmit elements are located in ideal open space, where all the Tx-Rx links are LOS links. The in-building scenario refers to that the probing UE is located in a given building, where the indoor obstacles could attenuate the signals. The SINR in the open-space scenario is denoted by

$$\gamma_{\mathrm{O}} = \frac{P_{\mathrm{O}}}{I_{\mathrm{O}} + \sigma^2}, \tag{4.1}$$

and the SINR in the in-building scenario is denoted by

$$\gamma_{\mathrm{B}} = \frac{P_{\mathrm{B}}}{I_{\mathrm{B}} + \sigma^2}, \tag{4.2}$$

where P_{O} and P_{B} denote the total received intended signal power in the open-space scenario and the in-building scenario, respectively, I_{O} and I_{B} denote the total received interference power in the open-space scenario and the in-building scenario, respectively, and σ^2 represents the thermal noise power. The subscripts "O" and "B" denote the open-space and the in-building scenarios throughout this chapter, respectively.

The BWP FoMs capture the wireless network performance gain resulted from placing a building with specific structures in open space. The PG and the IG are defined as

$$g_{\mathrm{P}} \triangleq \frac{P_{\mathrm{B}}}{P_{\mathrm{O}}}, \tag{4.3}$$

and

$$g_{\mathrm{I}} \triangleq \frac{I_{\mathrm{O}} + \sigma^2}{I_{\mathrm{B}} + \sigma^2}, \tag{4.4}$$

which indicate the effective change of the desired and undesired power received by a probing UE due to the presence of a building, respectively. Higher g_{P} means that less intended signal power is degraded by the building structures and higher g_{I} means that more interference power is blocked by the building structures. According to the definitions of g_{P} and g_{I}, there

is the relationship

$$\gamma_{\mathrm{B}} = g_{\mathrm{P}} g_{\mathrm{I}} \gamma_{\mathrm{O}}, \tag{4.5}$$

between $g_{\mathrm{P}} g_{\mathrm{I}}$ and the SINRs in a probing UE location in a given building and open space. Then $g_{\mathrm{P}} g_{\mathrm{I}}$ represents the effective change of the SINR in a probing UE location from open space to a given building. With the definitions of the FoMs, designing a building accommodating to a well-performed and energy-efficient indoor wireless network can be conducted by adjusting the building structures to achieve good BWP with high PG and IG values.

4.2.2 Assumptions

This chapter focuses on downlink transmissions. To capture the intrinsic BWP, the impact of building structures should be considered independent from any specific wireless technique or network deployment. Here a general and idealistic network model is employed to present the maximum achievable performance gain in a given building. The assumptions of the network model are as follows, where Assumptions 4.1 and 4.2 are from [19–22] and have been explained in section 2.2.3.

Assumption 4.1. *The transmit elements with the same transmit power are uniformly and infinitely densely distributed on a plane surface. All the transmit elements operate continuously with full power at the same frequency band. For the assumed network, the transmitted power per unit area is defined as* P_{T} $[\mathrm{Wm}^{-2}]$. *Given a small area* $\mathrm{d}\Omega$*, the transmitted power from which is denoted by* $P_{\mathrm{T}}\mathrm{d}\Omega$.

Assumption 4.2. *The probing UE makes use of all detectable power. A threshold* P_{th} $[\mathrm{Wm}^{-2}]$ *is defined according to the sensitivity of the receive device. The received power is detectable and considered intended signal power when exceeding* P_{th}*. Otherwise, it is considered interference power.*

Assumption 4.3. *A bounded partition-based path gain model is employed, which includes the distance-dependent decay and the penetration loss. The penetration loss on a signal refers to the attenuation caused by walls in a building.*

The small-scale fading is negligible in both the open-space and in-building scenarios for the assumed significantly densified network [133, 134]. For the sake of simplicity, the transmit elements and the probing UE are assumed on a 2-D plane.

4.2.3 Bounded path gain model

To include the site-specific information into the BWP evaluation scheme, a partition-based path gain model is employed [37]. Define i as the number of walls intersecting a Tx-Rx link. Consequently, a Tx-Rx link is a LOS link if $i = 0$ or a NLOS link if $i > 0$. The total penetration loss on a typical NLOS link is computed by

$$\prod_{l=1}^{i} A_l, \tag{4.6}$$

where A_l represents the attenuation factor of the l-th wall, which is decided by its thickness and the EM properties of the material. For the sake of simplicity, the walls in a building are assumed with the same attenuation factor A and denoted by the line segments without thickness. Then A^i represents the total penetration loss on a Tx-Rx link intersected by i walls, where $A \in (0,1]$ and $i \in \mathbb{N}_0$. In the literature, the wall attenuation factor is usually denoted in decibel as $A_{\mathrm{dB}} = -10\log_{10}(A)$.

For a typical Tx-Rx link with length R [m], the path gain is computed by

$$G(R,i) = \min\left\{1, A^i \left(\frac{\lambda}{4\pi}\right)^2 R^{-n}\right\}, \tag{4.7}$$

where the PLE n is decided by the characterisations of the propagation environment [135–138]. The wavelength $\lambda = \frac{c}{f_{\mathrm{c}}}$, where f_{c} [Hz] is the carrier frequency and $c = 3 \times 10^8$ ms^{-1} denoting the speed of light. Following the energy conservation law, the path gain should not exceed 1, and the approaches proposed in this chapter are applicable for arbitrary $n > 2$.

Following Assumption 4.2, the intended signal power to a probing UE satisfies

$$P_{\mathrm{T}} G(R,i) > P_{\mathrm{th}}. \tag{4.8}$$

Solving $P_{\mathrm{T}} G(R,i) = P_{\mathrm{th}}$, there is that

$$R_i = \left(\frac{A^i P_{\mathrm{T}}}{P_{\mathrm{th}}}\right)^{\frac{1}{n}} \left(\frac{\lambda}{4\pi}\right)^{\frac{2}{n}}. \tag{4.9}$$

Then a transmit element is considered an intended signal source to the probing UE when the Tx-Rx link intersected by i walls with length R satisfies $R < R_i$. Otherwise, it is considered an interference source. For the open-space scenario, the intended signal sources are located inside a circle with a radius of R_0 centred on the probing UE. As shown in Fig. 4.1, for the in-building scenario, the intended signal sources are located inside the arcs with radiuses R_i.

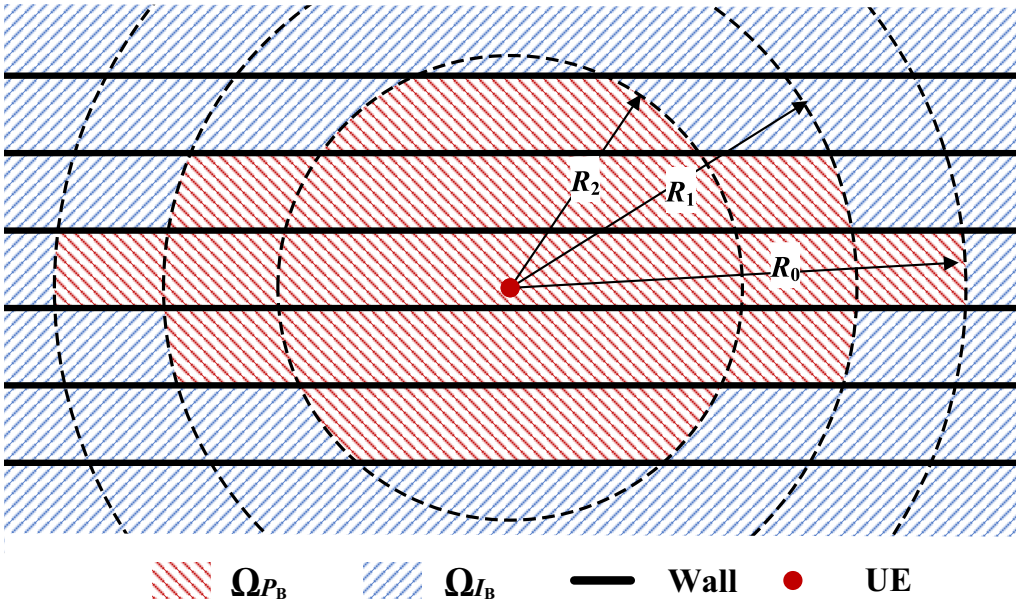

Fig. 4.1 The plan of a storey consisting of long corridors. For the probing UE, the areas that contain the transmit elements providing intended signals and interference signals are denoted by Ω_{P_B} and Ω_{I_B}, respectively.

4.3 Analytic Computations

4.3.1 Closed-form P_O and I_O

In open space, all signals from the transmit elements reach a target UE through LOS links, i.e., $i = 0$. Using a polar coordinate system (R, θ), whose pole is located on the probing UE, the total received intended signal power is given by

$$P_O = \int_0^{2\pi} \int_0^{R_0} P_T G(R, i) \mathrm{d}\Omega, \tag{4.10}$$

and the total received interference power is given by

$$I_O = \int_0^{2\pi} \int_{R_0}^{+\infty} P_T G(R, i) \mathrm{d}\Omega, \tag{4.11}$$

where R_0 is the minimum link length of an interference signal in open space. The closed-form expressions of P_O and I_O are given in Theorem 4.1.

Theorem 4.1. *The intended signal power and the interference power received by a probing UE in open space are computed by*

$$P_{\mathrm{O}} = P_{\mathrm{T}} \frac{2\pi}{2-n} \left(\frac{\lambda}{4\pi}\right)^{\frac{4}{n}} \left[\left(\frac{P_{\mathrm{T}}}{P_{\mathrm{th}}}\right)^{\frac{2}{n}-1} - \frac{n}{2} \right], \tag{4.12}$$

and

$$I_{\mathrm{O}} = -P_{\mathrm{T}} \frac{2\pi}{2-n} \left(\frac{\lambda}{4\pi}\right)^{\frac{4}{n}} \left(\frac{P_{\mathrm{T}}}{P_{\mathrm{th}}}\right)^{\frac{2}{n}-1}. \tag{4.13}$$

Proof: The derivations of (4.12) and (4.13) are straightforward by inserting (4.7) into (4.10) and (4.11), respectively, where R_0 is computed by inserting $i = 0$ into (4.9). ■

4.3.2 Division of computation units

To obtain P_{B} and I_{B} in a given building analytically, the plan of a building is first divided into multiple computation units and compute the intended signal power and the interference power from each. For example, Fig. 4.2 shows the division of computation units for a sample building about UE 1. For the in-building scenario, the subscripts "L", "F", and "U" denote the scenarios that the transmit elements are LOS, indoor NLOS, and outdoor NLOS transmit elements, respectively. Computation units containing LOS transmit elements are referred to as the LOS computation units and denoted by Ω_{L}. Computation units containing NLOS transmit elements inside and outside the building are referred to as the indoor NLOS computation units and the outdoor NLOS computation units, which are denoted by Ω_{F} and Ω_{U}, respectively. The signals sent from a computation unit traverse the same walls to the probing UE.

A polar coordinate system (R, θ) is built for each computation unit, where the pole is located on the probing UE and θ is limited to the interval $\left[0, \frac{\pi}{2}\right)$ for simplicity. The computation units and the parameters are defined as follows:

- As shown in Fig. 4.3a, a typical LOS computation unit, i.e., Ω_{L}, is a triangle composed of a wall segment and two line segments from the probing UE to the wall segment's endpoints. The reference 0-angle is defined on the line perpendicular to the wall. The angles at the endpoints of the wall segment are defined as θ_{e} and θ_{E}, where $0 \leq \theta_{\mathrm{e}} < \theta_{\mathrm{E}} < \frac{\pi}{2}$. The distance from the probing UE to the wall is denoted by D_0.

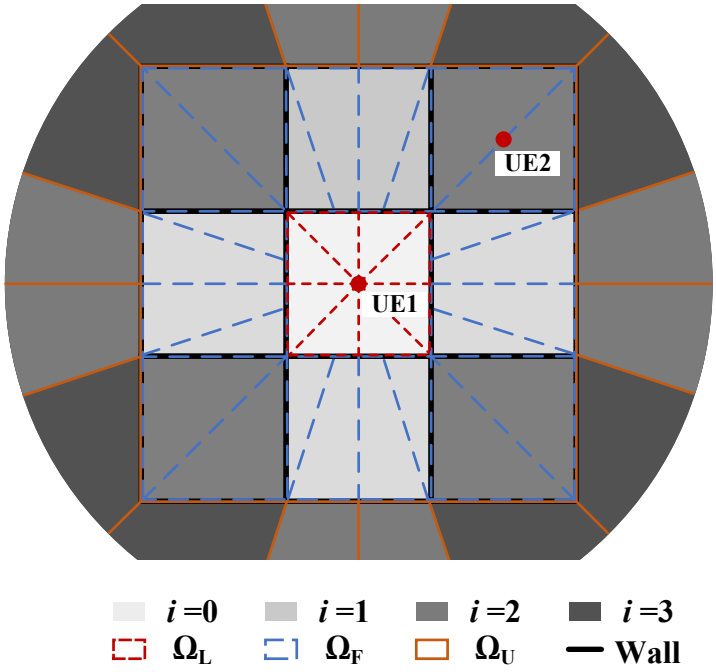

Fig. 4.2 Computation unit division in a sample building about UE 1. The LOS computation units, indoor NLOS computation units, and outdoor NLOS computation units are denoted by Ω_{L}, Ω_{F}, and Ω_{U}, respectively. UE 1 and UE 2 are located in the centres of the rooms in the centre and a corner of the sample building, respectively.

- As shown in Fig. 4.3c-d, a typical indoor NLOS computation unit, i.e., Ω_{F}, is a triangle/quadrilateral composed of two wall segments and one/two line segments connecting the endpoints. The reference 0-angle is defined on the line perpendicular to the wall traversed by signals sent from Ω_{F}. The angles at the endpoints of the wall segments are defined as θ_{e} and θ_{E}, where $0 \leq \theta_{\mathrm{e}} < \theta_{\mathrm{E}} < \frac{\pi}{2}$. The angle between the two walls is denoted by θ_{b}. Define the angles

$$\theta'_{\mathrm{e}} = \min\{|\theta_{\mathrm{e}} - \theta_{\mathrm{b}}|, |\theta_{\mathrm{E}} - \theta_{\mathrm{b}}|\}, \tag{4.14}$$

and

$$\theta'_{\mathrm{E}} = \max\{|\theta_{\mathrm{e}} - \theta_{\mathrm{b}}|, |\theta_{\mathrm{E}} - \theta_{\mathrm{b}}|\}, \tag{4.15}$$

where $0 \leq \theta'_{\mathrm{e}} < \theta'_{\mathrm{E}} < \frac{\pi}{2}$. The operators $\min\{\cdot\}$ and $\max\{\cdot\}$ denote the minimum and maximum values of the arguments, respectively. The distance from the probing UE

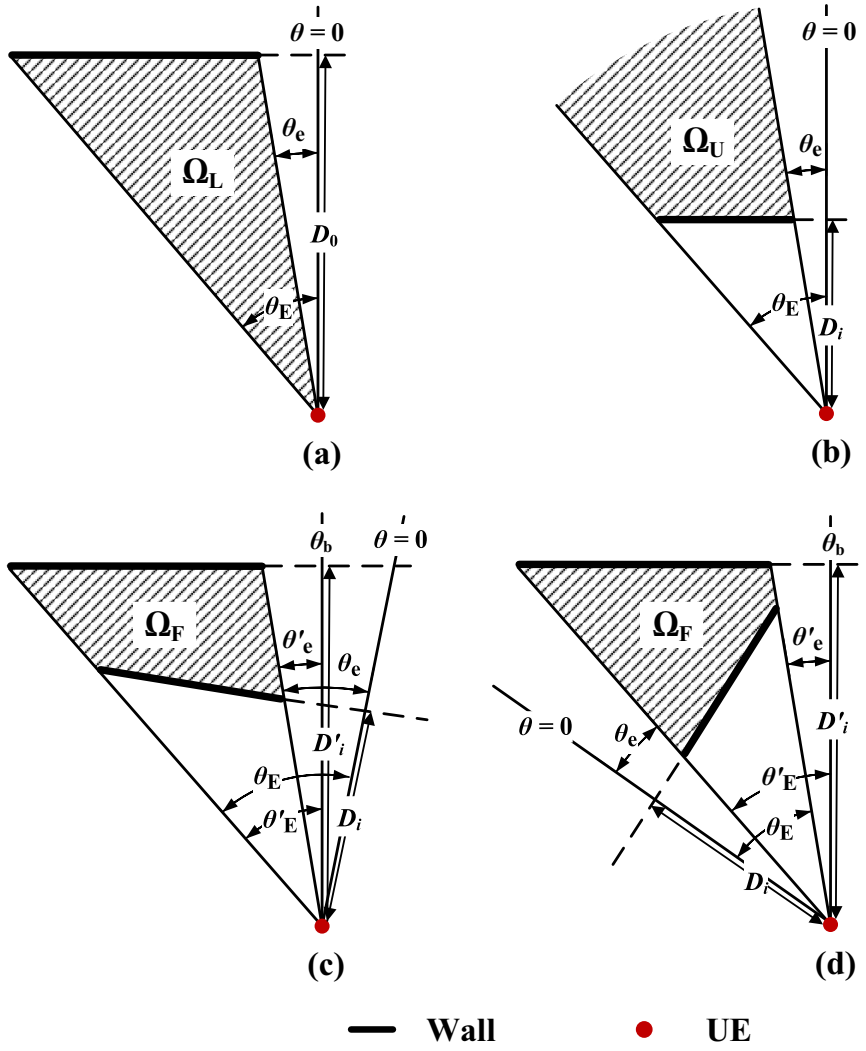

Fig. 4.3 The typical computation units. (a) A typical LOS computation unit Ω_{L}. (b) A typical outdoor NLOS computation unit Ω_{U}. (c), (d) Typical indoor NLOS computation units Ω_{F} .

to the wall traversed by signals sent from Ω_{F} is denoted by D_i, and to the wall not traversed is denoted by D'_i.

- As shown in Fig. 4.3b, a typical outdoor NLOS computation unit, i.e., Ω_{U}, is an infinite and continuous area confined by an external wall segment and two rays from the probing UE through the wall segment's endpoints. The reference 0-angle is defined on the line perpendicular to the external wall. The angles at the endpoints of the segment are defined as θ_{e} and θ_{E}, where $0 \leq \theta_{\mathrm{e}} < \theta_{\mathrm{E}} < \frac{\pi}{2}$. The distance from the probing UE to the external wall is denoted by D_i.

4.3.3 Closed-form P_{B} and I_{B}

For a probing UE in a given building, the total received intended signal power P_{B} can be denoted by

$$\begin{aligned} P_{\mathrm{B}} = & \sum_{i=1}^{i_{\max}-1} \sum_{m_{\mathrm{F},i}=1}^{M_{\mathrm{F},i}} \int_{\Omega_{P_{\mathrm{F}},m_{\mathrm{F},i}}} P_{\mathrm{T}} G(R,i) \mathrm{d}\Omega \\ & + \sum_{i=1}^{i_{\max}} \sum_{m_{\mathrm{U},i}=1}^{M_{\mathrm{U},i}} \int_{\Omega_{P_{\mathrm{U}},m_{\mathrm{U},i}}} P_{\mathrm{T}} G(R,i) \mathrm{d}\Omega \\ & + \sum_{m_{\mathrm{L},0}=1}^{M_{\mathrm{L},0}} \int_{\Omega_{P_{\mathrm{L}},m_{\mathrm{L},0}}} P_{\mathrm{T}} G(R,0) \mathrm{d}\Omega, \end{aligned} \tag{4.16}$$

and the total received interference power I_{B} can be denoted by

$$\begin{aligned} I_{\mathrm{B}} = & \sum_{i=1}^{i_{\max}-1} \sum_{m_{\mathrm{F},i}=1}^{M_{\mathrm{F},i}} \int_{\Omega_{I_{\mathrm{F}},m_{\mathrm{F},i}}} P_{\mathrm{T}} G(R,i) \mathrm{d}\Omega \\ & + \sum_{i=1}^{i_{\max}} \sum_{m_{\mathrm{U},i}=1}^{M_{\mathrm{U},i}} \int_{\Omega_{I_{\mathrm{U}},m_{\mathrm{U},i}}} P_{\mathrm{T}} G(R,i) \mathrm{d}\Omega \\ & + \sum_{m_{\mathrm{L},0}=1}^{M_{\mathrm{L},0}} \int_{\Omega_{I_{\mathrm{L}},m_{\mathrm{L},0}}} P_{\mathrm{T}} G(R,0) \mathrm{d}\Omega \end{aligned} \tag{4.17}$$

where $i_{\max}$ denotes the maximum number of walls intersecting the Tx-Rx links in the in-building scenario. In the given building, the number of LOS computation units is denoted by $M_{\mathrm{L},0}$, while the number of indoor and outdoor NLOS computation units that send signals intersecting i walls to reach the probing UE are denoted by $M_{\mathrm{F},i}$ and $M_{\mathrm{U},i}$, respectively. The area containing intended signal sources and interference sources in a computation unit are denoted by $\Omega_{P_{S,m_{S,i}}}$ and $\Omega_{I_{S,m_{S,i}}}$, respectively, where $S \in \{\mathrm{L},\mathrm{F},\mathrm{U}\}$. The analytical models to compute the intended signal power and the interference power from a typical computation unit are given as follows.

Theorem 4.2. *The intended signal power and the interference power from a typical LOS computation unit Ω_{L} can be computed by*

$$P_{\mathrm{L}} = \frac{1}{2} P_{\mathrm{T}} r_0^2 (\theta_{\mathrm{E}} - \theta_{\mathrm{e}}) + P_{\mathrm{T}} \left(\frac{\lambda}{4\pi}\right)^2 \left[\begin{array}{l} Z_1(\theta_{\mathrm{e}}, \theta_0, r_0, D_0, n-1) \\ + Z_0(\theta_0, \theta_{\mathrm{E}}, r_0, R_0, n-1) \end{array} \right], \tag{4.18}$$

and

$$I_{\mathrm{L}} = P_{\mathrm{T}} \left(\frac{\lambda}{4\pi} \right)^2 Z_1 \left(\theta_0, \theta_{\mathrm{E}}, R_0, D_0, n-1 \right), \tag{4.19}$$

respectively, where

$$\theta_0 = \mathrm{median} \left\{ \theta_{\mathrm{e}}, \theta_{\mathrm{E}}, \arccos \left(\frac{D_0}{\max \{D_0, R_0\}} \right) \right\}, \tag{4.20}$$

and

$$r_0 = \left(\frac{\lambda}{4\pi} \right)^{\frac{2}{n}}. \tag{4.21}$$

The parameters θ_{e}, θ_{E} and D_0 are defined in Section 4.3.2 for Ω_{L}. The radius R_0 is given by inserting $i = 0$ into (4.9). The operators $\min\{\cdot\}$, $\mathrm{median}\{\cdot\}$, *and* $\max\{\cdot\}$ *denote the minimum, median, and maximum values of the arguments, respectively. Note the analytical models proposed in this chapter apply to the cases that $r_0 < D_0$. For $0 \le z_1 < z_2 < \frac{\pi}{2}$, $z_3 > 0$, $z_4 > 0$, and $z_5 \ge 0$, $Z_1(\cdot)$ and $Z_0(\cdot)$ are in closed-form expressions, as*

$$Z_1 \left(z_1, z_2, z_3, z_4, z_5 \right) = \begin{cases} z_3 (z_1 - z_2) + z_4 \ln \left(\frac{\tan(z_2) + \sec(z_2)}{\tan(z_1) + \sec(z_1)} \right), & z_5 = 0, \\ \frac{1}{2} \mathrm{Im} \left\{ \mathrm{Li}_2(-e^{2jz_2}) - \mathrm{Li}_2(-e^{2jz_1}) \right\} + (z_2 - z_1) \ln \left(\frac{2z_4}{z_3} \right), & z_5 = 1, \\ \left\{ \begin{array}{l} \frac{z_3^{1-z_5}}{1-z_5} (z_1 - z_2) + \frac{z_4^{1-z_5}}{z_5(1-z_5)} \\ \times \left\{ \begin{array}{l} \cos^{z_5}(z_1) {}_2F_1 \left(\frac{z_5}{2}, \frac{1}{2}; \frac{z_5}{2} + 1; \cos^2(z_1) \right) \\ -\cos^{z_5}(z_2) {}_2F_1 \left(\frac{z_5}{2}, \frac{1}{2}; \frac{z_5}{2} + 1; \cos^2(z_2) \right) \end{array} \right. \end{array} \right., & \text{else}, \end{cases} \tag{4.22}$$

and

$$Z_0 \left(z_1, z_2, z_3, z_4, z_5 \right) = \begin{cases} (z_2 - z_1) \ln \left(\frac{z_4}{z_3} \right), & z_5 = 1, \\ \frac{(z_2 - z_1) \left(z_4^{1-z_5} - z_3^{1-z_5} \right)}{1 - z_5}, & z_5 \ne 1, \end{cases} \tag{4.23}$$

respectively, where ${}_2F_1(\cdot)$ denotes the hypergeometric function of the second kind, $\mathrm{Li}_s(z)$ *is the polylogarithm function, and* $\mathrm{Im}\{\cdot\}$ *denotes the imaginary part of a complex number.*

Proof: In a typical LOS computation unit, i.e., Ω_{L}, there is that $i = 0$. As shown in Fig. 4.4a, in the polar coordinate system (R, θ), the area containing the intended signal sources is denoted by $\Omega_{P_{\mathrm{L}}}$. It is divided into $\Omega_{P_{\mathrm{L}0}}$ and $\Omega_{P_{\mathrm{L}1}}$ by r_0, which can be denoted by

$$\Omega_{P_{\mathrm{L}0}} \triangleq \left\{ (R, \theta) \left| \left(0 < R \le r_0 \right) \wedge \left(\theta_{\mathrm{e}} < \theta < \theta_{\mathrm{E}} \right) \right. \right\}, \tag{4.24}$$

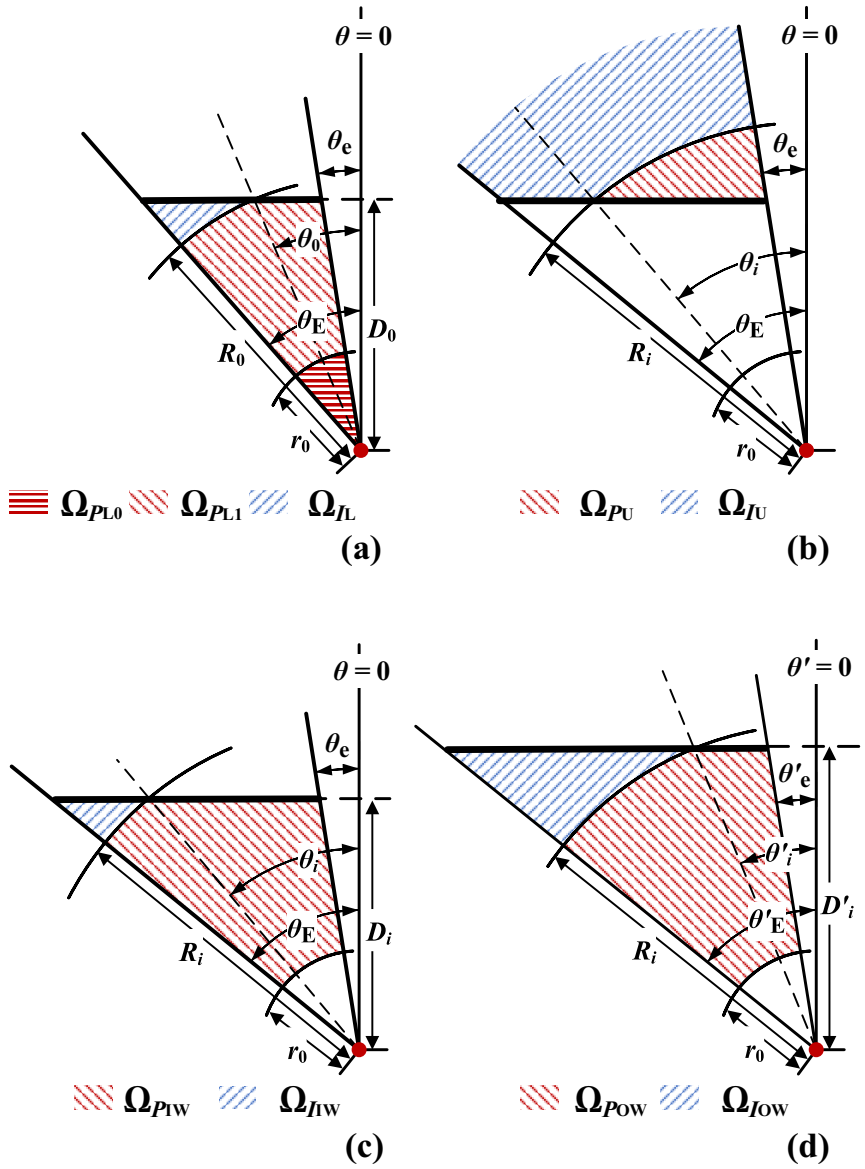

Fig. 4.4 Models of computation.

and

$$\Omega_{P_{\mathrm{L}1}} \triangleq \left\{ (R,\theta) \middle| \left(r_0 < R < \frac{D_0}{\cos(\theta)} \right) \wedge (\theta_{\mathrm{e}} < \theta < \theta_0) \right\} \vee \left\{ (R,\theta) \middle| (r_0 < R < R_0) \wedge (\theta_0 \le \theta < \theta_{\mathrm{E}}) \right\}, \tag{4.25}$$

where θ_{e}, θ_{E}, and D_0 are defined in Section 4.3.2 for Ω_{L}, R_0 is given by (4.9), and θ_0 is given by (4.20). The operators "$\wedge$" and "$\vee$" denote the logical conjunction and the logical

disjunction, respectively. The breakpoint r_0 given in (4.21) is from (4.7), which is obtained by solving the equation $\left(\frac{\lambda}{4\pi}\right)^2 r_0^{-n} = 1$.

For $0 \leq z_1 < z_2 < \frac{\pi}{2}$, $z_3 > 0$, $z_4 > 0$, and $z_5 \geq 0$, the functions $Z_1(\cdot)$ and $Z_0(\cdot)$ are defined as

$$Z_1(z_1, z_2, z_3, z_4, z_5) = \int_{z_1}^{z_2} \int_{z_3}^{\frac{z_4}{\cos(\theta)}} R^{-z_5} \mathrm{d}R\mathrm{d}\theta, \tag{4.26}$$

and

$$Z_0(z_1, z_2, z_3, z_4, z_5) = \int_{z_1}^{z_2} \int_{z_3}^{z_4} R^{-z_5} \mathrm{d}R\mathrm{d}\theta, \tag{4.27}$$

respectively. The closed-form expressions of $Z_1(\cdot)$ and $Z_0(\cdot)$ are given in [20] as (4.22) and (4.23), respectively. The derivation of (4.23) is straightforward thereby omitted here. The detailed derivations of (4.22) omitted in [20] are given in Appendix A.

The intended signal power from Ω_{L} is computed by

$$\begin{aligned} P_{\mathrm{L}} =& \int_{\Omega_{P_{\mathrm{L}0}}} P_{\mathrm{T}} G(R,0) \mathrm{d}\Omega + \int_{\Omega_{P_{\mathrm{L}1}}} P_{\mathrm{T}} G(R,0) \mathrm{d}\Omega \\ =& \int_{\theta_{\mathrm{e}}}^{\theta_{\mathrm{E}}} \int_0^{r_0} P_{\mathrm{T}} R \mathrm{d}R\mathrm{d}\theta + \int_{\theta_{\mathrm{e}}}^{\theta_0} \int_{r_0}^{\frac{D_0}{\cos(\theta)}} P_{\mathrm{T}} \left(\frac{\lambda}{4\pi}\right)^2 R^{1-n} \mathrm{d}R\mathrm{d}\theta \\ &+ \int_{\theta_0}^{\theta_{\mathrm{E}}} \int_{r_0}^{R_0} P_{\mathrm{T}} \left(\frac{\lambda}{4\pi}\right)^2 R^{1-n} \mathrm{d}R\mathrm{d}\theta \\ =& \frac{1}{2} P_{\mathrm{T}} r_0^2 (\theta_{\mathrm{E}} - \theta_{\mathrm{e}}) + P_{\mathrm{T}} \left(\frac{\lambda}{4\pi}\right)^2 Z_1(\theta_{\mathrm{e}}, \theta_0, r_0, D_0, n-1) \\ &+ P_{\mathrm{T}} \left(\frac{\lambda}{4\pi}\right)^2 Z_0(\theta_0, \theta_{\mathrm{E}}, r_0, R_0, n-1), \end{aligned} \tag{4.28}$$

where the closed-form expressions of $Z_1(\cdot)$ and $Z_0(\cdot)$ are given in (4.22) and (4.23), respectively. Then (4.18) can be obtained after simplification.

As shown in Fig. 4.4a, the area containing the interference sources can be denoted by

$$\Omega_{I_{\mathrm{L}}} \triangleq \left\{ (R,\theta) \middle| \left(R_0 \leq R < \frac{D_0}{\cos(\theta)} \right) \wedge (\theta_0 < \theta < \theta_{\mathrm{E}}) \right\}. \tag{4.29}$$

The interference power from Ω_{L} can be computed by

$$\begin{aligned} I_{\mathrm{L}} &= \int_{\Omega_{I_{\mathrm{L}}}} P_{\mathrm{T}} G(R,0)\mathrm{d}\Omega \\ &= \int_{\theta_0}^{\theta_{\mathrm{E}}} \int_{R_0}^{\frac{D_0}{\cos(\theta)}} P_{\mathrm{T}} \left(\frac{\lambda}{4\pi}\right)^2 R^{1-n}\mathrm{d}R\mathrm{d}\theta \\ &= P_{\mathrm{T}} \left(\frac{\lambda}{4\pi}\right)^2 Z_1\left(\theta_0, \theta_{\mathrm{E}}, R_0, D_0, n-1\right). \end{aligned} \tag{4.30}$$

■

Theorem 4.3. *The intended signal power and the interference power from a typical indoor NLOS computation unit Ω_{F} can be computed by*

$$P_{\mathrm{F}} = P_{\mathrm{T}} A^i \left(\frac{\lambda}{4\pi}\right)^2 \left[\begin{array}{l} Z_1\left(\theta'_{\mathrm{e}}, \theta'_i, r_0, D'_i, n-1\right) \\ +Z_0\left(\theta'_i, \theta'_{\mathrm{E}}, r_0, R_i, n-1\right) \\ -Z_1\left(\theta_{\mathrm{e}}, \theta_i, r_0, D_i, n-1\right) \\ -Z_0\left(\theta_i, \theta_{\mathrm{E}}, r_0, R_i, n-1\right) \end{array}\right], \tag{4.31}$$

and

$$I_{\mathrm{F}} = P_{\mathrm{T}} A^i \left(\frac{\lambda}{4\pi}\right)^2 \left[\begin{array}{l} Z_1\left(\theta'_i, \theta'_{\mathrm{E}}, R_i, D'_i, n-1\right) \\ -Z_1\left(\theta_i, \theta_{\mathrm{E}}, R_i, D_i, n-1\right) \end{array}\right], \tag{4.32}$$

where

$$\theta_i = \mathrm{median}\left\{\theta_{\mathrm{e}}, \theta_{\mathrm{E}}, \arccos\left(\frac{D_i}{\max\left\{D_i, R_i\right\}}\right)\right\}, \tag{4.33}$$

and

$$\theta'_i = \mathrm{median}\left\{\theta'_{\mathrm{e}}, \theta'_{\mathrm{E}}, \arccos\left(\frac{D'_i}{\max\left\{D'_i, R_i\right\}}\right)\right\}. \tag{4.34}$$

The parameters θ_{e}, θ_{E}, θ'_{e}, θ'_{E}, D_i, and D'_i are defined in Section 4.3.2 for Ω_{F}, while R_i is given by (4.9). The functions $Z_1(\cdot)$ and $Z_0(\cdot)$ are given by (4.22) and (4.23), respectively.

Proof: As shown in Fig. 4.3c-d, a typical NLOS computation unit Ω_{F} can be considered as the subtraction of two triangles. As shown in Fig. 4.4c, the triangle with the first wall traversed by the signals from Ω_{F} is denoted by Ω_{IW}. As shown in Fig. 4.4d, the triangle with the wall not traversed by signals from Ω_{F} is denoted by Ω_{OW}. As shown in Fig. 4.4c, in

the polar coordinate system (R,θ) for Ω_{IW}, the area that could contain the intended signal sources can be denoted by

$$\begin{aligned}\Omega_{P_{\mathrm{IW}}} \triangleq &\left\{(R,\theta)\middle|\left(r_0 < R < \frac{D_i}{\cos(\theta)}\right) \wedge (\theta_{\mathrm{e}} < \theta < \theta_i)\right\} \\ &\vee \left\{(R,\theta)\middle|(r_0 < R < R_i) \wedge (\theta_i \leq \theta < \theta_{\mathrm{E}})\right\},\end{aligned} \tag{4.35}$$

where θ_{e}, θ_{E}, and D_i are defined in Section 4.3.2 for Ω_{F}. The parameters R_i and θ_i are given by (4.9) and (4.33), respectively. As shown in Fig. 4.4d, in the polar coordinate system (R,θ') for Ω_{OW}, the area that could contain the intended signal sources can be denoted by

$$\begin{aligned}\Omega_{P_{\mathrm{OW}}} \triangleq &\left\{(R,\theta')\middle|\left(r_0 < R < \frac{D'_i}{\cos(\theta')}\right) \wedge \left(\theta'_{\mathrm{e}} < \theta' < \theta'_i\right)\right\} \\ &\vee \left\{(R,\theta')\middle|(r_0 < R < R_i) \wedge \left(\theta'_i \leq \theta' < \theta'_{\mathrm{E}}\right)\right\},\end{aligned} \tag{4.36}$$

where θ'_{e}, θ'_{E}, and D'_i are defined in Section 4.3.2 for Ω_{F} and θ'_i is given by (4.34). The intended signal power from Ω_{F} can be computed by

$$\begin{aligned}P_{\mathrm{F}} =& \int_{\Omega_{P_{\mathrm{OW}}}} P_{\mathrm{T}} G(R,i)\mathrm{d}\Omega - \int_{\Omega_{P_{\mathrm{IW}}}} P_{\mathrm{T}} G(R,i)\mathrm{d}\Omega \\ =& \int_{\theta'_{\mathrm{e}}}^{\theta'_i} \int_{r_0}^{\frac{D'_i}{\cos(\theta')}} P_{\mathrm{T}} A^i \left(\frac{\lambda}{4\pi}\right)^2 R^{1-n}\mathrm{d}R\mathrm{d}\theta' \\ &+ \int_{\theta'_i}^{\theta'_{\mathrm{E}}} \int_{r_0}^{R_i} P_{\mathrm{T}} A^i \left(\frac{\lambda}{4\pi}\right)^2 R^{1-n}\mathrm{d}R\mathrm{d}\theta' \\ &- \int_{\theta_{\mathrm{e}}}^{\theta_i} \int_{r_0}^{\frac{D_i}{\cos(\theta)}} P_{\mathrm{T}} A^i \left(\frac{\lambda}{4\pi}\right)^2 R^{1-n}\mathrm{d}R\mathrm{d}\theta \\ &- \int_{\theta_i}^{\theta_{\mathrm{E}}} \int_{r_0}^{R_i} P_{\mathrm{T}} A^i \left(\frac{\lambda}{4\pi}\right)^2 R^{1-n}\mathrm{d}R\mathrm{d}\theta \\ =& P_{\mathrm{T}} A^i \left(\frac{\lambda}{4\pi}\right)^2 Z_1\left(\theta'_{\mathrm{e}}, \theta'_i, r_0, D'_i, n-1\right) \\ &+ P_{\mathrm{T}} A^i \left(\frac{\lambda}{4\pi}\right)^2 Z_0\left(\theta'_i, \theta'_{\mathrm{E}}, r_0, R_i, n-1\right) \\ &- P_{\mathrm{T}} A^i \left(\frac{\lambda}{4\pi}\right)^2 Z_1\left(\theta_{\mathrm{e}}, \theta_i, r_0, D_i, n-1\right) \\ &- P_{\mathrm{T}} A^i \left(\frac{\lambda}{4\pi}\right)^2 Z_0\left(\theta_i, \theta_{\mathrm{E}}, r_0, R_i, n-1\right),\end{aligned} \tag{4.37}$$

where $Z_1(\cdot)$ and $Z_0(\cdot)$ are defined in (4.26) and (4.27), respectively, and the closed-form expressions are given in (4.22) and (4.23), respectively. Then (4.31) can be obtained after simplification.

The areas that could contain the interference sources in Ω_{OW} and Ω_{IW} can be denoted by

$$\Omega_{I_{\mathrm{IW}}} \triangleq \left\{ (R,\theta) \middle| \left(R_i \le R < \frac{D_i}{\cos(\theta)} \right) \wedge (\theta_i < \theta < \theta_{\mathrm{E}}) \right\}, \tag{4.38}$$

and

$$\Omega_{I_{\mathrm{OW}}} \triangleq \left\{ (R,\theta') \middle| \left(R_i \le R < \frac{D_i'}{\cos(\theta')} \right) \wedge (\theta_i' < \theta' < \theta_{\mathrm{E}}') \right\}. \tag{4.39}$$

The interference power from Ω_{F} can be computed by

$$\begin{aligned} I_{\mathrm{F}} =& \int_{\Omega_{I_{\mathrm{OW}}}} P_{\mathrm{T}} G(R,i) \mathrm{d}\Omega - \int_{\Omega_{I_{\mathrm{IW}}}} P_{\mathrm{T}} G(R,i) \mathrm{d}\Omega, \\ =& \int_{\theta_i'}^{\theta_{\mathrm{E}}'} \int_{R_i}^{\frac{D_i'}{\cos(\theta')}} P_{\mathrm{T}} A^i \left(\frac{\lambda}{4\pi} \right)^2 R^{1-n} \mathrm{d}R\mathrm{d}\theta' \\ & - \int_{\theta_i}^{\theta_{\mathrm{E}}} \int_{R_i}^{\frac{D_i}{\cos(\theta)}} P_{\mathrm{T}} A^i \left(\frac{\lambda}{4\pi} \right)^2 R^{1-n} \mathrm{d}R\mathrm{d}\theta \\ =& P_{\mathrm{T}} A^i \left(\frac{\lambda}{4\pi} \right)^2 Z_1\left(\theta_i', \theta_{\mathrm{E}}', R_i, D_i', n-1\right) \\ & - P_{\mathrm{T}} A^i \left(\frac{\lambda}{4\pi} \right)^2 Z_1\left(\theta_i, \theta_{\mathrm{E}}, R_i, D_i, n-1\right), \end{aligned} \tag{4.40}$$

and then (4.32) can be obtained after simplification. ■

Theorem 4.4. *The intended signal power and the interference power from a typical outdoor NLOS computation unit Ω_{U} can be computed by*

$$P_{\mathrm{U}} = -P_{\mathrm{T}} A^i \left(\frac{\lambda}{4\pi} \right)^2 Z_1\left(\theta_{\mathrm{e}}, \theta_i, R_i, D_i, n-1\right), \tag{4.41}$$

and

$$I_{\mathrm{U}} = P_{\mathrm{T}} A^i \left(\frac{\lambda}{4\pi} \right)^2 \left[\begin{array}{l} Z_0\left(\theta_{\mathrm{e}}, \theta_i, R_i, +\infty, n-1\right) \\ -Z_1\left(\theta_i, \theta_{\mathrm{E}}, +\infty, D_i, n-1\right) \end{array} \right], \tag{4.42}$$

where θ_{e}, θ_{E} and, D_i are defined in Section 4.3.2 for Ω_{U}, while R_i and θ_i are given by (4.9) and (4.33), respectively. The functions $Z_1(\cdot)$ and $Z_0(\cdot)$ are given by (4.22) and (4.23), respectively.

Proof: As shown in Fig. 4.4b, in the polar coordinate system (R,θ) for Ω_{U}, the area containing the intended signal sources can be denoted by

$$\Omega_{P_{\mathrm{U}}} \triangleq \left\{ (R,\theta) \middle| \left(\frac{D_i}{\cos(\theta)} \leq R < R_i \right) \wedge (\theta_{\mathrm{e}} < \theta < \theta_i) \right\}, \tag{4.43}$$

where θ_{e}, θ_{E}, and D_i are defined in Section 4.3.2 for Ω_{U}, R_i is given in (4.9), and θ_i can be obtained by (4.33). The intended signal power from Ω_{U} can be computed by

$$\begin{aligned} P_{\mathrm{U}} &= \int_{\Omega_{P_{\mathrm{U}}}} P_{\mathrm{T}} G(R,i) \mathrm{d}\Omega \\ &= \int_{\theta_{\mathrm{e}}}^{\theta_i} \int_{\frac{D_i}{\cos(\theta)}}^{R_i} P_{\mathrm{T}} A^i \left(\frac{\lambda}{4\pi} \right)^2 R^{1-n} \mathrm{d}R\mathrm{d}\theta \\ &= - P_{\mathrm{T}} A^i \left(\frac{\lambda}{4\pi} \right)^2 Z_1(\theta_{\mathrm{e}}, \theta_i, R_i, D_i, n-1), \end{aligned} \tag{4.44}$$

where $Z_1(\cdot)$ is defined in (4.26) and the closed-form expression is given in (4.22).

The area containing interference sources in Ω_{U} can be denoted by

$$\begin{aligned} \Omega_{I_{\mathrm{U}}} \triangleq & \{ (R,\theta) | (R \geq R_i) \wedge (\theta_{\mathrm{e}} < \theta < \theta_i) \} \\ & \vee \left\{ (R,\theta) \middle| \left(R \geq \frac{D_i}{\cos(\theta)} \right) \wedge (\theta_i \leq \theta < \theta_{\mathrm{E}}) \right\}. \end{aligned} \tag{4.45}$$

The interference power from Ω_{U} can be derived by

$$\begin{aligned} I_{\mathrm{U}} &= \int_{\Omega_{I_{\mathrm{U}}}} P_{\mathrm{T}} G(R,i) \mathrm{d}\Omega \\ &= \int_{\theta_{\mathrm{e}}}^{\theta_i} \int_{R_i}^{+\infty} P_{\mathrm{T}} A^i \left(\frac{\lambda}{4\pi} \right)^2 R^{1-n} \mathrm{d}R\mathrm{d}\theta \\ &\quad + \int_{\theta_i}^{\theta_{\mathrm{E}}} \int_{\frac{D_i}{\cos(\theta)}}^{+\infty} P_{\mathrm{T}} A^i \left(\frac{\lambda}{4\pi} \right)^2 R^{1-n} \mathrm{d}R\mathrm{d}\theta \\ &= P_{\mathrm{T}} A^i \left(\frac{\lambda}{4\pi} \right)^2 Z_0(\theta_{\mathrm{e}}, \theta_i, R_i, +\infty, n-1) \\ &\quad - P_{\mathrm{T}} A^i \left(\frac{\lambda}{4\pi} \right)^2 Z_1(\theta_i, \theta_{\mathrm{E}}, +\infty, D_i, n-1), \end{aligned} \tag{4.46}$$

where $Z_0(\cdot)$ is defined in (4.27) and the closed-form expression is given in (4.23). Then (4.42) can be obtained after simplification. ■

Note that same transmit power is assumed for both indoor and outdoor transmit elements throughout this chapter for the sake of simplicity. To incorporate the difference of the transmit power between indoor and outdoor transmit elements in the evaluation scheme, P_{T} in Theorem 4.4 can be defined individually according to practical outdoor environments.

4.3.4 Computation of the PG and the IG

With the proposed analytical models, g_{P} and g_{I} of a probing UE location in a given building under design consisting of polygonal-shaped rooms can be obtained as follows:

1. building up the propagation environment model, which includes the building plan, the wall attenuation factor A, the PLE n, and the thermal noise σ^2;
2. defining the primary network parameters, including the transmit power density P_{T}, the threshold P_{th}, the carrier frequency f_{c}, and the location of the probing UE;
3. computing the intended signal power and the interference power in open space, i.e., P_{O} and I_{O}, by Theorem 4.1;
4. dividing the building plan into multiple computation units about the probing UE; computing the intended signal power and the interference power from each computation unit by Theorem 4.2; computing the total received intended signal power and the total received interference power for the in-building scenario, i.e., P_{B} and I_{B}, by (4.16) and (4.17), respectively; and then
5. computing g_{P} and g_{I} by (4.3) and (4.4), respectively.

4.4 Validations

Here the analytical models are validated by the Monte Carlo simulations in the sample building shown in Fig. 4.2, which consists of 9 rooms with dimensions 10 m$\times$10 m. The network parameters $P_{\mathrm{T}} = -30$ dBWm^{-2} and $P_{\mathrm{th}} = -110$ dBWm^{-2}. The wall attenuation factor $A_{\mathrm{dB}} = 5$ dB, the PLE $n = 4$, and $\sigma^2 = -98$ dBm. For the Monte Carlo simulations, a large number of transmit elements and a large simulation radius R_{sim} [m] are employed to approximate the assumed theoretical network model, where each Tx-Rx link to the probing UE is with a random direction in $[0, 2\pi)$ and a random link length in $(0, R_{\mathrm{sim}})$. The transmit

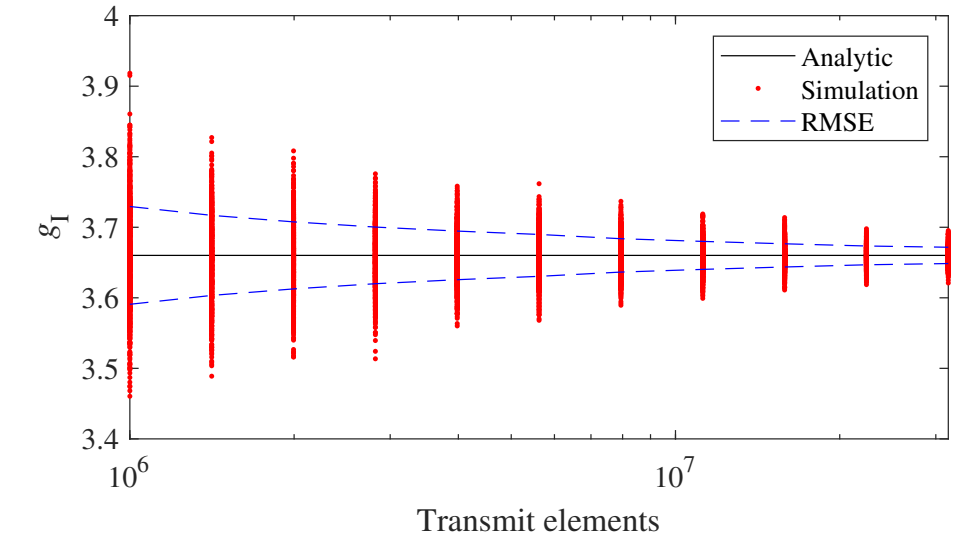

(a) g_{I}

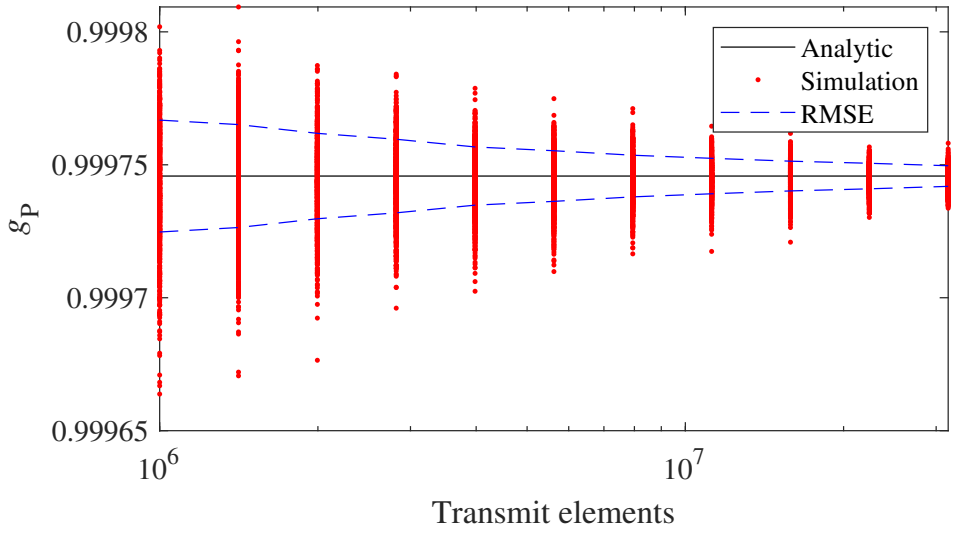

(b) g_{P}

Fig. 4.5 Simulation results on UE 1 at 1 GHz vary with the number of transmit elements.

power of each transmit element is weighed by the Tx-Rx link length to ensure a transmit power density of P_{T} in an arbitrary area. The received signal power from each transmit element is computed by the path gain model given in (4.7), where the number of walls intersecting a Tx-Rx link, i.e., i, is counted site-specifically for the in-building scenario. The intended signal and interference are distinguished by comparing the link length with R_i given by (4.9). Fig. 4.5 illustrates how the results of the Monte Carlo simulations vary with the number of the transmit elements on UE 1, where $R_{\mathrm{sim}} = 2 \times 10^3$ m. As the number of transmit

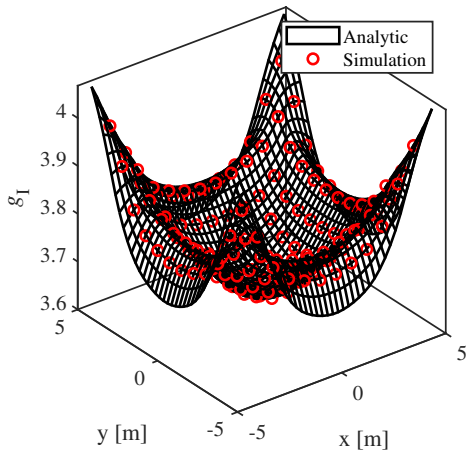

(a) g_I in the 1-GHz band.

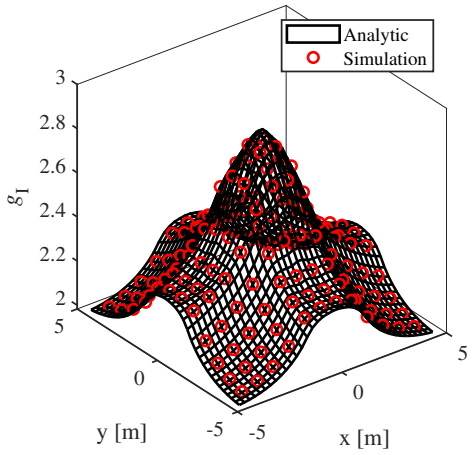

(b) g_I in the 6-GHz band.

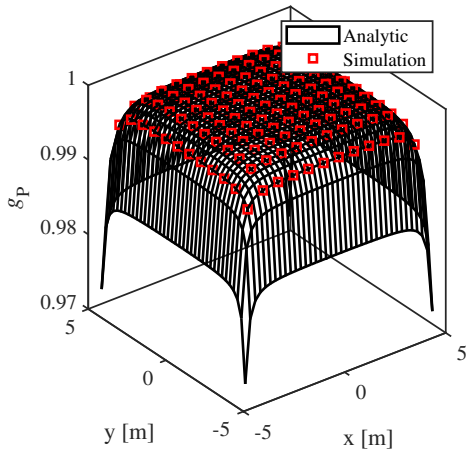

(c) g_P in the 1-GHz band.

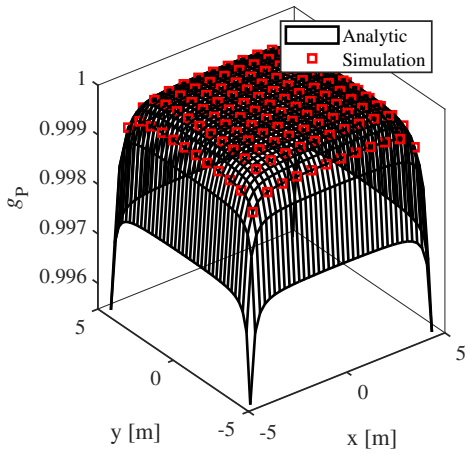

(d) g_P in the 6-GHz band.

Fig. 4.6 g_I and g_P in the centre room of the sample building in Fig. 4.2. The lines are computed by the analytical models, while the markers are generated by the Monte Carlo simulations.

elements increases, the root-mean-square error (RMSE) decreases while the time needed to conduct the simulation becomes longer. Fig. 4.6 shows g_P and g_I derived in the centre room of the sample building in the 1-GHz and 6-GHz bands by both the proposed analytical models and the Monte Carlo simulations. For each probing UE location, the simulated g_P and g_I are the mean values of the results of 10^2 simulation realisations, where 10^7 transmit elements are randomly placed in each realisation. With the closed-form expressions, the proposed analytical models can obtain g_P and g_I in a given building computational-efficiently. As shown in Fig. 4.6, the analytic results agree with the simulations well.

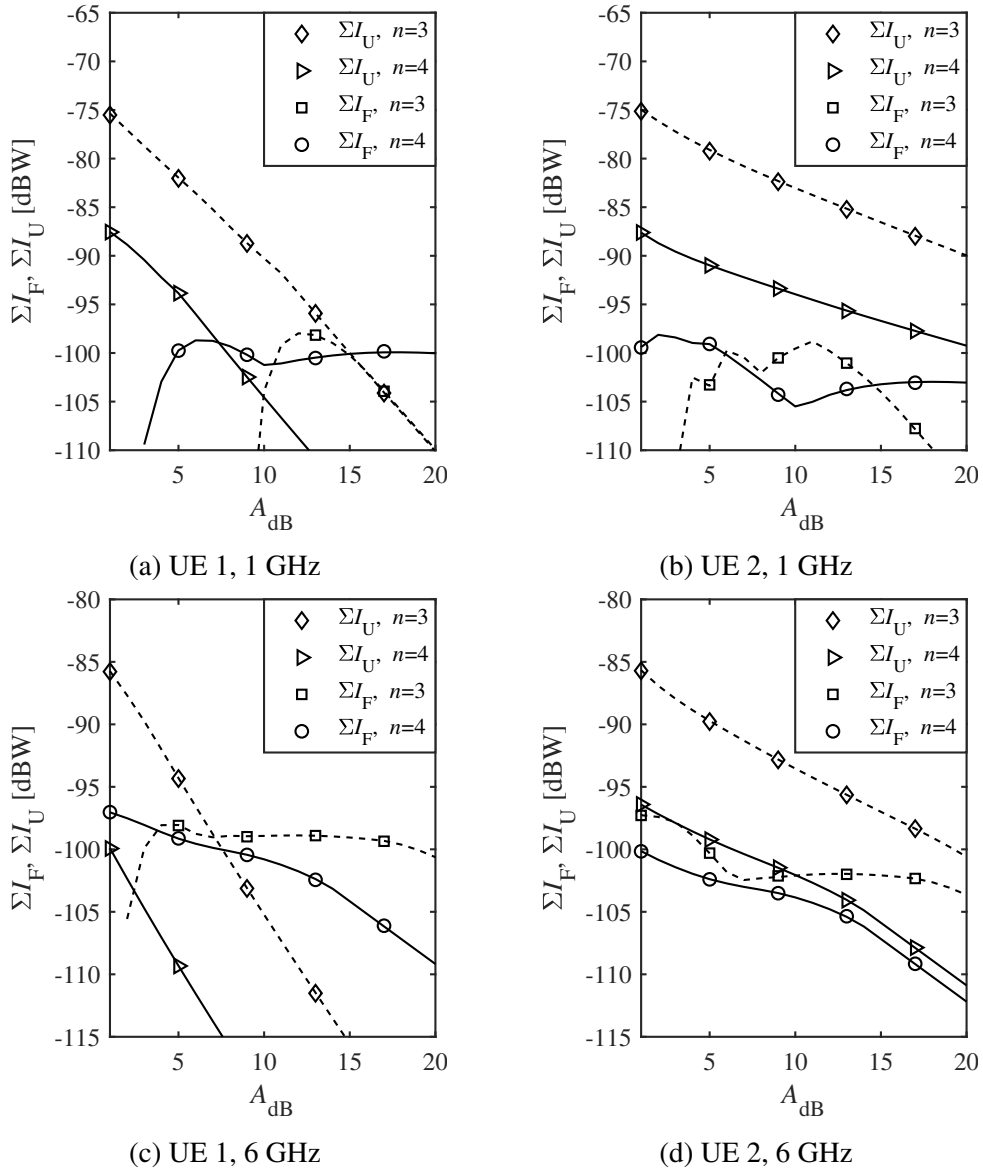

(a) UE 1, 1 GHz

(b) UE 2, 1 GHz

(c) UE 1, 6 GHz

(d) UE 2, 6 GHz

Fig. 4.7 NLOS interference signal power on UE 1 and UE 2 in Fig. 4.2. The lines are computed by the analytical models, while the markers are generated by the Monte Carlo simulations.

Comparing Fig. 4.6a and 4.6b, the distributions of g_{I} differ significantly in the 1-GHz and 6-GHz bands. Inserting $i = 0$ and $i = 1$ into (4.9), it has $R_0 = 15.45$ m and $R_1 = 11.59$ m in the 1-GHz band, and $R_0 = 6.31$ m and $R_1 = 4.73$ m in the 6-GHz band. Consequently, in the 1-GHz band, the LOS signals received by a probing UE in the centre room are all intended signals. UE in the centre is with lower g_{I} than in the corner, as it receives more NLOS interference signals from neighbouring rooms. In the 6-GHz band, UE in the corner is with lower g_{I} since it receives strong LOS interference signals from the opposite corner of the

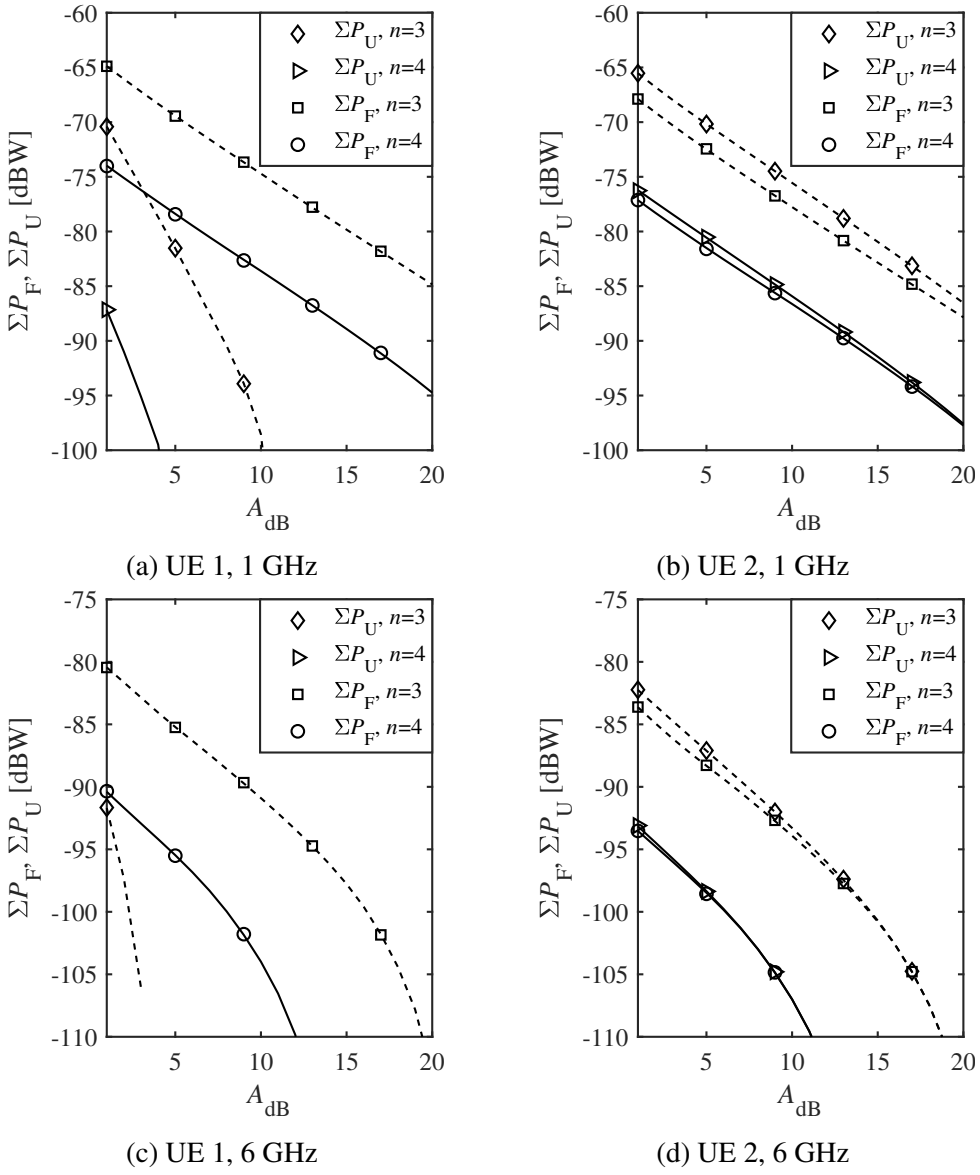

(a) UE 1, 1 GHz

(b) UE 2, 1 GHz

(c) UE 1, 6 GHz

(d) UE 2, 6 GHz

Fig. 4.8 NLOS intended signal power on UE 1 and UE 2 in Fig. 4.2. The lines are computed by the analytical models, while the markers are generated by the Monte Carlo simulations.

room, while UE in the centre is with higher g_I since the walls can block the LOS interference signals. As shown in Fig. 4.6c-d, g_P shows similar trends in the 1-GHz and 6-GHz bands. It is higher in the 6-GHz band since the LOS intended signal power takes a larger proportion than in the 1-GHz band. UE close to the edges of each room is with lower g_P, as it receives less LOS intended signal power than those in the centre due to the shape of the room.

As marked in Fig. 4.2, UE 1 and UE 2 are located in the centres of the rooms in the centre and a corner of the sample building, respectively. To explore how the relative position of a room in a building affects the BWP, the NLOS intended signal power and the NLOS

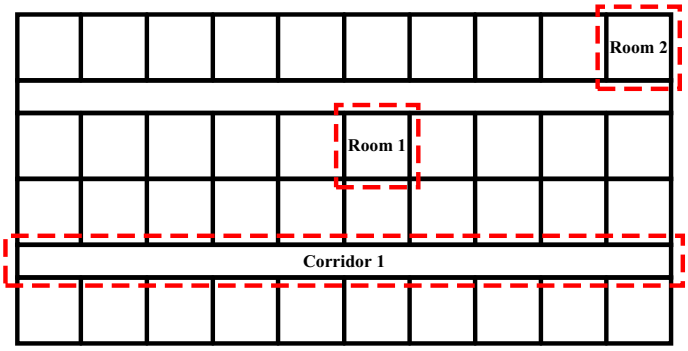

Fig. 4.9 WINNER II A1 scenario. Room 1 and Room 2 are two typical rooms located in the centre and a corner of the building, respectively, and Corridor 1 is a long corridor with multiple rooms on either side.

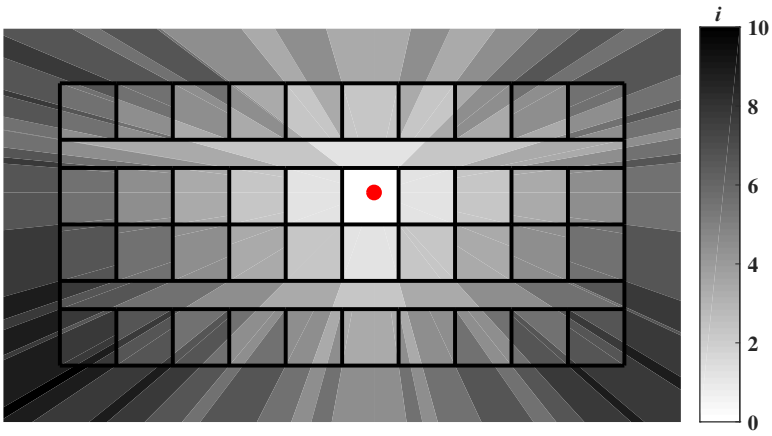

Fig. 4.10 The number of walls intersecting the Tx-Rx links to a probing UE location.

interference power received by UE 1 and UE 2 are compared. The network parameters $P_{\mathrm{T}} = -30$ dBWm^{-2} and $P_{\mathrm{th}} = -120$ dBWm^{-2}. The wall attenuation factor A_{dB} in the sample building varies from 1-20 dB. The propagation environments are considered with the PLEs $n = 3$ and $n = 4$. In Fig. 4.7, $\sum I_{\mathrm{F}}$ and $\sum I_{\mathrm{U}}$ denote the total NLOS interference power received from indoors and outdoors, respectively. In Fig. 4.8, $\sum P_{\mathrm{F}}$ and $\sum P_{\mathrm{U}}$ denote the total NLOS intended signal power received from indoors and outdoors, respectively. As it shows that the analytic results match the simulations well.

As shown in Fig. 4.7, with the assumed parameters, $\sum I_{\mathrm{U}}$ is reduced as A_{dB} enlarges. It decreases more rapidly on UE 1 than UE 2, as all outdoor signals have to traverse two or more walls to reach UE 1. The indoor NLOS interference power $\sum I_{\mathrm{F}}$ shows no apparent pattern compared among the scenarios with different PLEs or carrier frequencies, for that as

A_{dB} enlarges, the enhancement of $\sum I_{\mathrm{F}}$ due to the extension of the area containing interference sources and the degradation due to the increasing penetration loss cancel each other in the complex indoor environment. As shown in Fig. 4.8, $\sum P_{\mathrm{F}}$ and $\sum P_{\mathrm{U}}$ decrease as A_{dB} increases, for that the intended signals are not only attenuated due to the increasing penetration loss but also partially turn to interference signals. For UE 1, the NLOS intended signal power is mostly from indoors, while for UE 2, it may evenly come from indoors and outdoors. Compared with $n = 3$, $\sum P_{\mathrm{U}}$ and $\sum P_{\mathrm{F}}$ are lower when $n = 4$ due to a more severe distance-dependent decay. Despite the same locations in a room with the same geometry, the NLOS signal power on UE 1 and UE 2 could differ significantly. Thus, the relative locations of rooms in a building should be considered in the BWP evaluation.

4.5 Numerical Results

4.5.1 Computation parameters

This section demonstrates the BWP evaluation in a typical office scenario, the WINNER II A1 scenario [32]. As shown in Fig. 4.9, it consists of 40 rooms with dimensions 10 m$\times$10 m and two corridors with dimensions 100 m$\times$5 m. As marked in Fig. 4.9, Room 1 and Room 2 are two typical rooms located in the centre and a corner of the building, and Corridor 1 is a long corridor with multiple rooms on either side. As shown in Fig. 4.10, for a probing UE, the building plan is first divided into multiple computation units according to the number of walls intersecting the Tx-Rx links. In the following computations, the PLE $n = 4$ and the network parameters $P_{\mathrm{T}} = -30$ dBWm^{-2} and $P_{\mathrm{th}} = -110$ dBWm^{-2}. Define the scenarios with the wall attenuation factors $A_{\mathrm{dB}} = 5$ dB and $A_{\mathrm{dB}} = 12$ dB as the light wall scenario and the heavy wall scenario, respectively [32]. g_{P} and g_{I} are computed in uniformly distributed UE locations across the scenario in both the 1-GHz and 6-GHz bands. Fig. 4.11 and Fig. 4.12 illustrate the distributions of g_{I} and g_{P}, respectively. Fig. 4.13 shows the cumulative distribution function (CDF) of $g_{\mathrm{P}}g_{\mathrm{I}}$ in the WINNER II A1 scenario.

4.5.2 Results and analysis

Fig. 4.11a-b show that the distribution of g_{I} varies significantly among different rooms in the 1-GHz band. Room 1 shows higher g_{I} than Room 2 since the NLOS interference signals can be attenuated by the corridors and edge rooms before reaching the centre. Fig. 4.11c-d show that the distribution of g_{I} is similar in different rooms in the 6-GHz band. Both Room 1 and Room 2 show higher g_{I} in the centre. The difference of g_{I} among UEs in each room is more considerable in the heavy wall scenario, as UEs in the centre receive both less LOS

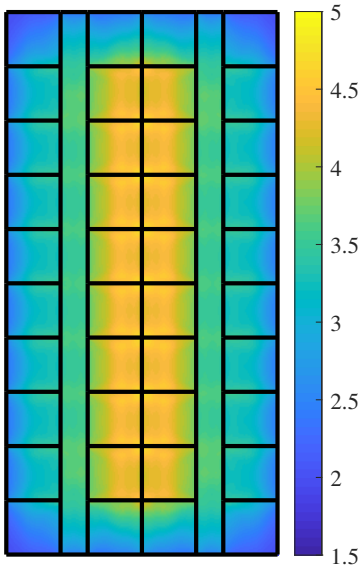

(a) 1 GHz, Light wall

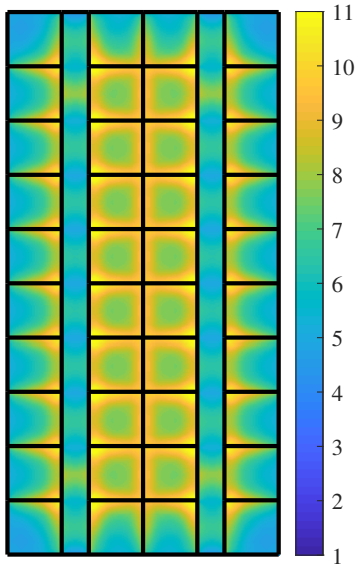

(b) 1 GHz, Heavy wall

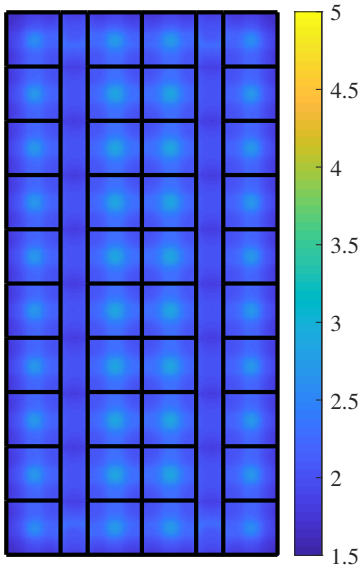

(c) 6 GHz, Light wall

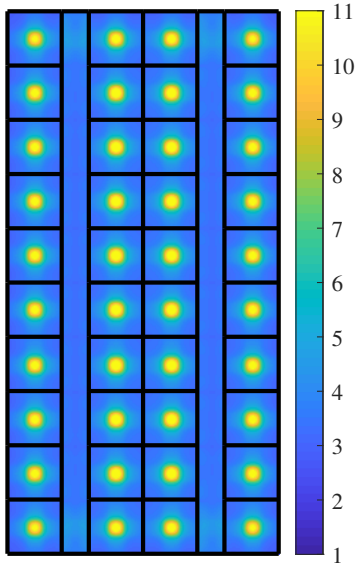

(d) 6 GHz, Heavy wall

Fig. 4.11 g_{I} in the WINNER II A1 scenario.

and NLOS interference power than UEs close to the edges. Furthermore, Corridor 1 shows relatively low g_{I}, as UEs in the corridor receive not only strong LOS interference signals but NLOS interference signals from the rooms on either side.

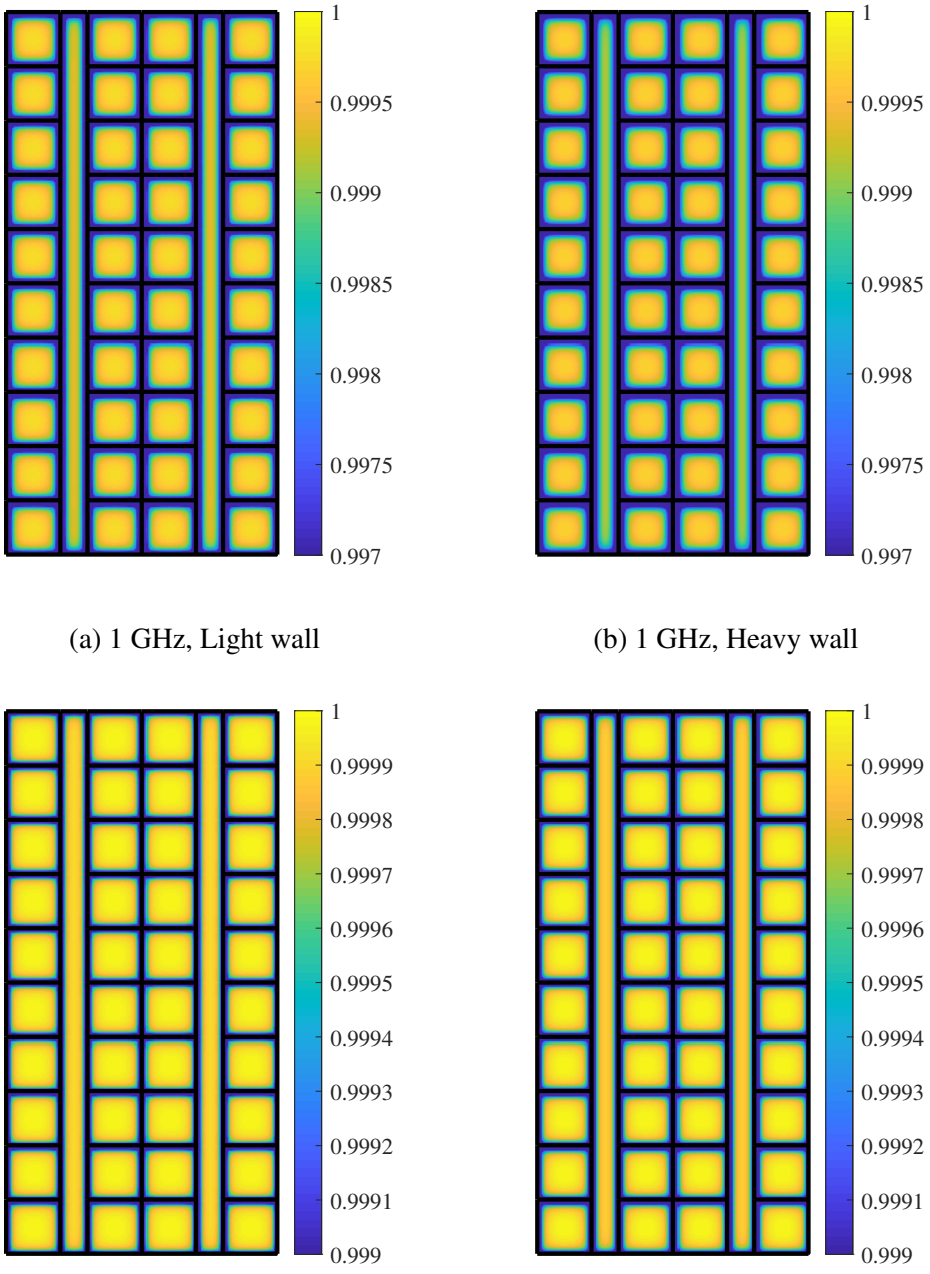

(a) 1 GHz, Light wall

(b) 1 GHz, Heavy wall

(c) 6 GHz, Light wall

(d) 6 GHz, Heavy wall

Fig. 4.12 g_{P} in the WINNER II A1 scenario.

As shown in Fig. 4.12, in both 1-GHz and 6-GHz bands, the heavy wall scenarios show lower g_{P} than the light wall scenarios for that the NLOS intended signals suffer more penetration loss. The PG g_{P} varies within a small range in the four combinations, which

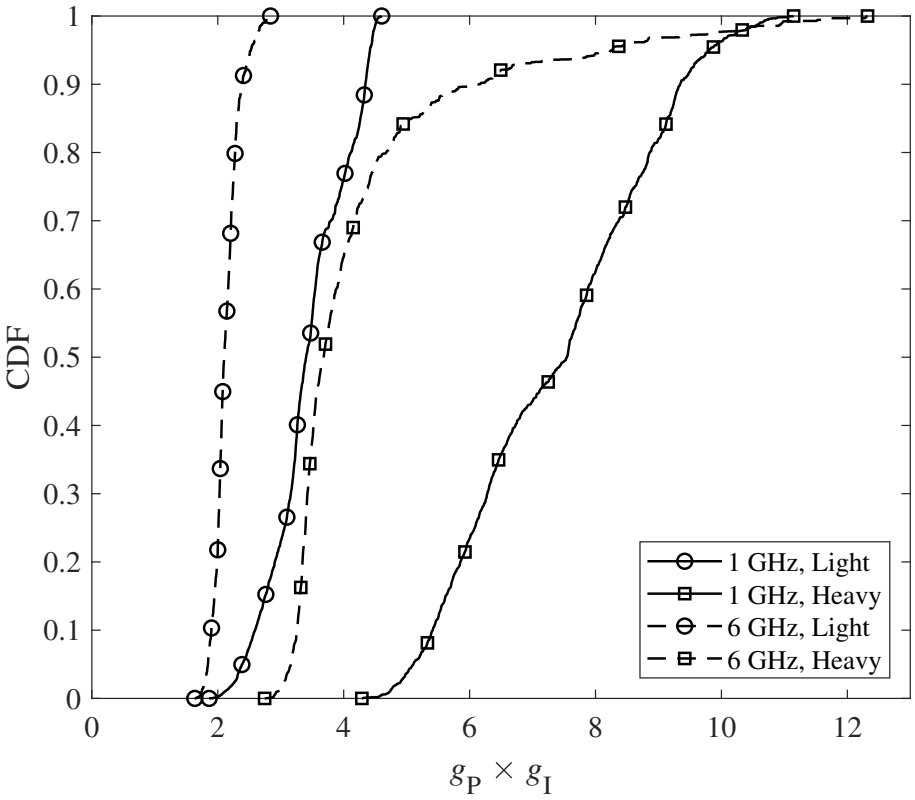

Fig. 4.13 The CDF of $g_P g_I$.

indicates that the blockage effects show a limited impact on g_P, as the received intended signal power mainly comes from the LOS transmitted elements.

As shown in Fig. 4.13, the WINNER II A1 scenario with heavy walls and a network operating in the 1-GHz band shows the best BWP among the four combinations in terms of average $g_P g_I$. Future wireless-friendly building design should target high g_P and g_I to make the most of building structures in achieving a relatively high SINR, especially in the areas with high user demands. Target values of g_P and g_I can be predefined according to the function of the building under design. Then, the proposed method can be employed by architectural practitioners to evaluate the BWP at the building design stage in real-time. If the design of the building can not achieve the predefined target BWP, architects could improve the BWP by choosing different building materials of some interior walls, changing layouts of rooms, or rearranging rooms.

4.6 Summary

In this chapter, a partition-based BWP evaluation scheme has been proposed. As in previous works discussing the BWP, the proposed approach in this chapter only applies to 2-D planes. The analytical models to compute the BWP FoMs, i.e., the PG and the IG, have been given in closed-form expressions and validated through Monte Carlo simulations. Compared with previous works, the partition-based BWP evaluation scheme employs a more comprehensive system model that includes the site-specific information. It enables the BWP FoMs to capture the impact of building materials and layouts on indoor wireless network performance.

Chapter 5

On Evaluation of Wireless Performance for Multi-Storey Buildings

Overview

The state-of-the-art works and Chapter 4 evaluated the BWP on a 2-D plane without considering the Tx-Rx height difference and the cross-floor associations/interference. This chapter proposes a multi-storey BWP evaluation scheme to enable the BWP evaluation for multi-storey buildings in 3-D space. The BWP FoMs, i.e., the PG and the IG, are defined for multi-storey buildings. In the system model, the transmit elements are assumed on multiple parallel planes. The path gain model distinguishes LOS and NLOS Tx-Rx links. The analytical models to compute the BWP FoMs are derived in closed-form expressions and validated by Monte Carlo simulations. The proposed method addresses the effects of 3-D building properties, including the number of storeys and their height, on indoor wireless network performance.

5.1 Introduction

5.1.1 Background and motivations

The analytical models computing the BWP FoMs given in [19–22], as well as the approach proposed in Chapter 4, are dedicated to the scenario that transmit elements and UE are with the same heights, which means that they are only valid on a 2-D plane. However, in a practical multi-storey building, the wireless transmit elements are commonly installed on the ceiling of each storey, which results in the appearance of the Tx-Rx height difference and the cross-floor associations/interference. In indoor scenarios, the Tx-Rx height difference is

comparable to the length of the projection of the Tx-Rx link on the ground, which means that the impact of building structures on indoor networks should be considered in 3-D space. In this chapter, a multi-storey BWP evaluation scheme is proposed to enable the analysis of the BWP in 3-D space.

5.1.2 Contributions in this chapter

The contributions of this chapter are summarised as follows.

- This chapter presents the definitions of the BWP FoMs, i.e., the IG and the PG, for multi-storey buildings. The BWP FoMs defined in this chapter introduce 3-D building layout parameters, including the number of storeys and their height, to the BWP evaluation. The Tx-Rx links are distinguished into the LOS and NLOS scenarios, and the path gains are computed with corresponding PLEs defined according to the characteristics of the propagation environment.
- The analytical models of the BWP FoMs are given in closed-form expressions and validated by Monte Carlo simulations. The proposed models enable the BWP evaluation in 3-D space with a low computational burden. Numerical results are generated for a typical toy model (TM) defined in this chapter with respect to different input parameters, including relative UE locations, PLEs, and basic network parameters, to analyse their roles to the BWP.
- The BWP evaluation is demonstrated in a 5-storey office building. The impact of the number of storeys and their height on the BWP in different frequency bands is analysed. The evaluation results are compared with those generated by the 2-D BWP evaluation scheme in [19–22] to explore the BWP under different system models.

5.2 BWP FoMs for multi-storey buildings

Here the BWP FoMs, i.e., the PG and the IG, are defined for multi-storey buildings, where PG indicates the impact of building structures on the intended signal power, while IG indicates it on the undesired power, i.e., the interference and thermal noise power [19–22].

The SINR of the probing UE in a K-storey building is defined as

$$\gamma_{\mathrm{B}} = \frac{\sum_{k=1}^{K} P_{\mathrm{B},k}}{\sum_{k=1}^{K} I_{\mathrm{B},k} + \sigma^2}, \tag{5.1}$$

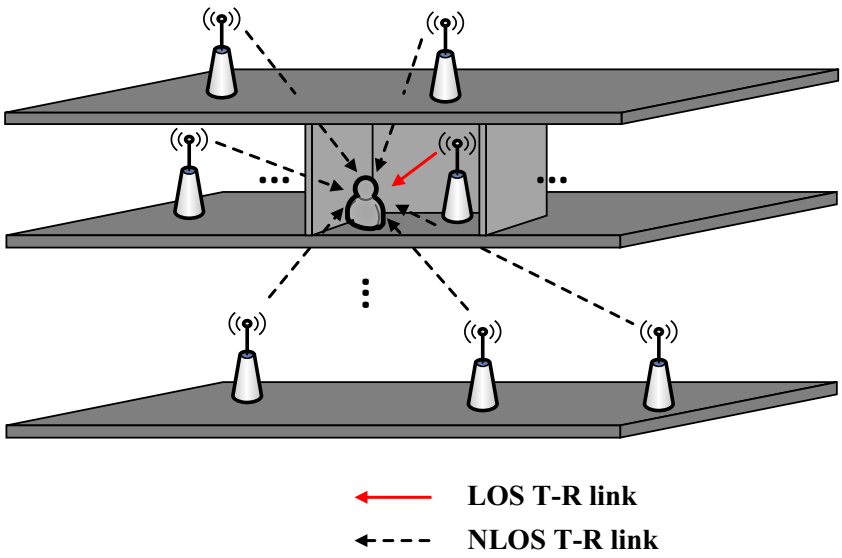

Fig. 5.1 The indoor wireless network in a multi-storey building.

where $P_{\mathrm{B},k}$ and $I_{\mathrm{B},k}$ denote the intended signal power and the interference power received from the k-th floor. σ^2 represents the thermal noise power. The SINR for the probing UE in open space is defined as γ_{O}, and the intended signal power and the interference power from transmit elements in open space are denoted by P_{O} and I_{O}.

For a K-storey building, the PG and the IG are defined as

$$g_{\mathrm{P}} \triangleq \frac{\sum_{k=1}^{K} P_{\mathrm{B},k}}{P_{\mathrm{O}}}, \tag{5.2}$$

and

$$g_{\mathrm{I}} \triangleq \frac{I_{\mathrm{O}} + \sigma^2}{\sum_{k=1}^{K} I_{\mathrm{B},k} + \sigma^2}, \tag{5.3}$$

respectively. The product of g_{I} and g_{P} is the ratio of the SINR in a multi-storey building to it in open space.

5.3 System Model

5.3.1 Assumptions

This chapter focuses on downlink transmissions and assumes impenetrable exterior walls, which means the signal power from outdoor environments is not considered for the UE in a

building. As shown in Fig. 5.1, in a K-storey building, the wireless transmit elements are assumed deployed on K parallel planes within the envelope of the building [119–122]. The assumptions of the network model are as follows.

Assumption 5.1. *The transmit elements are uniformly distributed with an infinitely large density in each storey of a multi-storey building. The transmit elements on the same floor are of the same height. All the transmit elements have the same transmit power and continuously operate at full power in the same frequency band.*

Assumption 5.2. *The probing UE is simultaneously served by the transmit elements sending detectable signals and considers the others sending undetectable signals as interferers. A signal is detectable for UE when its power received exceeds a threshold power level decided by the sensitivity of the receive device.*

Based on the assumptions, P_{T} [Wm^{-2}] is defined as the transmitted power per unit area and P_{th} [Wm^{-2}] is defined as the threshold power level of intended signals. As in [19–22], the assumptions enable the network model to represent future indoor wireless networks in a building under design with the basic network parameters, i.e., the transmit power density P_{T}, the receiver sensitivity P_{th}, and the carrier frequency f_{c} [Hz]. The BWP evaluation scheme is designed to quantify the impact of building structures on the maximum achievable network performance gain to reflect the intrinsic wireless performance of a building.

5.3.2 Intended signal power and interference power in multi-storey buildings

For the sake of simplicity, the building and individual rooms are assumed as cuboids with different dimensions and ignore the thickness of walls, floors, and ceilings [105, 139]. Consequently, as shown in Fig. 5.1, all the intra-room Tx-Rx links are LOS links, which reach the probing UE without the presence of walls, floors, or ceilings. Whereas, the inter-room and cross-floor Tx-Rx links are NLOS links. For the probing UE, the transmit elements located in the same room are referred to as the LOS transmit elements, while the others are referred to as the NLOS transmit elements. In a multi-storey building, the path gain is computed by a multi-slope model [140], as

$$G_s(R) = \begin{cases} 1, & R \leq \frac{\lambda}{4\pi}, \\ \left(\frac{\lambda}{4\pi}\right)^2 R^{-2}, & \frac{\lambda}{4\pi} < R \leq 1, \\ \left(\frac{\lambda}{4\pi}\right)^2 R^{-n_s}, & R > 1, \end{cases} \tag{5.4}$$

where R [m] is the length of the Tx-Rx link. The wavelength $\lambda = \frac{c}{f_c}$, where $c = 3 \times 10^8$ ms^{-1} denoting the speed of light. The subscript $s \in \{\mathrm{L}, \mathrm{N}\}$ representing the propagation scenario, where the event $\{s = \mathrm{L}\}$ denotes the LOS scenario and the event $\{s = \mathrm{N}\}$ denotes the NLOS scenario. The PLE n_s is decided by the characteristics of the propagation environment. The small-scale fading is ignored for simplicity.

Following the assumptions, the intended signal for probing UE in a given building satisfies the identity

$$P_{\mathrm{T}} G_s(R) > P_{\mathrm{th}}, \tag{5.5}$$

and the maximum Tx-Rx link length for an intended signal can be derived by solving the equation $P_{\mathrm{T}} G_s(R) = P_{\mathrm{th}}$, as

$$R_s = \left(\frac{P_{\mathrm{T}}}{P_{\mathrm{th}}}\right)^{\frac{1}{n_s}} \left(\frac{\lambda}{4\pi}\right)^{\frac{2}{n_s}}. \tag{5.6}$$

Note the method proposed in this chapter applies to the network system satisfying $R_s > 1$.

Without losing generality, the probing UE is assumed located on the k_0-th floor in a K-storey building. The height of the probing UE above the k_0-th floor is denoted by h_{R} [m], the height of the transmit elements above each floor is denoted by h_{T} [m], and the storey height is denoted by h_{F} [m]. A cylindrical coordinate system (r, θ, z) is used to denote the locations of the transmit elements, where the origin is set at the probing UE and the reference plane is parallel to the ground. Then the altitude of the transmit elements on the k-th floor is denoted by

$$H_k = h_{\mathrm{T}} - h_{\mathrm{R}} + h_{\mathrm{F}}(k - k_0), \tag{5.7}$$

where $k = 1, 2, \ldots, K$.

Fig. 5.2a shows the plane $z = H_{k_0}$, which contains both the LOS and NLOS transmit elements. Based on Assumption 1, the transmitted power from the transmit elements within a small region $\mathrm{d}\Omega$ is denoted by $P_{\mathrm{T}}\mathrm{d}\Omega$. The intended signal power and the interference power received from the k_0-th floor can be denoted by

$$P_{\mathrm{B},k_0} = \int_{\Omega_{P_{\mathrm{L}}}} P_{\mathrm{T}} G_{\mathrm{L}}(R)\mathrm{d}\Omega + \int_{\Omega_{P_{\mathrm{N}},k_0}} P_{\mathrm{T}} G_{\mathrm{N}}(R)\mathrm{d}\Omega, \tag{5.8}$$

and

$$I_{\mathrm{B},k_0} = \int_{\Omega_{I_{\mathrm{L}}}} P_{\mathrm{T}} G_{\mathrm{L}}(R)\mathrm{d}\Omega + \int_{\Omega_{I_{\mathrm{N}},k_0}} P_{\mathrm{T}} G_{\mathrm{N}}(R)\mathrm{d}\Omega, \tag{5.9}$$

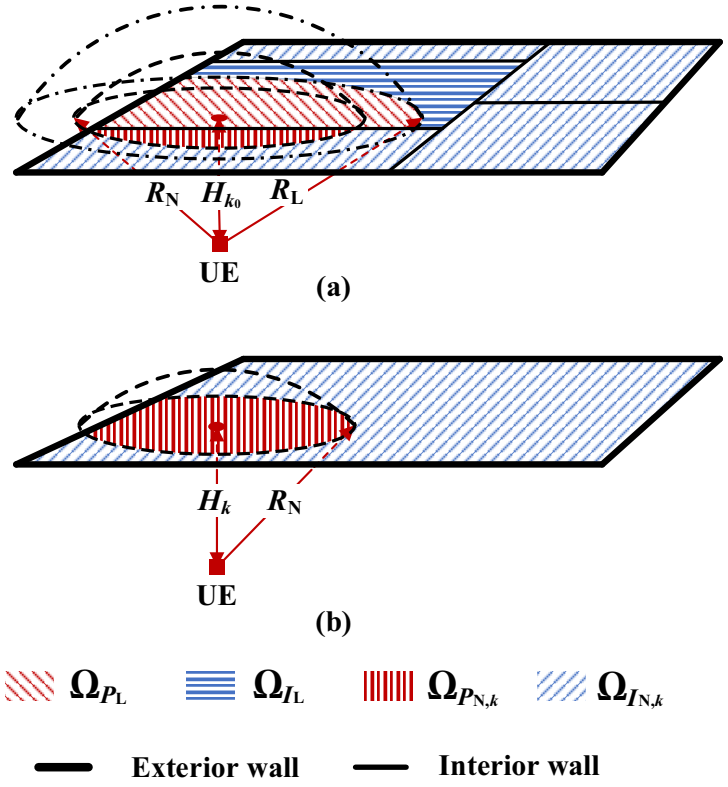

Fig. 5.2 The areas contain the transmit elements providing the intended signal power and the interference power in each storey. (a) Ω_{P_L}, $\Omega_{P_{N,k_0}}$, Ω_{I_L}, and $\Omega_{I_{N,k_0}}$ on the plane $z = H_{k_0}$. (b) $\Omega_{P_{N,k}}$ and $\Omega_{I_{N,k}}$ on the plane $z = H_k$ when $k \neq k_0$.

where Ω_{P_L} and Ω_{I_L} denote the areas containing the LOS transmit elements sending intended signals and interference, respectively, and $\Omega_{P_{N,k_0}}$ and $\Omega_{I_{N,k_0}}$ denote the areas on the plane $z = H_{k_0}$ containing the NLOS transmit elements sending intended signals and interference, respectively. Fig. 5.2b shows the plane $z = H_k$, which only contains the NLOS transmit elements when $k \neq k_0$. The intended signal power and the interference power received from the k-th ($k \neq k_0$) floor can be denoted by

$$P_{B,k} = \int_{\Omega_{P_{N,k}}} P_T G_N(R) d\Omega, \tag{5.10}$$

and

$$I_{B,k} = \int_{\Omega_{I_{N,k}}} P_T G_N(R) d\Omega, \tag{5.11}$$

where $\Omega_{P_{\mathrm{N}},k}$ and $\Omega_{I_{\mathrm{N}},k}$ denote the areas on the plane $z = H_k$ containing the NLOS transmit elements sending intended signals and interference, respectively. The detailed derivations of the closed-form expressions of $P_{\mathrm{B},k}$ and $I_{\mathrm{B},k}$ are given in Section 5.4.

5.3.3 Intended signal power and interference power in open space

To observe the impact of building structures, open space is used as the benchmark scenario, where no obstruction exists and the transmit elements are uniformly and infinitely densely deployed on the infinitely large plane $z = H_{k_0}$. The path gain model employed to compute the received signal strength in open space is given by [141]

$$G_{\mathrm{O}}(r) = \min\left\{1, \left(\frac{\lambda}{4\pi}\right)^2 r^{-2}, (h_{\mathrm{T}}h_{\mathrm{R}})^2 r^{-4}\right\}, \tag{5.12}$$

where r [m] is the 2-D link length, representing the length of the projection of a Tx-Rx link on the reference plane.

In open space, an intended signal to the probing UE satisfies the identity

$$P_{\mathrm{T}}G_{\mathrm{O}}(r) > P_{\mathrm{th}}. \tag{5.13}$$

Then the transmit elements providing intended signals are located in a circle with the radius r_{O} satisfying the relationship $P_{\mathrm{T}}G_{\mathrm{O}}(r_{\mathrm{O}}) = P_{\mathrm{th}}$, as

$$r_{\mathrm{O}} = \begin{cases} \frac{\lambda}{4\pi}\sqrt{\frac{P_{\mathrm{T}}}{P_{\mathrm{th}}}}, & \frac{\lambda}{4\pi}\sqrt{\frac{P_{\mathrm{T}}}{P_{\mathrm{th}}}} < r_{\mathrm{bp}}, \\ \sqrt{h_{\mathrm{T}}h_{\mathrm{R}}}\left(\frac{P_{\mathrm{T}}}{P_{\mathrm{th}}}\right)^{\frac{1}{4}}, & \frac{\lambda}{4\pi}\sqrt{\frac{P_{\mathrm{T}}}{P_{\mathrm{th}}}} \geq r_{\mathrm{bp}}, \end{cases} \tag{5.14}$$

where the break point distance

$$r_{\mathrm{bp}} = \frac{4\pi h_{\mathrm{T}}h_{\mathrm{R}}}{\lambda}. \tag{5.15}$$

The intended signal power and the interference power from transmit elements in open space can be computed by

$$P_{\mathrm{O}} = \int_0^{2\pi}\int_0^{r_{\mathrm{O}}} P_{\mathrm{T}}G_{\mathrm{O}}(r)\mathrm{d}\Omega, \tag{5.16}$$

and

$$I_{\mathrm{O}} = \int_0^{2\pi} \int_{r_{\mathrm{O}}}^{+\infty} P_{\mathrm{T}} G_{\mathrm{O}}(r) \mathrm{d}\Omega, \tag{5.17}$$

respectively. The closed-form expressions of P_{O} and I_{O} can be derived by inserting (5.12) and (5.14) into (5.16) and (5.17), as [20, Theorem 1]

$$P_{\mathrm{O}} = \begin{cases} \frac{P_{\mathrm{T}}\lambda^2}{16\pi}\left[1+\ln\left(\frac{P_{\mathrm{T}}}{P_{\mathrm{th}}}\right)\right], & \frac{\lambda}{4\pi}\sqrt{\frac{P_{\mathrm{T}}}{P_{\mathrm{th}}}} < r_{\mathrm{bp}}, \\ \frac{P_{\mathrm{T}}\lambda^2}{16\pi}\left[1+2\ln\left(\frac{16\pi^2 h_{\mathrm{T}} h_{\mathrm{R}}}{\lambda^2}\right)+\frac{\lambda^2}{32\pi^2(h_{\mathrm{T}}h_{\mathrm{R}})^2}\right]-\frac{\pi P_{\mathrm{th}}}{2}, & \frac{\lambda}{4\pi}\sqrt{\frac{P_{\mathrm{T}}}{P_{\mathrm{th}}}} \geq r_{\mathrm{bp}}, \end{cases} \tag{5.18}$$

and

$$I_{\mathrm{O}} = \begin{cases} \frac{P_{\mathrm{T}}\lambda^2}{16\pi}\left[1+2\ln\left(\frac{16\pi^2 h_{\mathrm{T}} h_{\mathrm{R}}}{\lambda^2}\right)+\ln\left(\frac{P_{\mathrm{th}}}{P_{\mathrm{T}}}\right)\right], & \frac{\lambda}{4\pi}\sqrt{\frac{P_{\mathrm{T}}}{P_{\mathrm{th}}}} < r_{\mathrm{bp}}, \\ \pi h_{\mathrm{T}} h_{\mathrm{R}} \sqrt{P_{\mathrm{T}} P_{\mathrm{th}}}, & \frac{\lambda}{4\pi}\sqrt{\frac{P_{\mathrm{T}}}{P_{\mathrm{th}}}} \geq r_{\mathrm{bp}}, \end{cases} \tag{5.19}$$

receptively.

5.4 Analytical Models

5.4.1 Definition of the TM

This section introduces the mathematical derivations of $P_{\mathrm{B},k}$ and $I_{\mathrm{B},k}$. As shown in Fig. 5.3, the projection of the probing UE and the interior/exterior walls define multiple triangles on the plane $z = H_k$. The triangular area confined by a wall and two rays from the projection of the probing UE is referred to as a TM. The analytical models to compute the intended signal power and the interference power from a typical TM are developed, and then applied to compute $P_{\mathrm{B},k}$ and $I_{\mathrm{B},k}$ in a multi-storey building. A typical TM from Fig. 5.3 is illustrated in Fig. 5.4.

As shown in Fig. 5.4, a cylindrical coordinate system (r, θ, z) is established for each TM, where the origin is set at the probing UE, the reference plane is parallel to the ground, and the 0-angle is defined on the direction perpendicular to the wall. Define H and D as the distances from the probing UE to the TM and the wall, respectively. θ_{l} and θ_{r} denote the angles of two ends of the projection of the wall on the reference plane, where $-\frac{\pi}{2} < \theta_{\mathrm{l}} < 0$ and $0 < \theta_{\mathrm{r}} < \frac{\pi}{2}$.

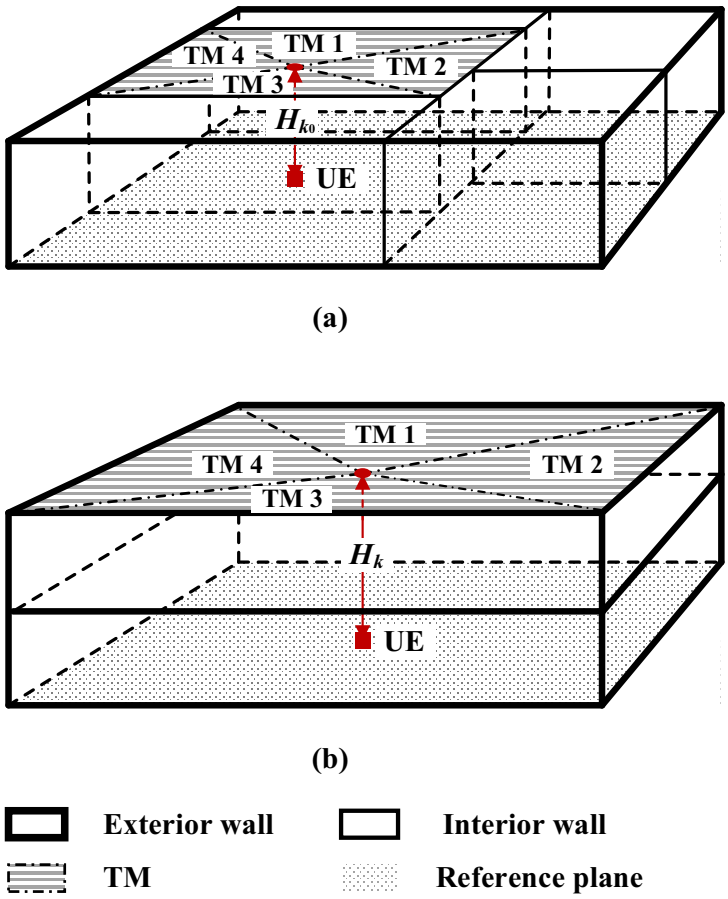

Fig. 5.3 TM division. (a) TM division for the room with the probing UE on the k_0-th floor. (b) TM division for the k-th floor.

5.4.2 Analytical models for a typical TM

The intended signal power and the interference power from the transmit elements in a typical TM with $s \in \{\mathrm{L}, \mathrm{N}\}$ can be denoted by

$$P_{\mathrm{TM}} = \int_{\Omega_{P_{\mathrm{TM}}}} P_{\mathrm{T}} G_s(R) \mathrm{d}\Omega, \tag{5.20}$$

and

$$I_{\mathrm{TM}} = \int_{\Omega_{I_{\mathrm{TM}}}} P_{\mathrm{T}} G_s(R) \mathrm{d}\Omega, \tag{5.21}$$

where $\Omega_{P_{\mathrm{TM}}}$ and $\Omega_{I_{\mathrm{TM}}}$ are the areas in the TM containing the transmit elements providing intended signal power and interference power, respectively. The analytical models of P_{TM}

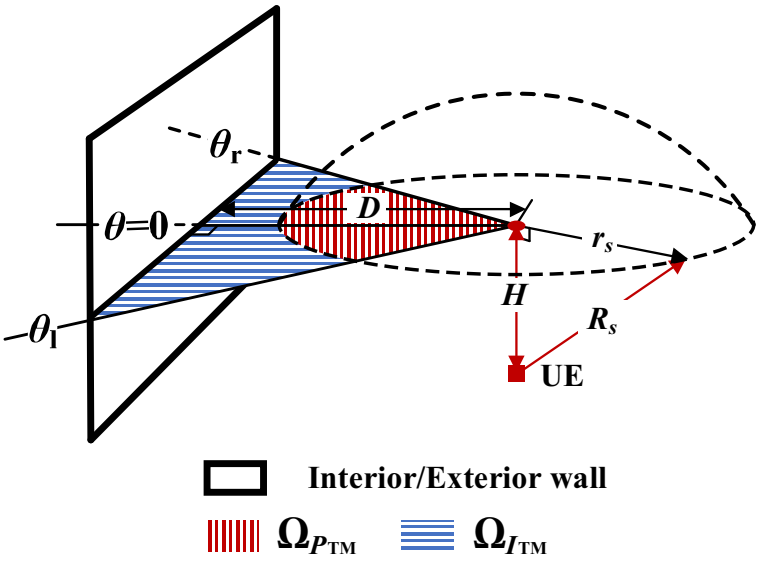

Fig. 5.4 A typical TM.

and I_{TM} are defined as

$$P_{\mathrm{TM}} = \mathscr{P}\left(P_{\mathrm{T}}, P_{\mathrm{th}}, \lambda, \theta_{\mathrm{l}}, \theta_{\mathrm{r}}, D, H, n_s\right), \tag{5.22}$$

and

$$I_{\mathrm{TM}} = \mathscr{I}\left(P_{\mathrm{T}}, P_{\mathrm{th}}, \lambda, \theta_{\mathrm{l}}, \theta_{\mathrm{r}}, D, H, n_s\right), \tag{5.23}$$

where the input parameters D, H, θ_{l} and θ_{r} are decided by the relative UE location, the PLE n_s depends on the characteristics of the propagation environment, and P_{T}, P_{th} and λ are basic network parameters. The closed-form expressions of $\mathscr{P}(\cdot)$ and $\mathscr{I}(\cdot)$ are given for a typical TM in Theorem 5.1.

Theorem 5.1. *The analytical models to compute the intended signal power and the interference power received by the probing UE from the transmit elements in a typical TM*

with $s \in \{\mathrm{L},\mathrm{N}\}$ *are given by*

$$\begin{aligned}\mathscr{P}\left(P_{\mathrm{T}},P_{\mathrm{th}},\lambda,\theta_{\mathrm{l}},\theta_{\mathrm{r}},D,H,n_s\right) =& P_{\mathrm{T}} r_{\mathrm{a}}^2 \frac{(\theta_{\mathrm{r}}-\theta_{\mathrm{l}})}{2} + P_{\mathrm{T}}\left(\frac{\lambda}{4\pi}\right)^2 \\ &\times \begin{bmatrix} \mathscr{H}_1\left(\theta_{\mathrm{l}},\theta_{\mathrm{r}},r_{\mathrm{a}},r_{\mathrm{b}},H,2\right) \\ +\mathscr{H}_2\left(\theta_{\mathrm{lb}},\theta_{\mathrm{rb}},r_{\mathrm{b}},D,H,2\right) \\ +\mathscr{H}_1\left(\theta_{\mathrm{l}},\theta_{\mathrm{r}},r_{\mathrm{b}},r_s,H,n_s\right) \\ +\mathscr{H}_2\left(\theta_{\mathrm{l}s},\theta_{\mathrm{r}s},r_s,D,H,n_s\right) \\ -\mathscr{H}_2\left(\theta_{\mathrm{lb}},\theta_{\mathrm{rb}},r_{\mathrm{b}},D,H,n_s\right) \end{bmatrix},\end{aligned} \tag{5.24}$$

and

$$\mathscr{I}\left(P_{\mathrm{T}},P_{\mathrm{th}},\lambda,\theta_{\mathrm{l}},\theta_{\mathrm{r}},D,H,n_s\right) = P_{\mathrm{T}}\left(\frac{\lambda}{4\pi}\right)^2 \begin{bmatrix} \mathscr{H}_2\left(\theta_{\mathrm{l}},\theta_{\mathrm{l}s},r_s,D,H,n_s\right) \\ +\mathscr{H}_2\left(\theta_{\mathrm{r}s},\theta_{\mathrm{r}},r_s,D,H,n_s\right) \end{bmatrix}, \tag{5.25}$$

where

$$r_{\mathrm{a}} = \mathrm{Re}\left\{\sqrt{\left(\frac{\lambda}{4\pi}\right)^2 - H^2}\right\}, \tag{5.26}$$

$$r_{\mathrm{b}} = \mathrm{Re}\left\{\sqrt{1-H^2}\right\}, \tag{5.27}$$

$$r_s = \mathrm{Re}\left\{\sqrt{{R_s}^2 - H^2}\right\}, \tag{5.28}$$

$$\theta_{\mathrm{lb}} = \max\left\{\theta_{\mathrm{l}}, -\arccos\left(\frac{D}{\max\{D,r_{\mathrm{b}}\}}\right)\right\}, \tag{5.29}$$

$$\theta_{\mathrm{rb}} = \min\left\{\theta_{\mathrm{r}}, \arccos\left(\frac{D}{\max\{D,r_{\mathrm{b}}\}}\right)\right\}, \tag{5.30}$$

$$\theta_{\mathrm{l}s} = \max\left\{\theta_{\mathrm{l}}, -\arccos\left(\frac{D}{\max\{D,r_s\}}\right)\right\}, \tag{5.31}$$

and

$$\theta_{rs} = \min\left\{\theta_{\mathrm{r}}, \arccos\left(\frac{D}{\max\{D, r_s\}}\right)\right\}, \tag{5.32}$$

where R_s is given in (5.6). The operator $\mathrm{Re}\{\cdot\}$ *denotes the real part of a complex number,* $\min\{\cdot\}$ *denotes the minimum value of the arguments, and* $\max\{\cdot\}$ *denotes the maximum value of the arguments. The functions $\mathscr{H}_1(\cdot)$ and $\mathscr{H}_2(\cdot)$ are given in the closed-form expressions for $-\frac{\pi}{2} < \theta_1 < 0$ and $0 < \theta_2 < \frac{\pi}{2}$, as*

$$\mathscr{H}_1(\theta_1, \theta_2, r_1, r_2, h, n) = \begin{cases} \frac{\theta_2 - \theta_1}{2-n}\left[\left({r_2}^2 + h^2\right)^{\frac{2-n}{2}} - \left({r_1}^2 + h^2\right)^{\frac{2-n}{2}}\right], & n \neq 2, \\ \frac{(\theta_2 - \theta_1)}{2} \ln\left(\frac{{r_2}^2 + h^2}{{r_1}^2 + h^2}\right), & n = 2, \end{cases} \tag{5.33}$$

and

$$\begin{aligned} &\mathscr{H}_2(\theta_1, \theta_2, r_1, d, h, n) \\ &= \begin{cases} \left\{ \begin{array}{l} \frac{(h^2+d^2)^{\frac{2-n}{2}}}{2-n} \\ \times \left[\begin{array}{l} \tan(\theta_2) F_1\left(\frac{1}{2}; \frac{n-2}{2}, 1; \frac{3}{2}; -\frac{d^2\tan^2(\theta_2)}{h^2+d^2}, -\tan^2(\theta_2)\right) \\ -\tan(\theta_1) F_1\left(\frac{1}{2}; \frac{n-2}{2}, 1; \frac{3}{2}; -\frac{d^2\tan^2(\theta_1)}{h^2+d^2}, -\tan^2(\theta_1)\right) \end{array}\right] \\ -\frac{(\theta_2-\theta_1)}{2-n}\left({r_1}^2 + h^2\right)^{\frac{2-n}{2}} \end{array} \right. , & n \neq 2, \\ \left\{ \begin{array}{l} \frac{1}{4}\,\mathrm{Im}\left\{ \begin{array}{l} \mathrm{Li}_2(-\frac{2d\sqrt{h^2+d^2}+2d^2+h^2}{h^2} e^{-2j\theta_2}) \\ -\mathrm{Li}_2(-\frac{2d\sqrt{h^2+d^2}+2d^2+h^2}{h^2} e^{-2j\theta_1}) \\ +\mathrm{Li}_2(\frac{2d\sqrt{h^2+d^2}-2d^2-h^2}{h^2} e^{-2j\theta_2}) \\ -\mathrm{Li}_2(\frac{2d\sqrt{h^2+d^2}-2d^2-h^2}{h^2} e^{-2j\theta_1}) \\ +2\mathrm{Li}_2(-e^{2j\theta_2}) - 2\mathrm{Li}_2(-e^{2j\theta_1}) \end{array} \right\} \\ +\frac{(\theta_2-\theta_1)}{2} \ln\left(\frac{h^2}{h^2+{r_1}^2}\right) \end{array} \right. , & n = 2, h \neq 0, \\ \frac{1}{2}\,\mathrm{Im}\left\{\mathrm{Li}_2\left(-e^{2j\theta_2}\right) - \mathrm{Li}_2\left(-e^{2j\theta_1}\right)\right\} + (\theta_2 - \theta_1)\ln\left(\frac{2d}{r_1}\right), & n = 2, h = 0, \end{cases} \end{aligned} \tag{5.34}$$

respectively, where $F_1(\cdot)$ denotes the Appell hypergeometric function, $\mathrm{Li}_2(\cdot)$ *denotes the dilogarithm function, and* $\mathrm{Im}\{\cdot\}$ *denotes the imaginary part of a complex number.*

Proof: A cylindrical coordinate system (r, θ, z) is established for a TM, where the origin is set at the probing UE, the reference plane is parallel to the ground, and the 0-angle is set to the line perpendicular to the wall, as shown in Fig. 5.4. For a Tx-Rx link with the length R and the propagation scenario s, the transmit element provides the intended signal if $R < R_s$; otherwise, it results in interference. The projection of R_s on the reference plane is denoted

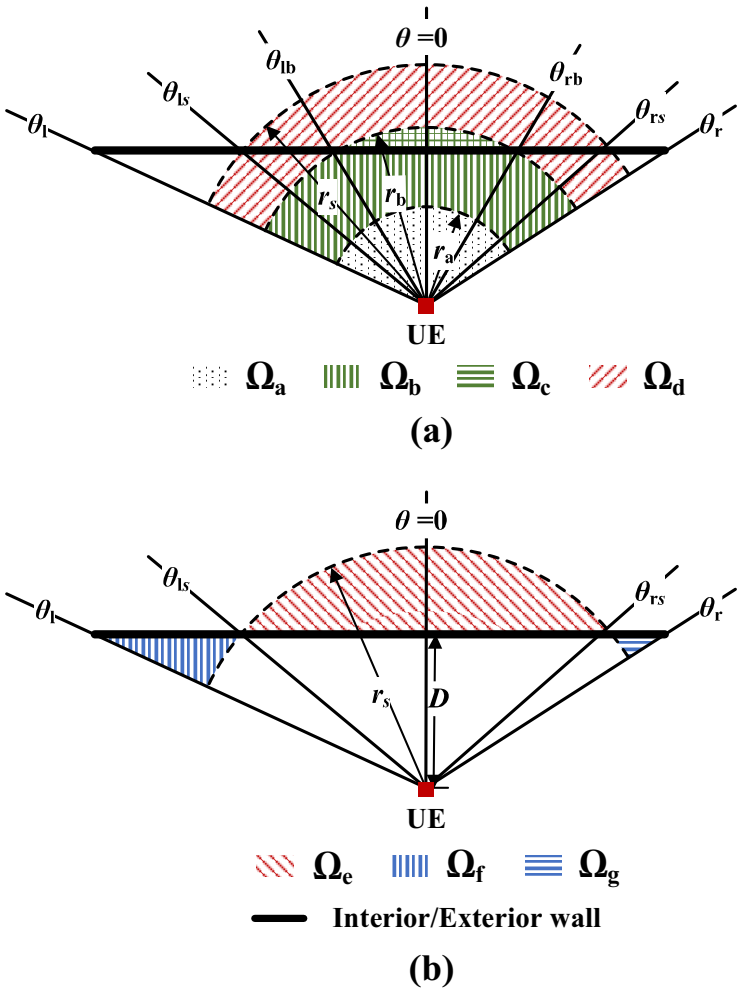

Fig. 5.5 The projection of a typical TM on the reference plane.

by r_s given in (5.28). Moreover, according to the multi-slope path gain model in (5.4), two corresponding break points exist at $R = \frac{\lambda}{4\pi}$ and $R = 1$, whose projections on the reference plane are denoted by r_{a} given in (5.26) and r_{b} given in (5.27), respectively.

Fig. 5.5 shows the projection of a typical TM on the reference plane, which can be divided into multiple regions by the arcs with the radius r_{a}, r_{b}, and r_s, as

$$\Omega_{\mathrm{a}} \triangleq \{(r,\theta,z) | (0 \le r \le r_{\mathrm{a}}) \wedge (\theta_{\mathrm{l}} < \theta < \theta_{\mathrm{r}}) \wedge (z = H)\}, \tag{5.35}$$

$$\Omega_{\mathrm{b}} \triangleq \{(r,\theta,z) | (r_{\mathrm{a}} < r \le r_{\mathrm{b}}) \wedge (\theta_{\mathrm{l}} < \theta < \theta_{\mathrm{r}}) \wedge (z = H)\}, \tag{5.36}$$

$$\Omega_{\rm c} \triangleq \left\{(r,\theta,z)\middle|\left(\frac{D}{\cos(\theta)} < r \le r_{\rm b}\right) \wedge (\theta_{\rm lb} \le \theta \le \theta_{\rm rb}) \wedge (z = H)\right\}, \tag{5.37}$$

$$\Omega_{\rm d} \triangleq \{(r,\theta,z)|\,(r_{\rm b} < r < r_s) \wedge (\theta_{\rm l} < \theta < \theta_{\rm r}) \wedge (z = H)\}, \tag{5.38}$$

$$\Omega_{\rm e} \triangleq \left\{(r,\theta,z)\middle|\left(\frac{D}{\cos(\theta)} < r < r_s\right) \wedge (\theta_{ls} < \theta < \theta_{rs}) \wedge (z = H)\right\}, \tag{5.39}$$

$$\Omega_{\rm f} \triangleq \left\{(r,\theta,z)\middle|\left(r_s \le r < \frac{D}{\cos(\theta)}\right) \wedge (\theta_{\rm l} < \theta \le \theta_{ls}) \wedge (z = H)\right\}, \tag{5.40}$$

and

$$\Omega_{\rm g} \triangleq \left\{(r,\theta,z)\middle|\left(r_s \le r < \frac{D}{\cos(\theta)}\right) \wedge (\theta_{rs} \le \theta < \theta_{\rm r}) \wedge (z = H)\right\}, \tag{5.41}$$

where $r_{\rm a} \le r_{\rm b} \le r_s$. $\theta_{\rm lb}$ and $\theta_{\rm rb}$ are the angles of the intersections of the arc with radius $r_{\rm b}$ and the wall, which are given in (5.29) and (5.30), respectively. θ_{ls} and θ_{rs} are the angle of the intersections of the arc with radius r_s and the wall, which are given in (5.31) and (5.32), respectively.

To simplify the expressions of the analytical models, for $n > 0$, $h \ge 0$, $-\pi \le \theta_1 \le \theta_2 \le \pi$ and $0 \le r_1 \le r_2$, define

$$\mathscr{H}_1(\theta_1,\theta_2,r_1,r_2,h,n) = \int_{\theta_1}^{\theta_2}\int_{r_1}^{r_2}\left(r^2+h^2\right)^{-\frac{n}{2}} r{\rm d}r{\rm d}\theta. \tag{5.42}$$

For $n > 0$, $h \ge 0$, $d > 0$, $-\frac{\pi}{2} < \theta_1 \le \theta_2 < \frac{\pi}{2}$ and $0 \le r_1 \le r_2$, define

$$\mathscr{H}_2(\theta_1,\theta_2,r_1,d,h,n) = \int_{\theta_1}^{\theta_2}\int_{r_1}^{\frac{d}{\cos(\theta)}}\left(r^2+h^2\right)^{-\frac{n}{2}} r{\rm d}r{\rm d}\theta. \tag{5.43}$$

$\mathscr{H}_1(\cdot)$ and $\mathscr{H}_2(\cdot)$ are given in closed-form expression by (5.33) and (5.34), respectively. The derivation of (5.33) is straightforward thereby omitted here. See Appendix B for the detailed derivations of (5.34).

For $0 < R < R_s$, the intended signal power from a typical TM can be computed by $\mathscr{P} = K_1 + K_2 + K_3$, where for $0 < R \le \frac{\lambda}{4\pi}$,

$$K_1 = \int_{\Omega_{\rm a}} P_{\rm T}{\rm d}\Omega = \int_{\theta_{\rm l}}^{\theta_{\rm r}}\int_0^{r_{\rm a}} P_{\rm T} r{\rm d}r{\rm d}\theta = P_{\rm T}\frac{\theta_{\rm r}-\theta_{\rm l}}{2}r_{\rm a}^2, \tag{5.44}$$

for $\frac{\lambda}{4\pi} < R \leq 1$,

$$\begin{aligned} K_2 =& \int_{\Omega_\mathrm{b}} P_\mathrm{T} \left(\frac{\lambda}{4\pi}\right)^2 R^{-2} \mathrm{d}\Omega - \int_{\Omega_\mathrm{c}} P_\mathrm{T} \left(\frac{\lambda}{4\pi}\right)^2 R^{-2} \mathrm{d}\Omega \\ =& \int_{\theta_\mathrm{l}}^{\theta_\mathrm{r}} \int_{r_\mathrm{a}}^{r_\mathrm{b}} P_\mathrm{T} \left(\frac{\lambda}{4\pi}\right)^2 \frac{r}{r^2+H^2} \mathrm{d}r\mathrm{d}\theta - \int_{\theta_\mathrm{lb}}^{\theta_\mathrm{rb}} \int_{\frac{D}{\cos(\theta)}}^{r_\mathrm{b}} P_\mathrm{T} \left(\frac{\lambda}{4\pi}\right)^2 \frac{r}{r^2+H^2} \mathrm{d}r\mathrm{d}\theta \\ =& P_\mathrm{T} \left(\frac{\lambda}{4\pi}\right)^2 \mathscr{H}_1\left(\theta_\mathrm{l}, \theta_\mathrm{r}, r_\mathrm{a}, r_\mathrm{b}, H, 2\right) + P_\mathrm{T} \left(\frac{\lambda}{4\pi}\right)^2 \mathscr{H}_2\left(\theta_\mathrm{lb}, \theta_\mathrm{rb}, r_\mathrm{b}, D, H, 2\right), \end{aligned} \tag{5.45}$$

and for $1 < R < R_s$,

$$\begin{aligned} K_3 =& \int_{\Omega_\mathrm{d}} P_\mathrm{T} \left(\frac{\lambda}{4\pi}\right)^2 R^{-n_s} \mathrm{d}\Omega - \int_{\Omega_\mathrm{e}} P_\mathrm{T} \left(\frac{\lambda}{4\pi}\right)^2 R^{-n_s} \mathrm{d}\Omega \\ &+ \int_{\Omega_\mathrm{c}} P_\mathrm{T} \left(\frac{\lambda}{4\pi}\right)^2 R^{-n_s} \mathrm{d}\Omega \\ =& \int_{\theta_\mathrm{l}}^{\theta_\mathrm{r}} \int_{r_\mathrm{b}}^{r_s} P_\mathrm{T} \left(\frac{\lambda}{4\pi}\right)^2 \left(r^2+H^2\right)^{-\frac{n_s}{2}} r\mathrm{d}r\mathrm{d}\theta \\ &- \int_{\theta_{\mathrm{l}s}}^{\theta_{\mathrm{r}s}} \int_{\frac{D}{\cos(\theta)}}^{r_s} P_\mathrm{T} \left(\frac{\lambda}{4\pi}\right)^2 \left(r^2+H^2\right)^{-\frac{n_s}{2}} r\mathrm{d}r\mathrm{d}\theta \\ &+ \int_{\theta_\mathrm{lb}}^{\theta_\mathrm{rb}} \int_{\frac{D}{\cos(\theta)}}^{r_\mathrm{b}} P_\mathrm{T} \left(\frac{\lambda}{4\pi}\right)^2 \left(r^2+H^2\right)^{-\frac{n_s}{2}} r\mathrm{d}r\mathrm{d}\theta \\ =& P_\mathrm{T} \left(\frac{\lambda}{4\pi}\right)^2 \mathscr{H}_1\left(\theta_\mathrm{l}, \theta_\mathrm{r}, r_\mathrm{b}, r_s, H, n_s\right) \\ &+ P_\mathrm{T} \left(\frac{\lambda}{4\pi}\right)^2 \mathscr{H}_2\left(\theta_{\mathrm{l}s}, \theta_{\mathrm{r}s}, r_s, D, H, n_s\right) \\ &- P_\mathrm{T} \left(\frac{\lambda}{4\pi}\right)^2 \mathscr{H}_2\left(\theta_\mathrm{lb}, \theta_\mathrm{rb}, r_\mathrm{b}, D, H, n_s\right). \end{aligned} \tag{5.46}$$

For $R \geq R_s$, the interference power from a typical TM can be computed by $\mathscr{I} = K_4$, where

$$\begin{aligned} K_4 &= \int_{\Omega_{\mathrm{f}}} P_{\mathrm{T}} \left(\frac{\lambda}{4\pi}\right)^2 R^{-n_s} \mathrm{d}\Omega + \int_{\Omega_{\mathrm{g}}} P_{\mathrm{T}} \left(\frac{\lambda}{4\pi}\right)^2 R^{-n_s} \mathrm{d}\Omega \\ &= \int_{\theta_{\mathrm{l}}}^{\theta_{\mathrm{ls}}} \int_{r_s}^{\frac{D}{\cos(\theta)}} P_{\mathrm{T}} \left(\frac{\lambda}{4\pi}\right)^2 \left(r^2 + H^2\right)^{-\frac{n_s}{2}} r \mathrm{d}r\mathrm{d}\theta \\ &\quad + \int_{\theta_{\mathrm{rs}}}^{\theta_{\mathrm{r}}} \int_{r_s}^{\frac{D}{\cos(\theta)}} P_{\mathrm{T}} \left(\frac{\lambda}{4\pi}\right)^2 \left(r^2 + H^2\right)^{-\frac{n_s}{2}} r \mathrm{d}r\mathrm{d}\theta \\ &= P_{\mathrm{T}} \left(\frac{\lambda}{4\pi}\right)^2 \mathscr{H}_2 \left(\theta_{\mathrm{l}}, \theta_{\mathrm{ls}}, r_s, D, H, n_s\right) \\ &\quad + P_{\mathrm{T}} \left(\frac{\lambda}{4\pi}\right)^2 \mathscr{H}_2 \left(\theta_{\mathrm{rs}}, \theta_{\mathrm{r}}, r_s, D, H, n_s\right). \end{aligned} \tag{5.47}$$

Define (5.22) and (5.23) as functions with the input parameters P_{T}, P_{th}, λ, n_s, θ_{l}, θ_{r}, D, and H. Then $\mathscr{P}(\cdot)$ and $\mathscr{I}(\cdot)$ defined in Theorem 5.1 can be extended to computed the intended signal power and the interference power in a multi-storey building. ■

5.4.3 Closed-form $P_{\mathrm{B},k}$ and $I_{\mathrm{B},k}$

Based on Theorem 5.1, P_{B,k_0} and I_{B,k_0} can be obtained by Lemma 5.1, while $P_{\mathrm{B},k}$ and $I_{\mathrm{B},k}$ with $k \neq k_0$ can be obtained by Lemma 5.2 given in the following.

Lemma 5.3. *The intended signal power and the interference power received by the probing UE from the transmit elements on the k_0-th floor are computed by*

$$\begin{aligned} P_{\mathrm{B},k_0} &= \sum_{m=1}^{M_{k_0}} \mathscr{P}\left(P_{\mathrm{T}}, P_{\mathrm{th}}, \lambda, \theta_{\mathrm{l},k_0,m}, \theta_{\mathrm{r},k_0,m}, D_{k_0,m}, H_{k_0}, n_{\mathrm{N}}\right) \\ &\quad + \sum_{m'=1}^{M_0} \begin{bmatrix} \mathscr{P}\left(P_{\mathrm{T}}, P_{\mathrm{th}}, \lambda, \theta_{\mathrm{l},0,m'}, \theta_{\mathrm{r},0,m'}, D_{0,m'}, H_{k_0}, n_{\mathrm{L}}\right) \\ -\mathscr{P}\left(P_{\mathrm{T}}, P_{\mathrm{th}}, \lambda, \theta_{\mathrm{l},0,m'}, \theta_{\mathrm{r},0,m'}, D_{0,m'}, H_{k_0}, n_{\mathrm{N}}\right) \end{bmatrix}, \end{aligned} \tag{5.48}$$

and

$$\begin{aligned} I_{\mathrm{B},k_0} &= \sum_{m=1}^{M_{k_0}} \mathscr{I}\left(P_{\mathrm{T}}, P_{\mathrm{th}}, \lambda, \theta_{\mathrm{l},k_0,m}, \theta_{\mathrm{r},k_0,m}, D_{k_0,m}, H_{k_0}, n_{\mathrm{N}}\right) \\ &\quad + \sum_{m'=1}^{M_0} \begin{bmatrix} \mathscr{I}\left(P_{\mathrm{T}}, P_{\mathrm{th}}, \lambda, \theta_{\mathrm{l},0,m'}, \theta_{\mathrm{r},0,m'}, D_{0,m'}, H_{k_0}, n_{\mathrm{L}}\right) \\ -\mathscr{I}\left(P_{\mathrm{T}}, P_{\mathrm{th}}, \lambda, \theta_{\mathrm{l},0,m'}, \theta_{\mathrm{r},0,m'}, D_{0,m'}, H_{k_0}, n_{\mathrm{N}}\right) \end{bmatrix}, \end{aligned} \tag{5.49}$$

respectively, where M_0 and M_{k_0} refer to the number of the TMs making up the room with the probing UE and the k_0-th floor, respectively. The altitude of the transmit elements on the k_0-th floor is denoted by H_{k_0}. For the m'-th TM in the room with the probing UE, $\theta_{\mathrm{l},0,m'}$ and $\theta_{\mathrm{r},0,m'}$ denote the angles of two ends of the projection of the m'-th wall on the reference plane; $D_{0,m'}$ denotes the distance from the probing UE to the m'-th wall. For the m-th TM making up the k_0-th floor, $\theta_{\mathrm{l},k_0,m}$ and $\theta_{\mathrm{r},k_0,m}$ denote the angles of two ends of the projection of the m-th exterior wall on the reference plane; $D_{k_0,m}$ denotes the distance from the probing UE to the m-th external wall.

Proof: As shown in Fig. 5.2, both the LOS and NLOS transmit elements exist on the k_0-th floor. The total intended signal power received from the k_0-th floor is given in (5.8), where the first and second terms denote the intended signal power received from the LOS transmit elements and NLOS transmit elements on the k_0-th floor, respectively.

As shown in Fig. 5.3a, a rectangular room can be divided into 4 TMs, i.e., $M_0 = 4$. The total LOS intended signal power is the sum of LOS intended signal power in the TMs. Then the first term in (5.8) can be computed by

$$\sum_{m'=1}^{M_0} \mathscr{P}\left(P_{\mathrm{T}}, P_{\mathrm{th}}, \lambda, \theta_{\mathrm{l},0,m'}, \theta_{\mathrm{r},0,m'}, D_{0,m'}, H_{k_0}, n_{\mathrm{L}}\right), \tag{5.50}$$

where $\theta_{\mathrm{l},0,m'}$ and $\theta_{\mathrm{r},0,m'}$ are the angles of the m'-th TM and $D_{0,m'}$ is the distance from UE to the m'-th wall of the room. H_{k_0} is the height difference between the probing UE and the transmit elements on the k_0-th floor.

As shown in Fig. 5.2, the room with the probing UE blocks a part of NLOS intended signals. The k_0-th floor can also be divided into 4 TMs, i.e., $M_{k_0} = 4$. The total NLOS intended signal power from the k_0-th floor is derived by summing up intended signal power from the TMs of the k_0-th floor and discarding the intended signal power blocked by the room with the probing UE. Then the second term in (5.8) can be computed by

$$\begin{aligned}&\sum_{m=1}^{M_{k_0}} \mathscr{P}\left(P_{\mathrm{T}}, P_{\mathrm{th}}, \lambda, \theta_{\mathrm{l},k_0,m}, \theta_{\mathrm{r},k_0,m}, D_{k_0,m}, H_{k_0}, n_{\mathrm{N}}\right)\\ &- \sum_{m'=1}^{M_0} \mathscr{P}\left(P_{\mathrm{T}}, P_{\mathrm{th}}, \lambda, \theta_{\mathrm{l},0,m'}, \theta_{\mathrm{r},0,m'}, D_{0,m'}, H_{k_0}, n_{\mathrm{N}}\right),\end{aligned} \tag{5.51}$$

where $\theta_{\mathrm{l},k_0,m}$ and $\theta_{\mathrm{r},k_0,m}$ are the angles of the m-th TM of the k_0-th floor and $D_{k_0,m}$ is the distance from the probing UE to the m-th exterior wall of the building. Inserting (5.50) and (5.51) into (5.8), the closed-form expression of P_{B,k_0} given in (5.48) can be derived.

Similarly, the total interference power for probing UE received from the transmit elements on the k_0-th floor is given in (5.9), where the first term denoting interference power received from the LOS transmit elements can be computed by

$$\sum_{m'=1}^{M_0} \mathscr{I}\left(P_{\mathrm{T}}, P_{\mathrm{th}}, \lambda, \theta_{\mathrm{l},0,m'}, \theta_{\mathrm{r},0,m'}, D_{0,m'}, H_{k_0}, n_{\mathrm{L}}\right), \tag{5.52}$$

and the second term denoting interference power received from the NLOS transmit elements can be computed by

$$\begin{aligned} &\sum_{m=1}^{M_{k_0}} \mathscr{I}\left(P_{\mathrm{T}}, P_{\mathrm{th}}, \lambda, \theta_{\mathrm{l},k_0,m}, \theta_{\mathrm{r},k_0,m}, D_{k_0,m}, H_{k_0}, n_{\mathrm{N}}\right) \\ &- \sum_{m'=1}^{M_0} \mathscr{I}\left(P_{\mathrm{T}}, P_{\mathrm{th}}, \lambda, \theta_{\mathrm{l},0,m'}, \theta_{\mathrm{r},0,m'}, D_{0,m'}, H_{k_0}, n_{\mathrm{N}}\right). \end{aligned} \tag{5.53}$$

Inserting (5.52) and (5.53) into (5.9), the closed-form expression of I_{B,k_0} given in (5.49) can be derived. ■

Lemma 5.4. *The intended signal power and the interference power received by the probing UE from the transmit elements on the k-th ($k \neq k_0$) floor are computed by*

$$P_{\mathrm{B},k} = \sum_{m=1}^{M_k} \mathscr{P}\left(P_{\mathrm{T}}, P_{\mathrm{th}}, \lambda, \theta_{\mathrm{l},k,m}, \theta_{\mathrm{r},k,m}, D_{k,m}, H_k, n_{\mathrm{N}}\right), \tag{5.54}$$

and

$$I_{\mathrm{B},k} = \sum_{m=1}^{M_k} \mathscr{I}\left(P_{\mathrm{T}}, P_{\mathrm{th}}, \lambda, \theta_{\mathrm{l},k,m}, \theta_{\mathrm{r},k,m}, D_{k,m}, H_k, n_{\mathrm{N}}\right), \tag{5.55}$$

respectively, where M_k refers to the number of the TMs making up the k-th floor. The altitude of the transmit elements on the k-th floor is denoted by H_k. For the m-th TM, $\theta_{\mathrm{l},k,m}$ and $\theta_{\mathrm{r},k,m}$ denote the angles of two ends of the projection of the m-th exterior wall on the reference plane; $D_{k,m}$ denotes the distance from the probing UE to the m-th exterior wall.

Proof: As shown in Fig. 5.3b, when $k \neq k_0$, $P_{\mathrm{B},k}$ and $I_{\mathrm{B},k}$ are the sums of intended signal power and interference power from all the TMs making up the k-th floor, respectively. ■

With the closed-form expressions of P_{O}, I_{O}, $P_{\mathrm{B},k}$ and $I_{\mathrm{B},k}$, g_{P} and g_{I} can be obtained for a probing UE location in a given building by substituting (5.18), (5.48) and (5.54) into (5.2) and substituting (5.19), (5.49) and (5.55) into (5.3), respectively.

5.5 Numerical Results

5.5.1 Validations of analytical models in a typical TM

Fig. 5.6 shows the received intended signal power and the interference power from a typical TM illustrated in Fig. 5.4, i.e., P_{TM} and I_{TM}, vary with the input parameters of (5.22) and (5.23), including the probing UE location, i.e., θ_{r}, D and H, PLEs, i.e., n_s, and basic network parameters, i.e., P_{th} and f_{c}. Without specifying in the figures, the parameters $D = 5$ m, $H = 2$ m, $\theta_{\mathrm{l}} = -\frac{\pi}{3}$, $\theta_{\mathrm{r}} = \frac{\pi}{3}$, $n_s = 3.19$, $P_{\mathrm{T}} = -30$ dBWm^{-2}, and $P_{\mathrm{th}} = -90$ dBWm^{-2}. The

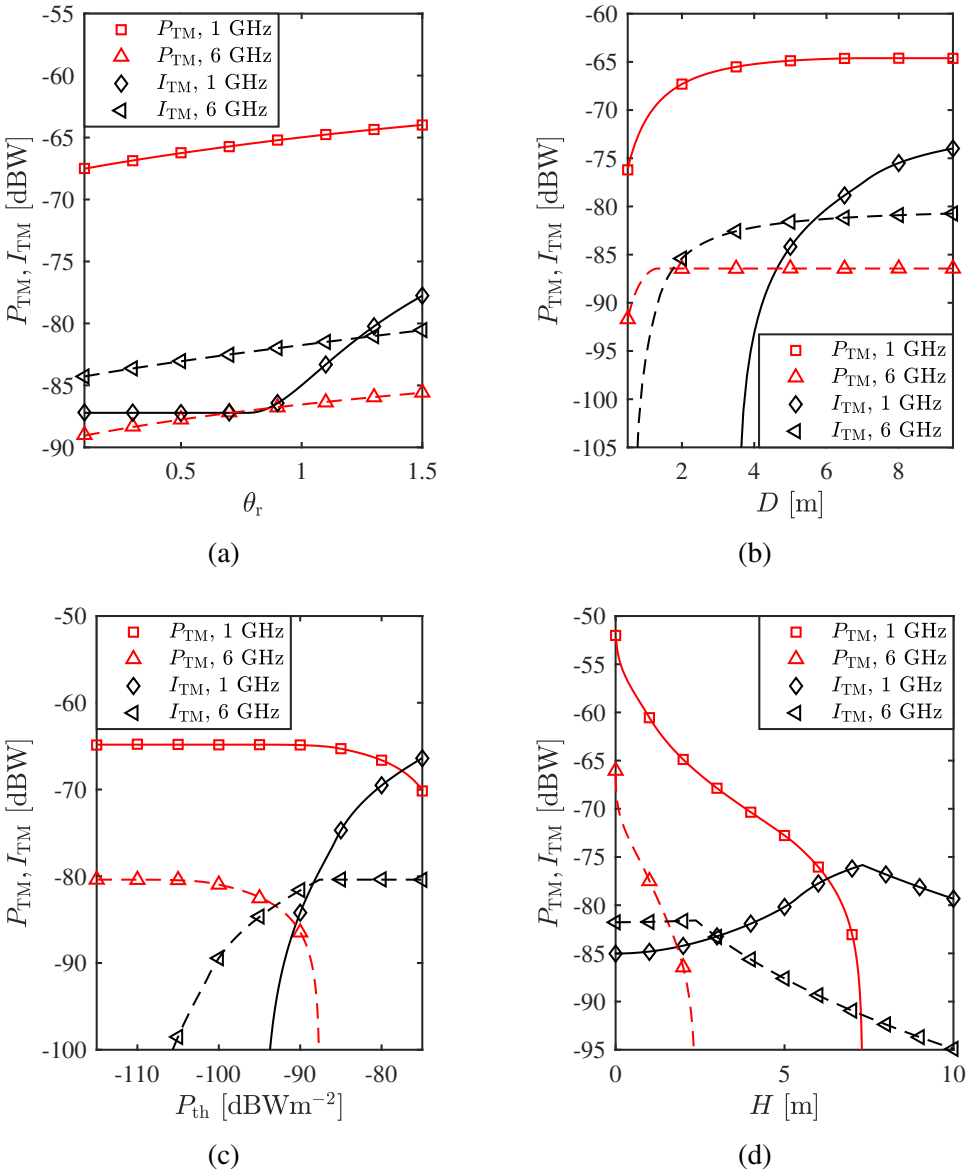

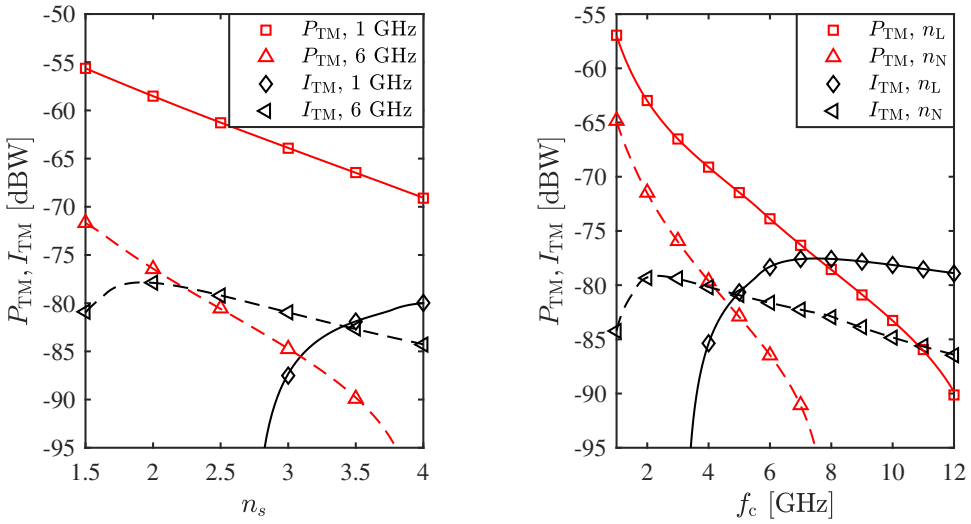

(e) (f)

Fig. 5.6 P_{TM} and I_{TM} vary with the input parameters of Theorem 5.1. The lines are generated by the analytical models while the markers are the results of the Monte Carlo simulations.

lines are generated by the analytical models proposed in Theorem 5.1, and the markers are the results of the Monte Carlo simulations, which match the lines well.

As shown in Fig. 5.6, P_{TM} and I_{TM} vary in different trends with these parameters. In Fig. 5.6a-b, P_{TM} and I_{TM} either remain constant or increase since the area of the TM increases as θ_{r} or D enlarges. In Fig. 5.6c, P_{TM} reduces while I_{TM} enhances as P_{th} rises because higher P_{th} results in shorter R_s and hence a smaller area of $\Omega_{P_{\mathrm{TM}}}$ and a larger area of $\Omega_{I_{\mathrm{TM}}}$. In Fig. 5.6d-f, P_{TM} drops as n_s, H, or f_{c} increases since Tx-Rx links from the TM suffer a more severe distance-dependent decay resulting in the intended signals weakened and partially turning to interference. Whereas I_{TM} fluctuates because the enlargement of $\Omega_{I_{\mathrm{TM}}}$ cancels out the reduction of the received interference power from each Tx-Rx link.

5.5.2 Validations of analytical models in a typical office building

The analytical models are then validated by the Monte Carlo simulations in a typical office building. Fig. 5.7 shows the 2-D floor plan of each storey, which consists of forty 10 m$\times$10 m rooms and two 100 m$\times$5 m corridors, as described by the WINNER II A1 scenario [32]. In the rest of this chapter, the PLEs $n_{\mathrm{L}} = 1.73$ and $n_{\mathrm{N}} = 3.19$ [102]. The transmit elements are assumed mounted on the ceiling of each storey, i.e., $h_{\mathrm{T}} = h_{\mathrm{F}}$. UE A marked in Fig. 5.7 is located in the centre of the square room and with the height $h_{\mathrm{R}} = 1$ m. The Monte Carlo simulations adopt the PPP with a high intensity of 0.1 m^{-2} to represent the transmit elements

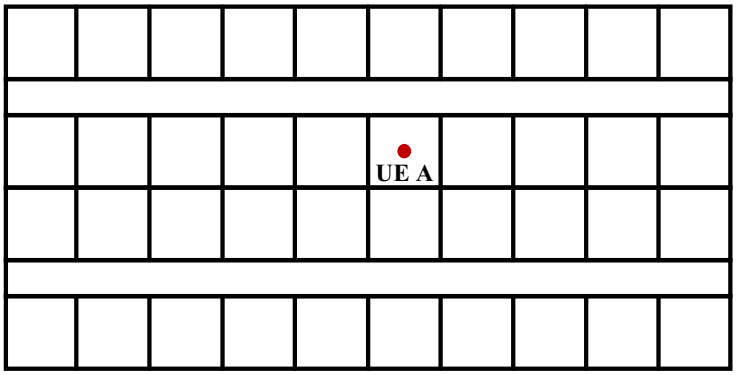

Fig. 5.7 The 2-D floor plan of a typical indoor office scenario, the WINNER II A1 scenario.

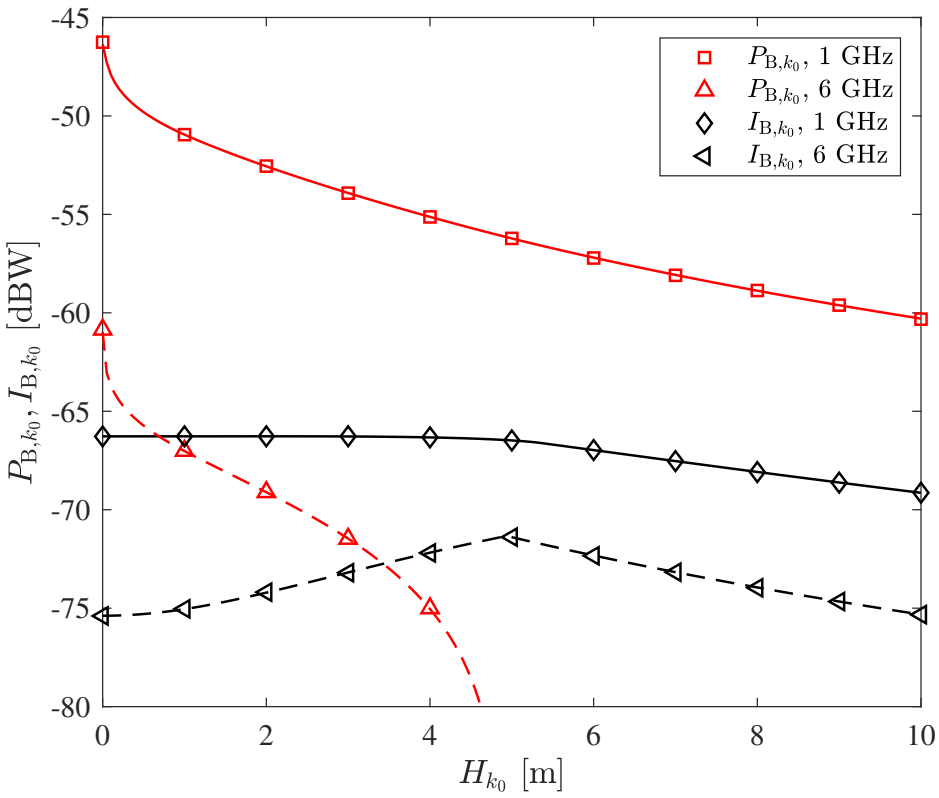

Fig. 5.8 P_{k_0} and I_{k_0} for UE A vary with H_{k_0}. The lines are generated by the analytical models while the markers are the results of the Monte Carlo simulations. The results are generated assuming $P_{\mathrm{T}} = -30$ dBWm^{-2} and $P_{\mathrm{th}} = -90$ dBWm^{-2}.

of the assumed network model in each storey. The received signal power is computed by (5.4) and the intended signals and interference are distinguished by the link length R_s given

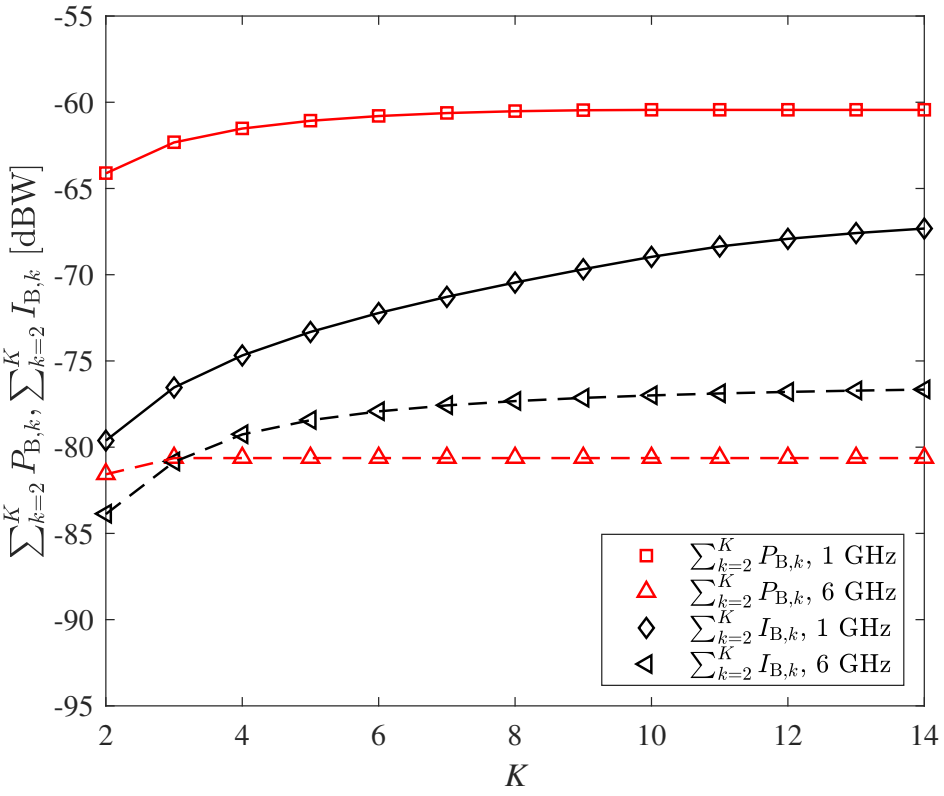

Fig. 5.9 $\sum_{k=2}^{K} P_{\mathrm{B},k}$ and $\sum_{k=2}^{K} I_{\mathrm{B},k}$ for UE A on the first floor ($k_0 = 1$) vary with K. The lines are generated by the analytical models while the markers are the results of the Monte Carlo simulations. The results are generated with $P_{\mathrm{T}} = -30$ dBWm^{-2} and $P_{\mathrm{th}} = -110$ dBWm^{-2}.

by (5.6). The simulation results are the average of 10^4 realisations. UE A is taken as an example to explore how the intended signal power and the interference power vary with the number of storeys and their height in the 1-GHz and 6-GHz bands. The numerical results are generated based on Lemma 5.1 and Lemma 5.2 and illustrated in Fig. 5.8 and Fig. 5.9, respectively, which show good agreements with the Monte Carlo simulations.

Fig. 5.8 shows the variations of P_{k_0} and I_{k_0} with the height difference between UE A and the transmit elements, i.e., H_{k_0}. The results are generated assuming $P_{\mathrm{T}} = -30$ dBWm^{-2} and $P_{\mathrm{th}} = -90$ dBWm^{-2}. Similar to Fig. 5.6d, P_{B,k_0} drops while I_{B,k_0} fluctuates at both 1 GHz and 6 GHz as H_{k_0} increases. As P_{B,k_0} and I_{B,k_0} composed of both LOS and NLOS signal power are affected by the layout of the building, their variations are not the same as P_{TM} and I_{TM} of a single TM in Fig. 5.6d.

Fig. 5.9 shows that the total cross-floor intended signal power and the total cross-floor interference power received by UE A on the first floor, i.e., $\sum_{k=2}^{K} P_{\mathrm{B},k}$ and $\sum_{k=2}^{K} I_{\mathrm{B},k}$, vary with the number of storeys K. The results are generated with $P_{\mathrm{T}} = -30$ dBWm^{-2}, $P_{\mathrm{th}} =$

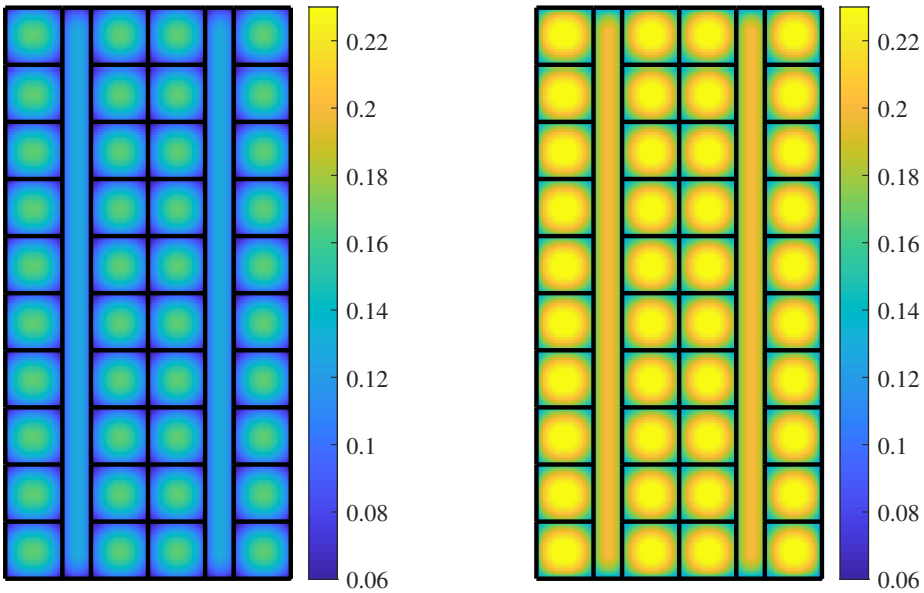

(a) g_{P}, $k_0 = 1$ (b) g_{P}, $k_0 = 3$

Fig. 5.10 g_{P} in a 5-storey building with a WINNER II A1 layout at 6 GHz.

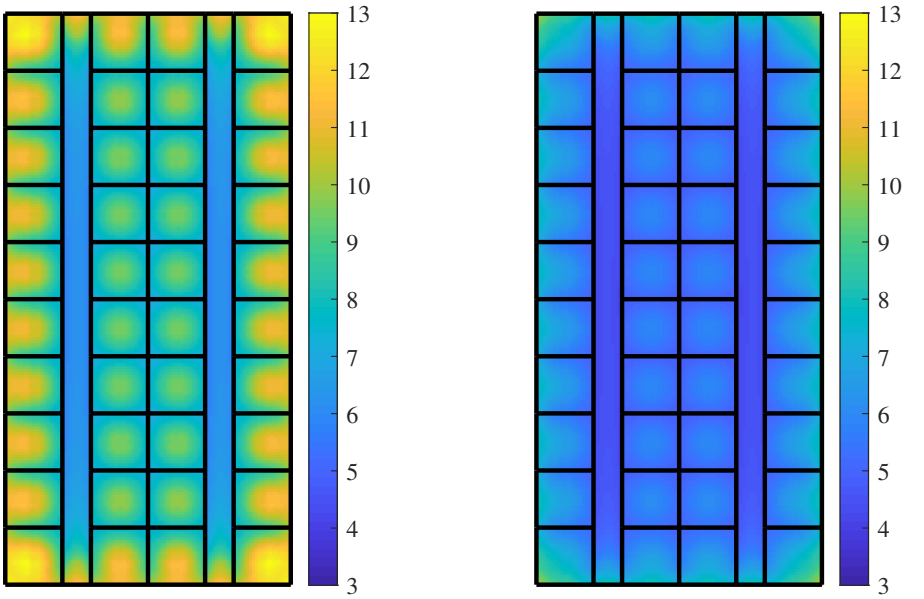

(a) g_{I}, $k_0 = 1$ (b) g_{I}, $k_0 = 3$

Fig. 5.11 g_{I} in a 5-storey building with a WINNER II A1 layout at 6 GHz.

-110 dBWm^{-2}, and $h_{\mathrm{T}} = h_{\mathrm{F}} = 3$ m. Then there are that $R_{\mathrm{N}} = 30.96$ m at 1 GHz and $R_{\mathrm{N}} = 10.07$ m at 6 GHz. As shown in Fig. 5.9, $\sum_{k=2}^{K} P_{\mathrm{B},k}$ stops rising when $K > 10$ at 1 GHz

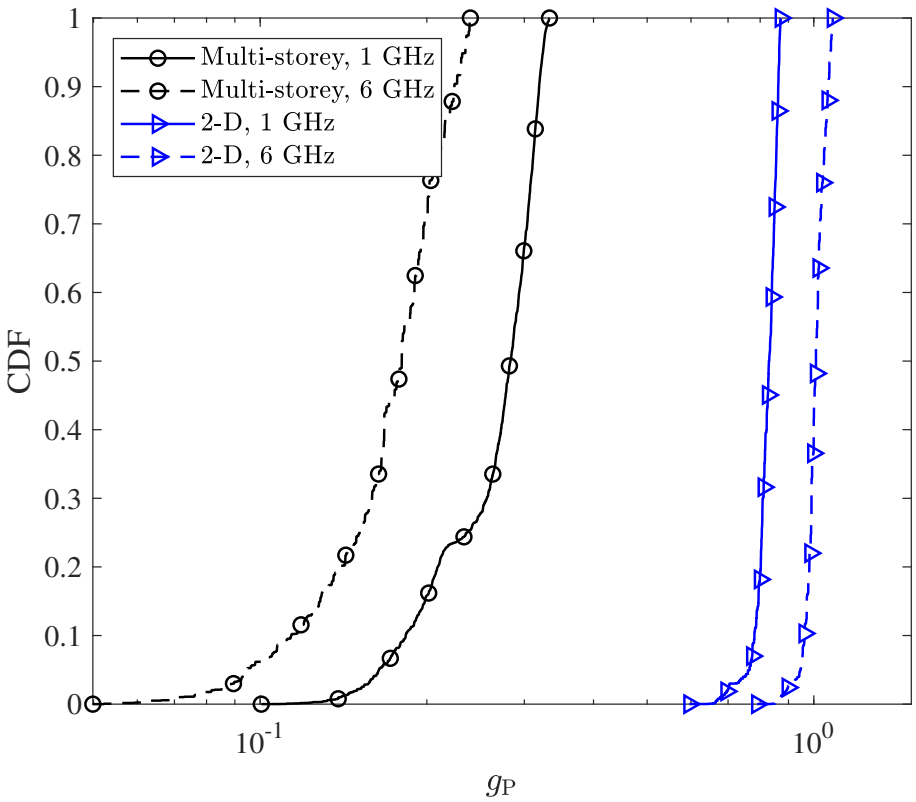

Fig. 5.12 The CDFs of g_{P} in a 5-storey building with a WINNER II A1 layout.

and when $K > 3$ at 6 GHz since $P_{\mathrm{B},K} = 0$ if $H_K \geq R_{\mathrm{N}}$. Despite the increase of $\sum_{k=2}^{K} I_{\mathrm{B},k}$, $I_{\mathrm{B},K}$ drops significantly as K increases. Therefore, two storeys with a large separation have a limited impact on each other in terms of the BWP.

5.5.3 BWP of a typical office building

The BWP evaluation is demonstrated for a 5-storey building with a WINNER II A1 layout in this section. Given $P_{\mathrm{T}} = -30$ dBWm^{-2}, $P_{\mathrm{th}} = -90$ dBWm^{-2}, $\sigma^2 = -98$ dBm, $h_{\mathrm{R}} = 1$ m, and $h_{\mathrm{T}} = h_{\mathrm{F}} = 3$ m, g_{I} and g_{P} are obtained for uniformly distributed probing UE locations in all the storeys of the building at 1 GHz and 6 GHz.

Fig. 5.10 shows the distributions of g_{P} on the first and the third floors at 6 GHz. With the assumed parameters, $R_{\mathrm{L}} = 4.94$ m and $R_{\mathrm{N}} = 2.38$ m at 6 GHz. The PG g_{P} is lower near the edges of the square rooms since the LOS intended signals are partially blocked when the distance from the probing UE to a wall is shorter than R_{L}. Moreover, the third floor has a higher g_{P} than the first. The transmit elements in the second floor are 4 m and 1 m apart from

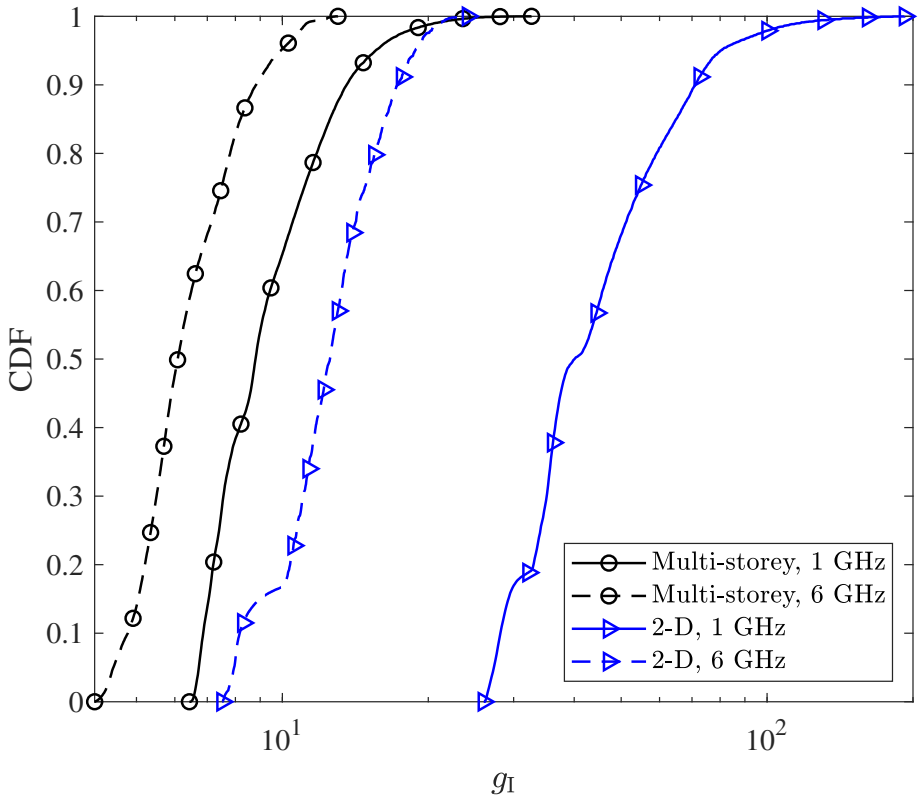

Fig. 5.13 The CDFs of g_{I} in a 5-storey building with a WINNER II A1 layout.

the probing UE on the first floor and the third floor, respectively. Since $1 < R_{\mathrm{N}}$, the probing UE on the third floor can receive extra NLOS intended signal power from the second floor.

Fig. 5.11 shows the distributions of g_{I} on the first and the third floors at 6 GHz. The IG g_{I} is much lower in the corridors than it in the square rooms since the long corridor induces more strong LOS interference power. In the centre rooms of each storey, g_{I} is higher in the centre of the rooms since the interior walls block the LOS interference and also keep the probing UE a distance from the NLOS interferers in other rooms. In the rooms on building edges, g_{I} is higher near the exterior walls since the interference outside the building is blocked. In contrast to g_{P}, g_{I} is lower on the third floor than it on the first since the UE on the third floor suffers stronger cross-floor interference.

Fig. 5.12-5.13 show the CDFs of g_{P} and g_{I} in the 5-storey office building at 1 GHz and 6 GHz. The CDFs obtained by the proposed multi-storey BWP evaluation scheme show that the 1-GHz band agrees with the 5-storey office building more than the 6-GHz band in terms of both g_{P} and g_{I}. As given by $\gamma_{\mathrm{B}} = g_{\mathrm{P}} g_{\mathrm{I}} \gamma_{\mathrm{O}}$, $g_{\mathrm{P}} g_{\mathrm{I}}$ represents the ratio of the SINR in the multi-storey building to it in open space. As shown in Fig. 5.14, the typical 5-storey

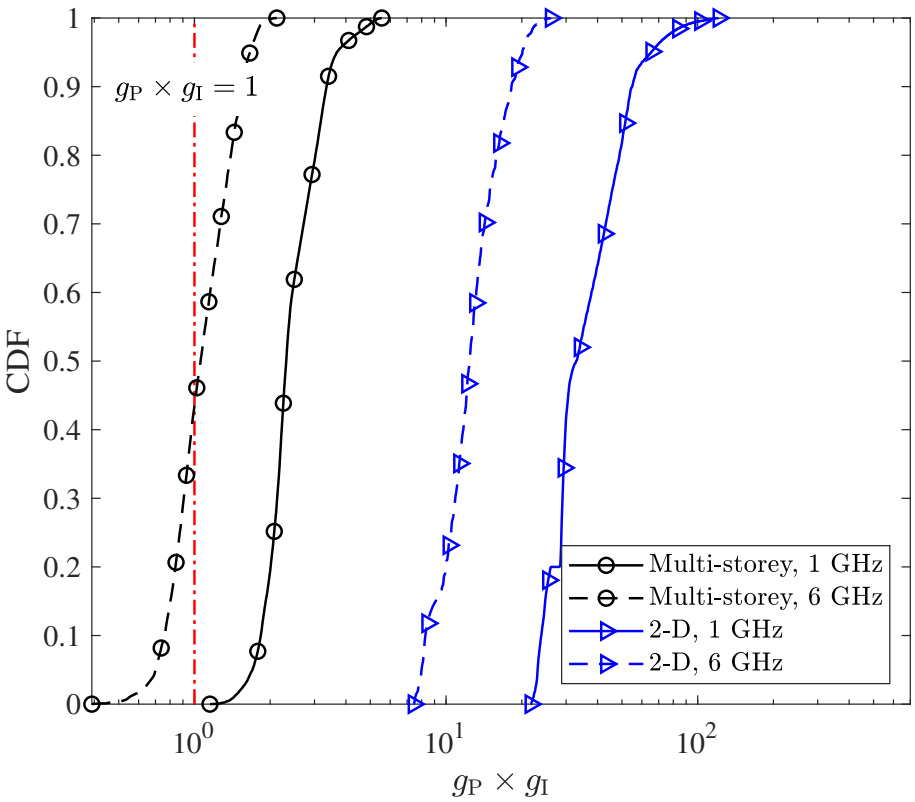

Fig. 5.14 The CDFs of $g_P g_I$ in a 5-storey building with a WINNER II A1 layout.

office building shows a positive impact on the maximum achievable network performance for all the UE locations at 1 GHz. Whereas it can degrade the maximum achievable network performance on about 43% of the UE locations at 6 GHz.

The results are compared with those generated by the 2-D BWP evaluation scheme in [19–22], where the path gain is computed with the 2-D link length, all the cross-floor associations/interference is ignored, and the transmit elements are confined in the envelope of the building for the sake of fairness. The 2-D method introduces considerable extra intended signal power from the surrounding transmit elements since the power loss caused by the height difference between the transmit elements and the probing UE is omitted. Consequently, as shown in Fig. 5.12, g_P is overestimated by the 2-D BWP evaluation scheme. Moreover, g_P at 1 GHz becomes lower than it at 6 GHz when computed without counting the cross-floor intended signal power from the adjacent storeys. As shown in Fig. 5.13b, the 2-D method also overestimates g_I because the cross-floor interference is ignored. The gap between the 2-D and the multi-storey methods is more considerable at 1 GHz since the cross-floor interference power takes a larger portion in total interference power at 1 GHz. As shown in Fig. 5.14,

when derived by the 2-D method, $g_{\mathrm{P}}g_{\mathrm{I}}$ is overestimated 15 times and 12 times at 1 GHz and 6 GHz, respectively. The significant difference between the evaluation results indicates that it is necessary to address the effects of the Tx-Rx height difference and the cross-floor associations/interference in the BWP evaluation by the proposed method.

5.6 Summary

In this chapter, a multi-storey BWP evaluation scheme has been proposed. The BWP FoMs, i.e., the PG and the IG, have been defined for multi-storey buildings. The analytical models to compute the BWP FoMs have been given in closed-form expressions. The BWP analysis has been demonstrated in a typical office building in different frequency bands and compared with the results generated by the 2-D BWP evaluation scheme. Numerical results show that the BWP varies among different storeys and is significantly affected by the 3-D building properties, including the number of storeys and their height. The comparison indicates that it is necessary to address the effects of the Tx-Rx height difference and the cross-floor associations/interference in the BWP evaluation for multi-storey buildings.

Chapter 6

Conclusion and Future Works

6.1 Conclusion

This thesis has investigated the effects of building structures on indoor wireless communications. A LOS probability model has been proposed for 3-D indoor environments in Chapter 3. The proposed model can be used to compute the LOS probability based on the exact layout of a building accurately, which can be employed in indoor wireless network performance evaluation and optimisation. A partition-based BWP evaluation scheme has been proposed in Chapter 4. It has induced the site-specific information into the BWP evaluation by counting the exact number of intersections for NLOS Tx-Rx links. In contrast to the initial works discussing the BWP, numerical results generated by the proposed method showed that the rooms with the same dimensions could vary in BWP significantly due to different relative locations in a building. The partition-based BWP evaluation scheme has enabled the BWP FoMs to capture the impact of building materials and layouts on indoor wireless network performance on a 2-D plane. A multi-storey BWP evaluation scheme has been proposed in Chapter 5. The BWP FoMs, i.e., the PG and the IG, have been defined for multi-storey buildings. Numerical results showed that the BWP varies among different storeys and is significantly affected by the number of storeys and their height. The multi-storey BWP evaluation scheme has addressed the effects of 3-D building properties, including the number of storeys and their height, on indoor wireless network performance. The proposed partition-based and multi-storey BWP evaluation schemes can be employed to assess the BWP at the design stage of a building to avoid costly building modification or retrofitting due to inadequate BWP.

6.2 Future Works

Based on the studies in this thesis, several further works are expected to be addressed in the short term. The 3-D indoor LOS probability model will be used to obtain analytical models of wireless network performance metrics in a given building, e.g., the coverage probability and capacity. Then the relationships between indoor network performance and general parameters of indoor networks, e.g., the density of SBSs, can be explored in a given building. For the BWP evaluation, the partition-based and multi-storey BWP evaluation schemes can be combined to include the effects of building materials and 3-D building properties simultaneously. In the prior works and this thesis, the transmit elements were assumed deployed on one or multiple planes. In future works, the transmit elements can be considered to be deployed in arbitrary locations in 3-D space. Considering the randomness of SBSs in future indoor networks, a 3-D indoor network model can be more practical for the BWP evaluation.

There are some open issues left in the BWP framework for long-term research [21]. The effects of small indoor obstacles, such as human bodies and furniture, will be modelled to address their impact on indoor network performance. The effects of building materials on the BWP should be specified by including the EM properties and the thickness of the material and considering the incident angles of EM waves. Only downlink transmissions have been considered in previous works and this thesis. A BWP framework considering both downlink and uplink transmissions should be investigated.

In previous works and this thesis, a general and idealistic network model was employed to present the maximum achievable performance gain in a given building. Consequently, it was not feasible to design practical experiments to validate the analytical models. In future works, the BWP will further correspond to specific wireless techniques, and hence the BWP evaluation schemes will be proposed considering the intrinsic constraints of the wireless techniques accordingly. Then practical experiments will be conducted to validate the proposed analytical models.

References

[1] S. Chen, Y. C. Liang, S. Sun, S. Kang, W. Cheng, and M. Peng, "Vision, requirements, and technology trend of 6G: How to tackle the challenges of system coverage, capacity, user data-rate and movement speed," *IEEE Wireless Commun.*, vol. 27, no. 2, pp. 218–228, Apr. 2020.

[2] ITU-R, "Requirements related to technical performance for IMT-Advanced radio interface(s)," Recommendation ITU-R M.2134, 2008. [Online]. Available: https://www.itu.int/pub/R-REP-M.2134-2008

[3] ——, "IMT Vision – Framework and overall objectives of the future development of IMT for 2020 and beyond," Recommendation ITU-R M.2083-0, 2015. [Online]. Available: https://www.itu.int/rec/R-REC-M.2150-0-202102-I

[4] Z. Zhang *et al.*, "6G wireless networks: Vision, requirements, architecture, and key technologies," *IEEE Veh. Technol. Mag.*, vol. 14, no. 3, pp. 28–41, Sep. 2019.

[5] I. F. Akyildiz, A. Kak, and S. Nie, "6G and beyond: The future of wireless communications systems," *IEEE Access*, vol. 8, pp. 133 995–134 030, 2020.

[6] S. Dang *et al.*, "What should 6G be?" *Nat. Electron.*, vol. 3, pp. 20–29, 2020. [Online]. Available: https://doi.org/10.1038/s41928-019-0355-6

[7] Cisco, "Cisco annual internet report (2018–2023)," White Paper. [Online]. Available: https://www.cisco.com/c/en/us/solutions/collateral/executive-perspectives/annual-internet-report/white-paper-c11-741490.pdf

[8] ——, "Cisco vision: 5G-thriving indoors," White Paper. [Online]. Available: https://www.cisco.com/c/dam/en/us/solutions/collateral/service-provider/ultra-services-platform/5g-ran-indoor.pdf

[9] T. Abergel, B. Dean, and J. Dulac, "Towards a zero-emission, efficient, and resilient buildings and construction sector global status report 2017," Tech. Rep., 2017.

[10] European Commission. [Online]. Available: https://ec.europa.eu/energy/eu-buildings-factsheets-topics-tree/energy-use-buildings_en

[11] A. Abrol and R. K. Jha, "Power optimization in 5G networks: A step towards green communication," *IEEE Access*, vol. 4, pp. 1355–1374, 2016.

[12] C.-L. I, S. Han, and S. Bian, "Energy-efficient 5G for a greener future," *Nat. Electron.*, vol. 3, pp. 182–184, Apr. 2020.

[13] T. Bai, R. Vaze, and R. W. Heath, "Analysis of blockage effects on urban cellular networks," *IEEE Trans. Wireless Commun.*, vol. 13, no. 9, pp. 5070–5083, Sep. 2014.

[14] N. Bhushan *et al.*, "Network densification: The dominant theme for wireless evolution into 5G," *IEEE Commun. Mag.*, vol. 52, no. 2, pp. 82–89, Feb. 2014.

[15] D. Lee *et al.*, "Coordinated multipoint transmission and reception in LTE-advanced: deployment scenarios and operational challenges," *IEEE Commun. Mag.*, vol. 50, no. 2, pp. 148–155, Feb. 2012.

[16] M. Ding, P. Wang, D. López-Pérez, G. Mao, and Z. Lin, "Performance impact of LoS and NLoS transmissions in dense cellular networks," *IEEE Trans. Wireless Commun.*, vol. 15, no. 3, pp. 2365–2380, Mar. 2016.

[17] H. Zheng, J. Zhang, H. Hu, and J. Zhang, "The analysis of indoor wireless communications by a blockage model in ultra-dense networks," in *88th IEEE Veh. Tech. Conf. (VTC Fall)*, Chicago, IL, USA, 2018, pp. 1–6.

[18] A. K. Brown, "The wireless friendly building," in *Loughborough Antennas Propag. Conf.*, Loughborough, UK, 2010, pp. 62–66.

[19] J. Zhang, A. A. Glazunov, H. Song, and J. Zhang, "Evaluating the wireless performance of a building," UK Patent, 2019.

[20] J. Zhang, A. A. Glazunov, and J. Zhang, "Wireless performance evaluation of building layouts: Closed-form computation of figures of merit," *IEEE Trans. Commun.*, vol. 69, no. 7, pp. 4890–4906, July 2021.

[21] J. Zhang, A. A. Glazunov, W. Yang, and J. Zhang, "Fundamental wireless performance of a building," *IEEE Wireless Commun.*, early access.

[22] J. Zhang, A. A. Glazunov, and J. Zhang, "Wireless energy efficiency evaluation for buildings under design based on analysis of interference gain," *IEEE Trans. Veh. Technol.*, vol. 69, pp. 6310–6324, June 2020.

[23] G. R. Maccartney, T. S. Rappaport, S. Sun, and S. Deng, "Indoor office wideband millimeter-wave propagation measurements and channel models at 28 and 73 GHz for ultra-dense 5G wireless networks," *IEEE Access*, vol. 3, pp. 2388–2424, 2015.

[24] G. R. Maccartney, S. Deng, and T. S. Rappaport, "Indoor office plan environment and layout-based mmWave path loss models for 28 GHz and 73 GHz," in *83rd IEEE Veh. Tech. Conf. (VTC Spring)*, Nanjing, China, 2016, pp. 1–6.

[25] X. Wu *et al.*, "60-GHz millimeter-wave channel measurements and modeling for indoor office environments," *IEEE Trans. Antennas Propag.*, vol. 65, no. 4, pp. 1912–1924, Feb. 2017.

[26] M. Martinez-Ingles, J. Pascual-García, D. P. Gaillot, C. S. Borras, and J. Molina-García-Pardo, "Indoor 1-40 GHz channel measurements," in *13th Eur. Conf. Antennas and Propag. (EuCAP)*, Krakow, Poland, 2019, pp. 1–5.

[27] F. Erden, O. Ozdemir, and I. Guvenc, "28 GHz mmWave channel measurements and modeling in a library environment," in *IEEE Radio and Wireless Symp. (RWS)*, San Antonio, TX, USA, 2020, pp. 52–55.

[28] M. Kyro *et al.*, "Measurement based path loss and delay spread modeling in hospital environments at 60 GHz," *IEEE Trans. Wireless Commun.*, vol. 10, no. 8, pp. 2423–2427, Aug. 2011.

[29] I. D. S. Batalha *et al.*, "Indoor corridor and office propagation measurements and channel models at 8, 9, 10 and 11 GHz," *IEEE Access*, vol. 7, pp. 55 005–55 021, 2019.

[30] X. Raimundo, S. Salous, and A. A. Cheema, "Indoor radio propagation measurements in the V-band," in *Radio Propag. and Technol. for 5G*, Durham, UK, 2016, pp. 1–5.

[31] ITU-R, "Propagation data and prediction methods for the planning of indoor radiocommunication systems and radio local area networks in the frequency range 300 MHz to 450 GHz," Recommendation ITU-R P.1238-10, 2019. [Online]. Available: https://www.itu.int/rec/R-REC-P.1238-10-201908-I

[32] P. Kyösti *et al.*, "WINNER II channel models," WINNER II, Tech. Rep. IST-4-027756 D1.1.2 V1.2, Feb. 2008.

[33] S. Piersanti, L. A. Annoni, and D. Cassioli, "Millimeter waves channel measurements and path loss models," in *IEEE Int. Conf. Commun. (ICC)*, Ottawa, ON, Canada, 2012, pp. 4552–4556.

[34] S. Sun *et al.*, "Propagation path loss models for 5G urban micro- and macro-cellular scenarios," in *IEEE 83rd Veh. Tech. Conf. (VTC Spring)*, Nanjing, China, 2016, pp. 1–6.

[35] G. Durgin, T. Rappaport, and H. Xu, "Partition-based path loss analysis for in-home and residential areas at 5.85 GHz," in *IEEE Global Commun. Conf. (GLOBECOM)*, vol. 2, Sydney, NSW, Australia, 1998, pp. 904–909.

[36] J. Keenan and A. J. Motley, "Radio coverage in buildings," *British Telecom Tech. J*, vol. 8, pp. 19–24, Jan. 1990.

[37] M. Lott and I. Forkel, "A multi-wall-and-floor model for indoor radio propagation," in *53rd IEEE Veh. Tech. Conf. (VTC Spring)*, vol. 1, Rhodes, Greece, 2001, pp. 464–468.

[38] A. G. M. Lima and L. F. Menezes, "Motley-Keenan model adjusted to the thickness of the wall," in *Int. Conf. Microw. and Optoelectronics (IMOC)*, Brasilia, Brazil, 2005, pp. 180–182.

[39] S. Hosseinzadeh, H. Larijani, and K. Curtis, "An enhanced modified multi wall propagation model," in *Global Internet of Things Summit (GIoTS)*, Geneva, Switzerland, 2017, pp. 1–4.

[40] C. Yang, B. Wu, and C. Ko, "A ray-tracing method for modeling indoor wave propagation and penetration," *IEEE Trans. Antennas Propag.*, vol. 46, no. 6, pp. 907–919, June 1998.

[41] A. S. Glassner, "An overview of ray tracing," in *An Introduction to Ray Tracing*, 1st ed., A. S. Glassner, Ed. GBR: Academic Press Ltd., 1989, ch. 1, pp. 1–31.

[42] J. S. Lu *et al.*, "A discrete environment-driven GPU-based ray launching algorithm," *IEEE Trans. Antennas Propag.*, vol. 67, no. 2, pp. 1180–1192, Feb. 2019.

[43] C. E. O. Vargas, L. d. S. Mello, and R. C. Rodriguez, "Measurements of construction materials penetration losses at frequencies from 26.5 GHz to 40 GHz," in *IEEE Pacific Rim Conf. Commun., Comput. and Signal Process. (PACRIM)*, Victoria, BC, Canada, 2017, pp. 1–4.

[44] H. Zhao *et al.*, "28 GHz millimeter wave cellular communication measurements for reflection and penetration loss in and around buildings in New York City," in *IEEE Int. Conf. Communications (ICC)*, Budapest, Hungary, 2013, pp. 5163–5167.

[45] C. E. O. Vargas and L. d. S. Mello, "Measurements of reflection and penetration loss of construction materials at 28 GHz and 38 GHz," in *IEEE-APS Topical Conf. Antennas and Propag. in Wireless Commun. (APWC)*, Cartagena des Indias, Colombia, 2018, pp. 897–900.

[46] G. L. B. Langen and W. Herzig, "Reflection and transmission behaviour of building materials at 60 GHz," in *5th IEEE Int. Symp. Pers., Indoor, Mobile Radio Commun. (PIMRC)*, The Hague, Netherlands, 1994, pp. 505–509.

[47] J. Ryan, G. R. MacCartney, and T. S. Rappaport, "Indoor office wideband penetration loss measurements at 73 GHz," in *IEEE Int. Conf. Commun. Workshops (ICC Workshops)*, Paris, France, 2017, pp. 228–233.

[48] T. S. Rappaport *et al.*, "Wireless communications and applications above 100 GHz: Opportunities and challenges for 6G and beyond," *IEEE Access*, vol. 7, pp. 78 729–78 757, 2019.

[49] I. Cuiñas and M. G. Sánchez, "Permittivity and conductivity measurements of building materials at 5.8 GHz and 41.5 GHz," *Wireless Pers. Commun.*, vol. 20, no. 1, pp. 93–100, Jan. 2002.

[50] W. Yang, J. Huang, J. Zhang, Y. Gao, S. Salous, and J. Zhang, "Measurements of reflection and penetration loss in indoor environments in the 39-GHz band," in *15th Eur. Conf. Antennas and Propag. (EuCAP)*, Düsseldorf, Germany, 2021, pp. 83–87.

[51] K. Sato *et al.*, "Measurements of reflection and transmission characteristics of interior structures of office building in the 60-GHz band," *IEEE Trans. Antennas Propag.*, vol. 45, no. 12, pp. 1783–1792, Dec. 1997.

[52] J. Lahteenmaki and T. Karttaavi, "Measurement of dielectric parameters of wall materials at 60 GHz band," *Electron. Lett.*, vol. 32, no. 16, pp. 1442–1444, Aug. 1996.

[53] J. Lu, D. Steinbach, P. Cabrol, P. Pietraski, and R. V. Pragada, "Propagation characterization of an office building in the 60 GHz band," in *8th Eur. Conf. Antennas and Propag. (EuCAP)*, The Hague, Netherlands, 2014, pp. 809–813.

[54] S. N. J. Ahmadi-Shokouh and H.Keshavarz, "Reflection coefficient measurement for north American house flooring at 57–64 GHz," *IEEE Antennas Wireless Propag. Lett.*, vol. 10, pp. 1321–1324, Nov. 2011.

[55] I. Cuinas, J. P. Pugliese, A. Hammoudeh, and M. G. Sanchez, "Comparison of the electromagnetic properties of building materials at 5.8 GHz and 62.4 GHz," in *52nd IEEE Veh. Tech. Conf. (VTC Fall)*, vol. 2, Boston, MA, USA, 2000, pp. 780–785.

[56] D. Ferreira, I. Cuiñas, R. F. S. Caldeirinha, and T. R. Fernandes, "A review on the electromagnetic characterisation of building materials at micro- and millimetre wave frequencies," in *8th Eur. Conf. Antennas and Propag. (EuCAP)*, The Hague, Netherlands, 2014, pp. 145–149.

[57] S. S. Zhekov, O. Franek, and G. F. Pedersen, "Dielectric properties of common building materials for ultrawideband propagation studies," *IEEE Antennas Propag. Mag.*, vol. 62, no. 1, pp. 72–81, Feb. 2020.

[58] ITU-R, "Effects of building materials and structures on radiowave propagation above about 100 MHz," Recommendation ITU-R P.2040, 2015. [Online]. Available: https://www.itu.int/rec/R-REC-P.2040-1-201507-I

[59] R. G. Kouyoumjian and P. H. Pathak, "A uniform geometrical theory of diffraction for an edge in a perfectly conducting surface," *Proc. IEEE*, vol. 62, no. 11, pp. 1448–1461, 1974.

[60] T. S. Rappaport, Ed., *Wireless Communications: Principles and Practice*, 2nd ed. Upper Saddle River, NJ, USA: Prentice-Hall, 2002.

[61] R. G. Kouyoumjian and P. H. Pathak, "A uniform geometrical theory of diffraction for an edge in a perfectly conducting surface," *Proc. IEEE*, vol. 62, no. 11, pp. 1448–1461, Nov. 1974.

[62] T. S. Rappaport, G. R. MacCartney, S. Sun, H. Yan, and S. Deng, "Small-scale, local area, and transitional millimeter wave propagation for 5G communications," *IEEE Trans. Antennas Propag.*, vol. 65, no. 12, pp. 6474–6490, Dec. 2017.

[63] M. Jacob, S. Priebe, R. Dickhoff, T. Kleine-Ostmann, T. Schrader, and T. Kurner, "Diffraction in mm and sub-mm wave indoor propagation channels," *IEEE Trans. Microw. Theory Techn.*, vol. 60, no. 3, pp. 833–844, Mar. 2012.

[64] J. Kunisch and J. Pamp, "Ultra-wideband double vertical knife-edge model for obstruction of a ray by a person," in *IEEE Int. Conf. Ultra-Wideband*, vol. 2, Hannover, Germany, 2008, pp. 17–20.

[65] ITU-R, "Propagation by diffraction," Recommendation ITU-R P.526-25, 2019. [Online]. Available: https://www.itu.int/rec/R-REC-P.526-15-201910-I

[66] K. A. Remley, H. R. Anderson, and A. Weisshar, "Improving the accuracy of ray-tracing techniques for indoor propagation modeling," *IEEE Trans. Veh. Technol.*, vol. 49, no. 6, pp. 2350–2358, Nov. 2000.

[67] P. Bernardi, R. Cicchetti, and O. Testa, "An accurate UTD model for the analysis of complex indoor radio environments in microwave WLAN systems," *IEEE Trans. Antennas Propag.*, vol. 52, no. 6, pp. 1509–1520, June 2004.

[68] H. Wang and T. S. Rappaport, "A parametric formulation of the UTD diffraction coefficient for real-time propagation prediction modeling," *IEEE Antennas Wireless Propag. Lett.*, vol. 4, pp. 253–257, 2005.

[69] J. -V. Rodriguez, J. -M. Molina-Garcia-Pardo, and L. Juan-Llacer, "An improved solution expressed in terms of UTD coefficients for the multiple-building diffraction of plane waves," *IEEE Antennas Wireless Propag. Lett.*, vol. 4, pp. 16–19, 2005.

[70] A. V. Osipov, "A simple approximation of the Maliuzhinets function for describing wedge diffraction," *IEEE Trans. Antennas Propag.*, vol. 53, no. 8, pp. 2773–2776, Aug. 2005.

[71] V. Degli-Esposti and H. L. Bertoni, "Evaluation of the role of diffuse scattering in urban microcellular propagation," in *50th IEEE Veh. Tech. Conf. (VTC Fall)*, vol. 3, Amsterdam, Netherlands, 1999, pp. 1392–1396.

[72] V. Degli-Esposti, "A diffuse scattering model for urban propagation prediction," *IEEE Trans. Antennas Propag.*, vol. 49, no. 7, pp. 1111–1113, July 2001.

[73] V. Degli-Esposti, F. Fuschini, E. M. Vitucci, and G. Falciasecca, "Measurement and modelling of scattering from buildings," *IEEE Trans. Antennas Propag.*, vol. 55, no. 1, pp. 143–153, Jan. 2007.

[74] F. Mani, F. Quitin, and C. Oestges, "Accuracy of depolarization and delay spread predictions using advanced ray-based modeling in indoor scenarios," *EURASIP J. Wireless Commun. Netw.*, vol. 2011, no. 1, pp. 1–9, Dec. 2011.

[75] N. Zhang *et al.*, "Dynamic channel modeling for an indoor scenario at 23.5 GHz," *IEEE Access*, vol. 3, pp. 2950–2958, 2015.

[76] M. Inomata, M. Sasaki, M. Nakamura, and Y. Takatori, "Diffuse scattering prediction for 26 GHz band in indoor office environments," in *Int. Symp. on Antennas and Propag. (ISAP)*, Phuket, Thailand, 2017, pp. 1–2.

[77] J. Jürvelüinen and K. Haneda, "Sixty gigahertz indoor radio wave propagation prediction method based on full scattering model," *Radio Sci.*, vol. 49, no. 4, pp. 293–305, 2014.

[78] J. Pascual-García, M. Martínez-Inglés, J. Molina-García-Pardo, J. Rodríguez, and L. J. Llácer, "Using tuned diffuse scattering parameters in ray tracing channel modeling," in *9th Eur. Conf. Antennas and Propag. (EuCAP)*, Lisbon, Portugal, 2015, pp. 1–4.

[79] X. Liao, Y. Shao, Y. Wang, and T. Hu, "Experimental study of diffuse scattering from typical construction materials over 40-50 GHz," in *IEEE Asia-Pacific Conf. Antennas and Propag. (APCAP)*, Auckland, New Zealand, 2018, pp. 216–218.

[80] J. Pascual-García, M. Martínez-Inglés, J. Molina-García-Pardo, J. Rodríguez, and V. Degli-Esposti, "Experimental parameterization of a diffuse scattering model at 60 GHz," in *IEEE-APS Topical Conf. Antennas and Propag. in Wireless Commun. (APWC)*, Turin, Italy, 2015, pp. 734–737.

[81] J. Pascual-García, J. Molina-García-Pardo, M. Martínez-Inglés, J. Rodríguez, and N. Saurín-Serrano, "On the importance of diffuse scattering model parameterization in indoor wireless channels at mm-Wave frequencies," *IEEE Access*, vol. 4, pp. 688–701, 2016.

[82] K. S. Gilhousen, I. M. Jacobs, R. Padovani, A. J. Viterbi, L. A. Weaver, and C. E. Wheatley, "On the capacity of a cellular CDMA system," *IEEE Trans. Veh. Technol.*, vol. 40, no. 2, pp. 303–312, May 1991.

[83] A. D. Wyner, "Shannon-theoretic approach to a Gaussian cellular multiple-access channel," *IEEE Trans. Inf. Theory*, vol. 40, no. 6, pp. 1713–1727, Nov. 1994.

[84] S. Shamai and A. D. Wyner, "Information-theoretic considerations for symmetric, cellular, multiple-access fading channels. I," *IEEE Trans. Inf. Theory*, vol. 43, no. 6, pp. 1877–1894, Nov. 1997.

[85] ——, "Information-theoretic considerations for symmetric, cellular, multiple-access fading channels. II," *IEEE Trans. Inf. Theory*, vol. 43, no. 6, pp. 1895–1911, Nov. 1997.

[86] O. Somekh and S. Shamai, "Shannon-theoretic approach to a Gaussian cellular multiple-access channel with fading," *IEEE Trans. Inf. Theory*, vol. 46, no. 4, pp. 1401–1425, July 2000.

[87] T. X. Brown, "Cellular performance bounds via shotgun cellular systems," *IEEE J. Sel. Areas Commun.*, vol. 18, no. 11, pp. 2443–2455, Nov. 2000.

[88] M. Haenggi, J. G. Andrews, F. Baccelli, O. Dousse, and M. Franceschetti, "Stochastic geometry and random graphs for the analysis and design of wireless networks," *IEEE J. Sel. Areas Commun.*, vol. 27, no. 7, pp. 1029–1046, Sep. 2009.

[89] J. G. Andrews, F. Baccelli, and R. K. Ganti, "A tractable approach to coverage and rate in cellular networks," *IEEE Trans. Commun.*, vol. 59, no. 11, pp. 3122–3134, Nov. 2011.

[90] Y. Li, F. Baccelli, H. S. Dhillon, and J. G. Andrews, "Statistical modeling and probabilistic analysis of cellular networks with determinantal point processes," *IEEE Trans. Commun.*, vol. 63, no. 9, pp. 3405–3422, Sep. 2015.

[91] N. Deng, W. Zhou, and M. Haenggi, "The ginibre point process as a model for wireless networks with repulsion," *IEEE Trans. Wireless Commun.*, vol. 14, no. 1, pp. 107–121, Jan. 2015.

[92] Y. Wang and Q. Zhu, "Modeling and analysis of small cells based on clustered stochastic geometry," *IEEE Commun. Lett.*, vol. 21, no. 3, pp. 576–579, Mar. 2017.

[93] H.-S. Jo, Y. J. Sang, P. Xia, and J. G. Andrews, "Heterogeneous cellular networks with flexible cell association: A comprehensive downlink SINR analysis," *IEEE Trans. Wireless Commun.*, vol. 11, no. 10, pp. 3484–3495, Oct. 2012.

[94] H. S. Dhillon, R. K. Ganti, F. Baccelli, and J. G. Andrews, "Modeling and analysis of *K*-tier downlink heterogeneous cellular networks," *IEEE J. Sel. Areas Commun.*, vol. 30, no. 3, pp. 550–560, Apr. 2012.

[95] Y. J. Chun, M. O. Hasna, and A. Ghrayeb, "Modeling heterogeneous cellular networks interference using Poisson cluster processes," *IEEE J. Sel. Areas Commun.*, vol. 33, no. 10, pp. 2182–2195, Oct. 2015.

[96] N. Deng, W. Zhou, and M. Haenggi, "Heterogeneous cellular network models with dependence," *IEEE J. Sel. Areas Commun.*, vol. 33, no. 10, pp. 2167–2181, Oct. 2015.

[97] I. Flint, H. Kong, N. Privault, P. Wang, and D. Niyato, "Analysis of heterogeneous wireless networks using Poisson hard-core hole process," *IEEE Trans. Wireless Commun.*, vol. 16, no. 11, pp. 7152–7167, Nov. 2017.

[98] Z. Pan and Q. Zhu, "Modeling and analysis of coverage in 3-D cellular networks," *IEEE Commun. Lett.*, vol. 19, no. 5, pp. 831–834, May 2015.

[99] J. Miao, X. Gu, B. Leng, and L. Zhang, "Modelling and analysis of 3-D cellular networks using a Matern cluster process," in *30th IEEE Int. Symp. Pers., Indoor, Mobile Radio Commun. (PIMRC)*, Istanbul, Turkey, 2019, pp. 1–6.

[100] A. Omri and M. O. Hasna, "Modeling and performance analysis of D2D communications with interference management in 3-D HetNets," in *IEEE Global Commun. Conf. (GLOBECOM)*, Washington, DC, USA, 2016, pp. 1–7.

[101] ——, "Modeling and performance analysis of 3-D heterogeneous networks with interference management," *IEEE Commun. Lett.*, vol. 21, no. 8, pp. 1787–1790, Aug. 2017.

[102] 3GPP, "Study on channel model for frequencies from 0.5 to 100 GHz," 3rd Generation Partnership Project (3GPP), Tech. Rep. TR 38.901 V14.1.1 Release 14, 2017. [Online]. Available: http://www.3gpp.org/DynaReport/38901.htm

[103] I. Atzeni, J. Arnau, and M. Kountouris, "Downlink cellular network analysis with LOS/NLOS propagation and elevated base stations," *IEEE Trans. Wireless Commun.*, vol. 17, no. 1, pp. 142–156, Jan. 2018.

[104] J. Yang, M. Ding, G. Mao, Z. Lin, D. Zhang, and T. H. Luan, "Optimal base station antenna downtilt in downlink cellular networks," *IEEE Trans. Wireless Commun.*, vol. 18, no. 3, pp. 1779–1791, Mar. 2019.

[105] H. Zheng, J. Zhang, H. Li, Q. Hong, H. Hu, and J. Zhang, "Exact line-of-sight probability for channel modeling in typical indoor environments," *IEEE Antennas Wireless Propag. Lett.*, vol. 17, no. 7, pp. 1359–1362, July 2018.

[106] W. Yang, J. Zhang, and J. Zhang, "Machine learning based indoor line-of-sight probability prediction," in *Int. Symp. Antennas and Propag. (ISAP)*, Xian, China, 2019, pp. 1–3.

[107] A. K. Gupta, J. G. Andrews, and R. W. Heath, "Macrodiversity in cellular networks with random blockages," *IEEE Trans. Wireless Commun.*, vol. 17, no. 2, pp. 996–1010, Feb. 2018.

[108] M. Taranetz, R. W. Heath, and M. Rupp, "Analysis of urban two-tier heterogeneous mobile networks with small cell partitioning," *IEEE Trans. Wireless Commun.*, vol. 15, no. 10, pp. 7044–7057, Oct. 2016.

[109] S. Niknam, B. Natarajan, and R. Barazideh, "Interference analysis for finite-area 5G mmWave networks considering blockage effect," *IEEE Access*, vol. 6, pp. 23 470–23 479, 2018.

[110] T. Bai and R. W. Heath, "Coverage and rate analysis for millimeter-wave cellular networks," *IEEE Trans. Wireless Commun.*, vol. 14, no. 2, pp. 1100–1114, Feb. 2015.

[111] M. N. Kulkarni, S. Singh, and J. G. Andrews, "Coverage and rate trends in dense urban mmWave cellular networks," in *IEEE Global Commun. Conf. (GLOBECOM)*, Austin, TX, USA, 2014, pp. 3809–3814.

[112] G. Franceschetti, S. Marano, and F. Palmieri, "Propagation without wave equation toward an urban area model," *IEEE Trans. Antennas Propag.*, vol. 47, no. 9, pp. 1393–1404, Sep. 1999.

[113] M. K. Müller, S. Schwarz, and M. Rupp, "Investigation of area spectral efficiency in indoor wireless communications by blockage models," in *16th Int. Symp. Model. and Optim. in Mobile, Ad Hoc, and Wireless Netw. (WiOpt)*, Shanghai, China, May 2018, pp. 1–6.

[114] M. K. Müller, M. Taranetz, and M. Rupp, "Analyzing wireless indoor communications by blockage models," *IEEE Access*, vol. 5, pp. 2172–2186, 2017.

[115] ——, "Effects of wall-angle distributions in indoor wireless communications," in *17th IEEE Workshop on Signal Process. Adv. in Wireless Commun. (SPAWC)*, Edinburgh, UK, 2016, pp. 1–5.

[116] W. Yang, J. Zhang, and J. Zhang, "On evaluation of indoor to outdoor communications using neighbourhood small cells," *IEEE Trans. Veh. Technol.*, vol. 69, no. 7, pp. 8045–8050, July 2020.

[117] X. Zhang, F. Baccelli, and R. W. Heath, "An indoor correlated shadowing model," in *IEEE Global Commun. Conf. (GLOBECOM)*, San Diego, CA, USA, 2015, pp. 1–7.

[118] Y. Wu, J. Kokkoniemi, C. Han, and M. Juntti, "Interference and coverage analysis for terahertz networks with indoor blockage effects and line-of-sight access point association," *IEEE Trans. Wireless Commun.*, vol. 20, no. 3, pp. 1472–1486, Mar. 2021.

[119] S. Yan, M. Peng, W. Chen, J. Wang, M. A. Abana, and L. Yang, "Downlink heterogeneous small cell networks with cell associations in K-floor indoor scenarios," in *IEEE Int. Conf. Commun. Workshop (ICCW)*, London, UK, 2015, pp. 2550–2554.

[120] Y. Zhang, W. Xu, and X. Li, "Multi-floor PPP model for performance analysis of indoor wireless networks," in *19th Int. Symp. Wireless Pers. Multimedia Commun. (WPMC)*, Shenzhen, China, 2016, pp. 371–376.

[121] C. Chen, Y. Zhang, J. Zhang, X. Chu, and J. Zhang, "On the performance of indoor multi-story small-cell networks," *IEEE Trans. Wireless Commun.*, vol. 20, no. 2, pp. 1336–1348, Feb. 2021.

[122] S. Jiang, X. Wen, Z. Lu, W. Zheng, and T. Lei, "K-floors HCPP model based performance analysis of indoor ultra-dense WLANs," in *IEEE Int. Conf. Commun. Workshops (ICC Workshops)*, Kansas City, MO, USA, 2018, pp. 1–6.

[123] J. Lee, X. Zhang, and F. Baccelli, "A 3-D spatial model for in-building wireless networks with correlated shadowing," *IEEE Trans. Wireless Commun.*, vol. 15, no. 11, pp. 7778–7793, Nov. 2016.

[124] L. Zhang, X. Gu, Z. Liu, L. Zhang, and H. Moon, "Modeling and analysis of indoor coverage probability for future 3D dense mobile networks," in *20th Int. Symp. Wireless Pers. Multimedia Commun. (WPMC)*, Bali, Indonesia, Dec. 2017, pp. 247–252.

[125] I. Trigui, S. Affes, and B. Liang, "Unified stochastic geometry modeling and analysis of cellular networks in LOS/NLOS and shadowed fading," *IEEE Trans. Commun.*, vol. 65, no. 12, pp. 5470–5486, Dec. 2017.

[126] A. Zanella, N. Bui, A. Castellani, L. Vangelista, and M. Zorzi, "Internet of things for smart cities," *IEEE Internet Things J.*, vol. 1, no. 1, pp. 22–32, Feb. 2014.

[127] H. Jiang, C. Cai, X. Ma, Y. Yang, and J. Liu, "Smart home based on WiFi sensing: A survey," *IEEE Access*, vol. 6, pp. 13 317–13 325, 2018.

[128] R. Fakler, "Buffon's needle problem for a rectangular grid," *National Council of Teachers of Math.*, vol. 88, no. 3, pp. 205–208, Mar. 1995.

[129] A. Horwitz, "A version of Simpson's rule for multiple integrals," *J. Comput. Appl. Math.*, vol. 134, pp. 1–11, 2001.

[130] D. López-Pérez, M. Ding, H. Claussen, and A. H. Jafari, "Towards 1 Gbps/UE in cellular systems: Understanding ultra-dense small cell deployments," *IEEE Commun. Surv. Tuts.*, vol. 17, no. 4, pp. 2078–2101, 4th Quart. 2015.

[131] Z. Yun and M. F. Iskander, "Ray tracing for radio propagation modeling: Principles and applications," *IEEE Access*, vol. 3, pp. 1089–1100, 2015.

[132] J. Zhang, A. A. Glazunov, J. Yang, X. Chu, and J. Zhang, "An experimental study on indoor massive 3D-MIMO channel at 30-40 GHz band," in *Int. Symp. Antennas and Propag. (ISAP)*, Busan, South Korea, 2018, pp. 1–2.

[133] J. G. Andrews, S. Buzzi, W. Choi, S. V. Hanly, A. Lozano, A. C. K. Soong, and J. C. Zhang, "What will 5G be?" *IEEE J. Sel. Areas Commun.*, vol. 32, no. 6, pp. 1065–1082, June 2014.

[134] E. Björnson, L. Sanguinetti, H. Wymeersch, J. Hoydis, and T. L. Marzetta, "Massive MIMO is a reality—What is next?: Five promising research directions for antenna arrays," *Digit. Signal Process.*, vol. 94, pp. 3–20, Nov. 2019.

[135] C. R. Anderson and T. S. Rappaport, "In-building wideband partition loss measurements at 2.5 and 60 GHz," *IEEE Trans. Wireless Commun.*, vol. 3, no. 3, pp. 922–928, May 2004.

[136] G. D. Durgin, T. S. Rappaport, and H. Xu, "5.85-GHz radio path loss and penetration loss measurements in and around homes and trees," *IEEE Commun. Lett.*, vol. 2, no. 3, pp. 70–72, Mar. 1998.

[137] L. Li, Y. Ibdah, Y. Ding, H. Eghbali, S. H. Muhaidat, and X. Ma, "Indoor multi-wall path loss model at 1.93 GHz," in *IEEE Mil. Commun. Conf. (MILCOM)*, San Diego, CA, USA, Nov. 2013, pp. 1233–1237.

[138] S. Y. Seidel and T. S. Rappaport, "914 MHz path loss prediction models for indoor wireless communications in multifloored buildings," *IEEE Trans. Antennas Propag.*, vol. 40, no. 2, pp. 207–217, Feb. 1992.

[139] W. Yang, J. Zhang, A. A. Glazunov, and J. Zhang, "Line-of-sight probability for channel modeling in 3-D indoor environments," *IEEE Antennas Wireless Propag. Lett.*, vol. 19, no. 7, pp. 1182–1186, July 2020.

[140] X. Zhang and J. G. Andrews, "Downlink cellular network analysis with multi-slope path loss models," *IEEE Trans. Commun.*, vol. 63, no. 5, pp. 1881–1894, May 2015.

[141] S. Christoph and D. Falko, "Using the right two-ray model? A measurement-based evaluation of PHY models in VANETs," in *Annu. Int. Conf. Mobile Comput. and Netw. (MobiCom)*, Las Vegas, NV, USA, 2011.

[142] W. N. Bailey, "On the reducibility of Appell's function F4," *Q. J. Math*, vol. 5, pp. 291–292, Jan. 1934.

Appendix A

Derivations of the closed-form expression of Z_1

The closed-form expression of $Z_1(\cdot)$ given in (4.22) was proposed in [20]. The detailed derivations omitted in [20] are given below.

A.1 Proof of closed-form Z_1 when $z_5 \neq 1$

When $z_5 \neq 1$, through some straightforward integral computation, (4.26) can be simplified into

$$Z_1(z_1, z_2, z_3, z_4, z_5) = \frac{z_4^{1-z_5}}{1-z_5} \int_{z_1}^{z_2} \cos^{z_5-1}(\theta) \mathrm{d}\theta + \frac{(z_1 - z_2) z_3^{1-z_5}}{1-z_5}. \tag{A.1}$$

The closed-form expression of (4.26) can be derived by solving $\int_0^x \cos^z(t)\mathrm{d}t$.

Lemma A.1. *For $0 \leq x < \frac{\pi}{2}$, $z \geq -1$, and $z \neq 0$, $\int_0^x \cos^z(t)\mathrm{d}t$ can be denoted in the closed-form expression as*

$$\int_0^x \cos^z(t)\mathrm{d}t = \begin{cases} \ln(\sec(x)) + \ln(\sin(x)+1), & z = -1, \\ \frac{1}{2}\mathrm{B}\left(\frac{z+1}{2}, \frac{1}{2}\right) & \\ -\frac{\cos^{1+z}(x)}{1+z} {}_2F_1\left(\frac{z+1}{2}, \frac{1}{2}; \frac{z+3}{2}; \cos^2(x)\right), & \text{else}, \end{cases} \tag{A.2}$$

where $\mathrm{B}(\cdot)$ represents the beta function.

Proof: For $z=-1$, the derivations are straightforward, therefore omitted here. For $z\neq 0,-1$, define $t_1=\cos^2(t)$, then

$$\begin{aligned}\int_0^x \cos^z(t)\mathrm{d}t =& \frac{1}{2}\int_0^1 t_1^{\frac{z-1}{2}}(1-t_1)^{-\frac{1}{2}}\mathrm{d}t_1 - \frac{1}{2}\int_0^{\cos^2(x)} t_1^{\frac{z-1}{2}}(1-t_1)^{-\frac{1}{2}}\mathrm{d}t_1 \\ \overset{(a)}{=}& \frac{1}{2}\mathrm{B}\left(\frac{z+1}{2},\frac{1}{2}\right) - \frac{\cos^{z+1}(x)}{1+z}{}_2F_1\left(\frac{z+1}{2},\frac{1}{2};\frac{z+3}{2};\cos^2(x)\right),\end{aligned} \tag{A.3}$$

where for (a), the first integral follows the beta function $\mathrm{B}(a,b)=\int_0^1 t^{a-1}(1-t)^{b-1}\mathrm{d}t$ and the second integral follows the property of the incomplete beta function $\mathrm{B}(y;a,b)=\int_0^y t^{a-1}(1-t)^{b-1}\mathrm{d}t=\frac{y^a}{a}{}_2F_1\left(a,1-b;a+1;y\right)$. ■

A.2 Proof of closed-form Z_1 when $z_5=1$

When $z_5=1$, through some straightforward integral computation, (4.26) can be initially simplified into

$$\begin{aligned}Z_1\left(z_1,z_2,z_3,z_4,z_5\right) &= \int_{z_1}^{z_2}\ln\left(\frac{z_4}{\cos(\theta)}\right)-\ln(z_3)\mathrm{d}\theta \\ &= (z_2-z_1)\ln\left(\frac{z_4}{z_3}\right) - \int_{z_1}^{z_2}\ln\left(\cos(\theta)\right)\mathrm{d}\theta,\end{aligned} \tag{A.4}$$

and then the closed-form expression can be derived by solving $\int_0^x \ln\left(\cos(t)\right)\mathrm{d}t$.

Lemma A.2. *For* $-\frac{\pi}{2}<x<\frac{\pi}{2}$,

$$\int_0^x \ln(\cos(t))\mathrm{d}t = -x\ln 2 - \mathrm{Im}\left\{\frac{\mathrm{Li}_2\left(-e^{2jx}\right)}{2}\right\}. \tag{A.5}$$

Proof: Let $t_1=-e^{2jt}$,

$$\begin{aligned}\int_0^x \ln\left(\cos(t)\right)\mathrm{d}t &\overset{(a)}{=} \int_0^x \ln\left(1+e^{2jt}\right)-\ln 2 - jt\mathrm{d}t \\ &\overset{(b)}{=} -\frac{jx^2}{2} - x\ln 2 + \frac{j}{2}\int_0^{-e^{2jx}}\frac{\mathrm{Li}_1\left(t_1\right)}{t_1}\mathrm{d}t_1 \\ &\overset{(c)}{=} -\frac{jx^2}{2} - x\ln 2 + \frac{j\mathrm{Li}_2\left(-e^{2jx}\right)}{2},\end{aligned} \tag{A.6}$$

where (a) is from the identity

$$\begin{aligned} &\ln\left(1+e^{2jx}\right) - \ln\left(\cos(x)\right) \equiv \ln\left(\frac{1+e^{2jx}}{\cos(x)}\right) \\ &\equiv \ln\left(e^{jx}\left(\frac{e^{-jx}+e^{jx}}{\cos(x)}\right)\right) \equiv \ln 2 + jx, \end{aligned} \tag{A.7}$$

(b) and (c) are from the definition $\mathrm{Li}_1(x) \triangleq -\ln(1-x)$ and the definition $\mathrm{Li}_2(x) \triangleq \int_0^x \frac{\mathrm{Li}_1(t)}{t}\mathrm{d}t$, respectively. Since $\ln\left(\cos(t)\right)$ is a real function for $-\frac{\pi}{2} < t < \frac{\pi}{2}$, $\mathrm{Im}\left\{\int_0^x \ln(\cos(t))\mathrm{d}t\right\} = 0$. According to (A.6),

$$\mathrm{Im}\left\{-\frac{jx^2}{2} - x\ln 2 + \frac{j\,\mathrm{Li}_2\left(-e^{2jx}\right)}{2}\right\} = 0, \tag{A.8}$$

and then

$$\mathrm{Im}\left\{\frac{j\mathrm{Li}_2\left(-e^{2jx}\right)}{2}\right\} = \frac{x^2}{2}. \tag{A.9}$$

Inserting (A.9) into (A.6), (A.5) can be obtained. ■

Inserting (A.2) and (A.5) to (A.1) and (A.4), respectively, the closed-form $Z_1\left(\cdot\right)$ in (4.22) can be obtained.

Appendix B

Derivations of the closed-form expression of $\mathscr{H}_2$

The detailed derivations of the closed-form expression of $\mathscr{H}_2(\cdot)$ in different cases are given as follows.

B.1 Proof of closed-form $\mathscr{H}_2$ when $n \neq 2$

When $n \neq 2$, following some algebraic manipulations,

$$\mathscr{H}_2(\theta_1,\theta_2,r_1,d,h,n) = \frac{d^{2-n}}{2-n}\int_{\theta_1}^{\theta_2}\left(\sec^2(\theta)+\frac{h^2}{d^2}\right)^{\frac{2-n}{2}}\mathrm{d}\theta - \frac{(\theta_2-\theta_1)}{2-n}\left({r_1}^2+h^2\right)^{\frac{2-n}{2}}, \tag{B.1}$$

where the first term can be derived by the following lemma.

Lemma B.1. For $-\frac{\pi}{2} < x < \frac{\pi}{2}$, $\alpha \neq -1$, and $\beta \neq 0$,

$$\int_0^x \left(\alpha+\sec^2(t)\right)^{\beta}\mathrm{d}t = (\alpha+1)^{\beta}\tan(x)F_1\left(\frac{1}{2};-\beta,1;\frac{3}{2};-\frac{\tan^2(x)}{\alpha+1},-\tan^2(x)\right). \tag{B.2}$$

Proof: Inserting $t_1 = \tan^2(t)$,

$$\int_0^x \left(\alpha+\sec^2(t)\right)^{\beta}\mathrm{d}t = \frac{1}{2}\int_0^{\tan^2(x)} {t_1}^{-\frac{1}{2}}\left(1+\alpha+t_1\right)^{\beta}\left(t_1+1\right)^{-1}\mathrm{d}t_1. \tag{B.3}$$

Then inserting $t_2 = \frac{t_1}{\tan^2(x)}$, (B.3) can be expressed by

$$\frac{1}{2}\tan(x)(\alpha+1)^{\beta}\int_0^1 t_2^{-\frac{1}{2}}\left(1+\frac{\tan^2(x)}{1+\alpha}t_2\right)^{\beta}(1+\tan^2(x)t_2)^{-1}\mathrm{d}t_2. \tag{B.4}$$

Introducing the property $F_1(a;b_1,b_2;c;x,y) = \frac{\Gamma(c)}{\Gamma(a)\Gamma(c-a)}\int_0^1 t^{a-1}(1-t)^{c-a-1}(1-xt)^{-b_1}(1-yt)^{-b_2}\mathrm{d}t$ for $\Re[a]>0$ and $\Re[c-a]>0$ [142], where $\Gamma(\cdot)$ represents the gamma function, there is (B.2). ■

Using Lemma 5.3 in (B.1), for $n \neq 2$,

$$\begin{aligned}
&\mathscr{H}_2(\theta_1,\theta_2,r_1,d,h,n)\\
&=\frac{(h^2+d^2)^{\frac{2-n}{2}}}{2-n}\tan(\theta_2)F_1\left(\frac{1}{2};\frac{n-2}{2},1;\frac{3}{2};-\frac{d^2\tan^2(\theta_2)}{h^2+d^2},-\tan^2(\theta_2)\right)\\
&-\frac{(h^2+d^2)^{\frac{2-n}{2}}}{2-n}\tan(\theta_1)F_1\left(\frac{1}{2};\frac{n-2}{2},1;\frac{3}{2};-\frac{d^2\tan^2(\theta_1)}{h^2+d^2},-\tan^2(\theta_1)\right)\\
&-\frac{(\theta_2-\theta_1)}{2-n}\left({r_1}^2+h^2\right)^{\frac{2-n}{2}}.
\end{aligned} \tag{B.5}$$

B.2 Proof of closed-form $\mathscr{H}_2$ when $n = 2$

When $n = 2$ and $h \neq 0$, (5.43) can be rewritten as

$$\begin{aligned}
\mathscr{H}_2(\theta_1,\theta_2,r_1,d,h,n) &= \int_{\theta_1}^{\theta_2}\int_{r_1}^{\frac{d}{\cos(\theta)}}\frac{r}{r^2+h^2}\mathrm{d}r\mathrm{d}\theta\\
&=\frac{1}{2}\int_{\theta_1}^{\theta_2}\ln\left(1+\frac{d^2}{h^2}\sec^2(\theta)\right)\mathrm{d}\theta+\frac{(\theta_2-\theta_1)}{2}\ln\left(\frac{h^2}{h^2+{r_1}^2}\right),
\end{aligned} \tag{B.6}$$

where the first term can be derived by the following lemma.

Lemma B.2. For $-\frac{\pi}{2} < x < \frac{\pi}{2}$ and $\alpha \geq 0$,

$$\int_0^x \ln\left(\alpha\sec^2(t)+1\right)\mathrm{d}t = \frac{1}{2}\mathrm{Im}\left\{\begin{array}{l}\mathrm{Li}_2\left(\left(-2\sqrt{\alpha^2+\alpha}-2\alpha-1\right)e^{-2jx}\right)\\+\mathrm{Li}_2\left(\left(2\sqrt{\alpha^2+\alpha}-2\alpha-1\right)e^{-2jx}\right)\\+2\mathrm{Li}_2\left(-e^{2jx}\right)\end{array}\right\}. \tag{B.7}$$

Proof: For $-\frac{\pi}{2} < x < \frac{\pi}{2}$,

$$\int_0^x \ln\left(\alpha \sec^2(t)+1\right) \mathrm{d}t = \int_0^x \ln\left(\alpha+\cos^2(t)\right) \mathrm{d}t - 2\int_0^x \ln\left(\cos(t)\right) \mathrm{d}t. \tag{B.8}$$

For the first term $\int_0^x \ln\left(\alpha+\cos^2(t)\right) \mathrm{d}t$, define $\beta_1 = -2\sqrt{\alpha^2+\alpha} - 2\alpha - 1$ and $\beta_2 = 2\sqrt{\alpha^2+\alpha} - 2\alpha - 1$,

$$\begin{aligned}\int_0^x \ln\left(\alpha+\cos^2(t)\right) \mathrm{d}t &= \int_0^x \ln\left(\alpha + \frac{1}{4}e^{-2jt} + \frac{1}{4}e^{2jt} + \frac{1}{2}\right) \mathrm{d}t \\ &= \int_0^x \ln\left(\frac{\left(1-\beta_1 e^{-2jt}\right)\left(1-\beta_2 e^{-2jt}\right)}{4e^{-2jt}}\right) \mathrm{d}t \\ &= \int_0^x \ln\left(1-\beta_1 e^{-2jt}\right) \mathrm{d}t + \int_0^x \ln\left(1-\beta_2 e^{-2jt}\right) \mathrm{d}t + jx^2 - x\ln 4.\end{aligned} \tag{B.9}$$

Inserting $t_1 = \beta e^{-2jt}$ and following the definitions $\mathrm{Li}_1(x) \triangleq -\ln(1-x)$ and $\mathrm{Li}_2(x) \triangleq \int_0^x \frac{\mathrm{Li}_1(t_1)}{t_1} \mathrm{d}t_1$,

$$\begin{aligned}\int_0^x \ln\left(1-\beta e^{-2jt}\right) \mathrm{d}t &= -\int_0^x \mathrm{Li}_1(\beta e^{-2jt}) \mathrm{d}t \\ &= -\frac{j}{2}\int_0^{\beta e^{-2jx}} \frac{\mathrm{Li}_1(t_1)}{t_1} \mathrm{d}t_1 = -\frac{j}{2}\mathrm{Li}_2(\beta e^{-2jx}).\end{aligned} \tag{B.10}$$

Since $\ln\left(\alpha+\cos^2(t)\right)$ is a real function for $-\frac{\pi}{2} < t < \frac{\pi}{2}$ and $\alpha \geq 0$,

$$\mathrm{Im}\left\{ jx^2 - x\ln 4 - \frac{j\left[\mathrm{Li}_2(\beta_1 e^{-2jx}) + \mathrm{Li}_2(\beta_2 e^{-2jx})\right]}{2} \right\} = 0, \tag{B.11}$$

and

$$\mathrm{Im}\left\{ \frac{j\left[\mathrm{Li}_2(\beta_1 e^{-2jx}) + \mathrm{Li}_2(\beta_2 e^{-2jx})\right]}{2} \right\} = x^2. \tag{B.12}$$

Inserting (B.10) and (B.12) into (B.9),

$$\begin{aligned}\int_0^x \ln\left(\alpha+\cos^2(t)\right) \mathrm{d}t &= jx^2 - x\ln 4 - \frac{j\left[\mathrm{Li}_2(\beta_1 e^{-2jx}) + \mathrm{Li}_2(\beta_2 e^{-2jx})\right]}{2} \\ &= -x\ln 4 + \mathrm{Im}\left\{ \frac{\mathrm{Li}_2(\beta_1 e^{-2jx}) + \mathrm{Li}_2(\beta_2 e^{-2jx})}{2} \right\}.\end{aligned} \tag{B.13}$$

Inserting (B.13) and (A.5) into (B.8), (B.7) can be obtained following some algebraic manipulations. ■

Using Lemma B.2 in (B.6), for $n=2$ and $h\neq 0$,

$$\begin{aligned}\mathscr{H}_2(\theta_1,\theta_2,r_1,d,h,n) =& \frac{1}{4}\mathrm{Im}\left\{\begin{array}{l}\mathrm{Li}_2\left(-\frac{2d\sqrt{h^2+d^2}+2d^2+h^2}{h^2}e^{-2j\theta_2}\right)\\ -\mathrm{Li}_2\left(-\frac{2d\sqrt{h^2+d^2}+2d^2+h^2}{h^2}e^{-2j\theta_1}\right)\\ +\mathrm{Li}_2\left(\frac{2d\sqrt{h^2+d^2}-2d^2-h^2}{h^2}e^{-2j\theta_2}\right)\\ -\mathrm{Li}_2\left(\frac{2d\sqrt{h^2+d^2}-2d^2-h^2}{h^2}e^{-2j\theta_1}\right)\\ +2\mathrm{Li}_2\left(-e^{2j\theta_2}\right)-2\mathrm{Li}_2(-e^{2j\theta_1}\right)\end{array}\right\}\\ &+\frac{(\theta_2-\theta_1)}{2}\ln\left(\frac{h^2}{h^2+{r_1}^2}\right).\end{aligned} \tag{B.14}$$

When $n=2$ and $h=0$, (5.43) can be rewritten as

$$\begin{aligned}\mathscr{H}_2(\theta_1,\theta_2,r_1,d,h,n) &= \int_{\theta_1}^{\theta_2}\int_{r_1}^{\frac{d}{\cos(\theta)}} r^{-1}\mathrm{d}r\mathrm{d}\theta\\ &= -\int_{\theta_1}^{\theta_2}\ln(\cos(\theta))\mathrm{d}\theta+(\theta_2-\theta_1)\ln\left(\frac{d}{r_1}\right),\end{aligned} \tag{B.15}$$

where the first term can be derived by (A.5). Then

$$\mathscr{H}_2(\theta_1,\theta_2,r_1,d,h,n)=\frac{1}{2}\mathrm{Im}\left\{\mathrm{Li}_2\left(-e^{2j\theta_2}\right)-\mathrm{Li}_2\left(-e^{2j\theta_1}\right)\right\}+(\theta_2-\theta_1)\ln\left(\frac{2d}{r_1}\right). \tag{B.16}$$

The closed-form expression of $\mathscr{H}_2(\cdot)$ in (5.34) can be obtained with (B.5), (B.14), and (B.16).